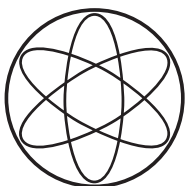# Technische Universität München

Majorana Dark Matter: The Power of Direct, Indirect and Collider Searches

Author:
Stefan Vogl

Advisor:
Prof. Dr. Alejandro Ibarra

Dissertation

Physik Department T30D

Majorana Dark Matter: The Power of Direct, Indirect and Collider Searches

Stefan Vogl

Abstract

Even though the amount of gravitational evidence for dark matter is overwhelming, the properties of dark matter still remain one of the most intriguing puzzles of high energy physics. Elusive by its very nature, most candidates for dark matter interact only weakly with Standard Model particles and are hard to probe. Nevertheless, a number of detection strategies, i.e. indirect, direct and collider searches, have seen a tremendous increase in sensitivity in the last decade and begin to cut into the parameter space of thermal dark matter. In this work, we discuss a promising signature for dark matter annihilations in the gamma-ray sky and report results from a search for gamma-ray features based on Fermi-LAT observations of the Galactic Center. Furthermore, we analyse the impact of direct detection experiments on these scenarios and comment on the complementarity of direct and indirect detection. In addition, we derive limits on spin-dependent dark matter interactions from the XENON100 experiment and demonstrate the importance of spin-dependent dark matter nucleon scattering for the detection of dark matter with the next generation of direct detection experiments. Finally, we consider the possibility of probing the dark sector with collider experiments and compare the sensitivity of the LHC with different detection strategies.

Zusammenfassung

Obwohl astronomische und kosmologische Beobachtungen überwältigende Beweise für Dunkle Materie liefern bleiben die Eigenschaften des Dunkle-Materie-Teilchens eines der großen Rätsel der Hochenergiephysik. Da ein guter Dunkle Materie Kandidat notwendigerweise nur schwach mit den Standardmodellteilchen wechselwirken kann, ist Dunkle Materie experimentell nur schwer nachweisbar. Im letzten Jahrzehnt haben direkte und indirekte Suchmethoden, sowie Beschleunigerexperimente, trotz dieser Hindernisse erhebliche Fortschritte erzielt und beginnen den theoretisch erwarteten Parameterraum einzuschränken. In dieser Arbeit werden Dunkle Materie Annihilationsprozesse, welche zu einer lokalen Verzerrung des galaktischen Gammastrahlungsspektrum führen können, diskutiert und die Ergebnisse einer Suche nach einem solchen Gammastrahlungsüberschuss mit dem Fermi-LAT Teleskop präsentiert. Unabhängig von solchen astrophysikalischen Beobachtungen kann Dunkle Materie auch auf der Erde direkt nachgewiesen werden. Interessanterweise stehen direkte und indirekte Suchen in einer Wechselbeziehung und es ist möglich die Sensitivitäten der jeweiligen Experimente auf ihre Komplementarität hin zu analysieren. Eine weitere Einschränkung des Parameterraumes wird durch die Interpretation der Daten des XENON100 Experiments in Form von Grenzen an den Spin-abhängigen Wirkungsquerschnitt erzielt und es kann gezeigt werden, dass die Berücksichtigung von Spin-abhängigen Streuprozessen in der nächsten Generation von Experimenten äußerst relevant ist. Abschließend wird zudem die Möglichkeit diskutiert, Dunkle Materie am LHC zu beobachten.

Contents

1. Introduction

The origin and the nature of dark matter is one the of most intriguing unanswered questions in high energy physics and particle cosmology. Although our observations of the gravitational effects of dark matter have made tremendous progress since the first indications for a sizeable abundance of non-luminous matter discovered in the early 1930s [1, 2], and we know the abundance of dark matter to unprecedented precision today, $\Omega h^2 = 0.1199 \pm 0.0027$ [3], the microscopic physics of dark matter still remains a puzzle. As the known particles of the Standard Model (SM) do not have the right properties to account for dark matter, any solution of this puzzle requires an extension of the SM and must invoke new physics to explain the origin of dark matter. One of the most promising dark matter candidates is a weakly-interacting massive particle (WIMP). This class of particles is interesting as, for a reasonable choice of parameters, they can be produced with the observed relic abundance by thermal freeze-out in the early universe and have all the properties required for a good dark matter candidate. In the following we will assume that dark matter has a mass in the GeV to TeV range and interacts with the Standard Model particles with a strength of the order of the weak interactions, even though we do not require these to be actual gauge interactions. We will use the terms WIMP and dark matter interchangeably.

WIMP-like dark matter is interesting from a particle physics point of view as the thermal production mechanism implies further interactions with the SM which can be used to detect dark matter with a number of different experimental approaches. Most closely related to thermal freeze-out are dark matter annihilations in the universe today, which contribute to the fluxes of cosmic-rays, neutrinos or gamma-rays at the Earth. A different possibility is the scattering of dark matter off Standard Model particles, which is employed in direct detection experiments and, finally, the production of dark matter or other particles of the dark sector in accelerator experiments. All these experimental approaches have made tremendous progress in the last decade and recent results, for example from XENON100 [4] and LUX [5] in direct searches, Fermi-LAT [6], AMS-02 [7], H.E.S.S. [8], MAGIC [9] and IceCube [10] in indirect searches and the LHC in collider searches [11, 12, 13, 14], begin to cut into the regions of theoretical expectations. Despite - or perhaps because of - this wealth of experimental data a number of challenges for dark matter theory arise. The interpretation of the experimental observations requires an understanding of their implications for the theory of dark matter, while, in particular for collider searches, even defining an useful observable remains a non-trivial task. Furthermore, we need to use all available search strategies and employ their synergy efficiently if we want to tackle the dark matter puzzle and identify the dark matter particle or rule out models for dark matter conclusively. The aim of this work is to explore the power of various experimental searches and

assess their relative detection power. In order to be able to determine the relevant observables and quantify their correlation we employ in a large part, but not exclusively, a simplified model for Majorana dark matter coupling to the Standard Model fermions via a Yukawa interaction with a new scalar.

Thermal dark matter is expected to annihilate in the galaxy today and thus contributes to the flux of cosmic-rays, neutrinos and gamma-rays. Since the possible contribution from dark matter is most likely subleading, it is one of the big challenges for indirect detection to understand the astrophysical background to the necessary precision. A sharp spectral feature in gamma-rays is a particularly promising signature as astrophysical processes are in general not expected to mimic such a signal. In this work, we perform a dedicated analysis of data taken by the gamma-ray space telescope Fermi-LAT during the first 43 months of operation and search for a gamma-ray feature. Furthermore, we propose a new adaptive technique to determine the optimal target region for any kind of dark matter profile. The limits on the dark matter annihilation cross section derived from our analysis are competitive or even stronger than previous limits from the observation of dwarf galaxies. However, we are not able to exclude the annihilation rates expected for thermally produced dark matter. Interestingly, we find a hint for a gamma ray excess at 130 GeV with a global significance of 3.1σ, which could be fitted by an internal bremsstrahlung feature with a dark matter mass of about 150 GeV or a gamma-ray line with a dark matter mass of roughly 130 GeV.

A different way to test dark matter is direct detection. We present an introduction to the calculation of the nuclear recoil rate in direct detection experiments. This can be used to derive constraints on the parameter space of a simplified dark matter model and to compare the sensitivity of direct and indirect detection. Including further data from observations of the Galactic Center with the H.E.S.S. Cherenkov telescope, we find, on the one hand, that the limits from indirect detection extend up to tens of TeV with very little dependence on the mass difference. On the other hand, limits from direct detection exhibit a strong dependence on the mass difference. For small to moderate mass splittings and dark matter masses below one TeV the constraints from XENON100 on dark matter coupling to light quarks surpass the limits from indirect detection by orders of magnitude. Furthermore, we analyse the prospects of future direct and indirect detection experiments and find the two search strategies to be fully complementary with XENON1T chiefly probing small to moderate mass differences up to dark matter masses of one TeV, while CTA is most sensitive in the multi-TeV range. Unfortunately, even future indirect detection experiments do not seem to possess the sensitivity necessary to probe thermal dark matter.

Next we study the spin-dependent sensitivity of XENON100. As is well-known [15, 16], xenon based detectors naturally contain a significant fraction of neutron odd isotopes, which are sensitive to spin-dependent interactions. We analyse the results of the latest XENON100 run and find that the constraints derived from this data set are the strongest bounds on spin-dependent dark matter neutron scattering to date. Furthermore, we apply our bounds to two exemplary

dark matter models and show that limits from spin-dependent interactions can exceed the limits from spin-independent scattering. Additionally, limits on the spin-dependent cross section are able to rule out regions of parameter space which are in agreement with all other constraints.

Finally, we consider the LHC implications of a simplified model of Majorana dark matter coupling to Standard Model fermions via a Yukawa interaction with a new scalar in more detail. The collider phenomenology of this model is quite promising as pairs of the coloured mediator can be produced copiously at the LHC and decay into jets and missing energy. Such a final state can be searched for very efficiently by ATLAS and CMS. We discuss the production rate of the scalar in detail and include both QCD processes and t-channel exchange of dark matter. In particular, the dark matter induced t-channel production mode dominates the total cross section in significant parts of the parameter space. As this channel is quite distinct from the more commonly considered production via strong interactions, we perform a full Monte Carlo simulation, including jet matching with up to two additional jets, in order to determine the appropriate experimental efficiencies. These can then be used to derive upper limits on the interactions of dark matter with the Standard Model and we discuss the complementarity of collider searches with direct and indirect detection.

The structure of this thesis is as follows. In chapter 2 we review astrophysical evidence for dark matter before we introduce a class of simplified models for dark matter interactions with Standard Model fermions and discuss the thermal freeze-out mechanism in chapter 3. We describe our search for dark matter annihilations with Fermi-LAT in chapter 4. In chapter 5 we discuss the concepts of direct detection and comment on the complementarity between direct and indirect detection before analysing the importance of XENON100 for spin-dependent dark matter scattering. Finally, we investigate the implications of collider searches for dark matter and present our results in chapter 6 before concluding in chapter 7.

Parts of this thesis have been published in the following articles:

[17] **Dark matter annihilations into two light fermions and one gauge boson: General analysis and antiproton constraints**
M. Garny, A. Ibarra, and S. Vogl
JCAP 1204 (2012) 033, [arXiv:1112.5155]

[18] **Fermi LAT Search for Internal Bremsstrahlung Signatures from Dark Matter Annihilation**
T. Bringmann, X. Huang, A. Ibarra, S. Vogl, and C. Weniger
JCAP 1207 (2012) 054, [arXiv:1203.1312]

[19] **Closing in on mass-degenerate dark matter scenarios with antiprotons and direct detection**
M. Garny, A. Ibarra, M. Pato, and S. Vogl
JCAP 1211 (2012) 017, [arXiv:1207.1431]

[20] **On the spin-dependent sensitivity of XENON100**
M. Garny, A. Ibarra, M. Pato, and S. Vogl
Phys.Rev. D87 (2013) 056002, [arXiv:1211.4573]

[21] **Internal bremsstrahlung signatures in light of direct dark matter searches,**
M. Garny, A. Ibarra, M. Pato, and S. Vogl
JCAP 1312 (2013) 046, [arXiv:1306.6342]

[22] **Majorana Dark Matter with a Coloured Mediator: Collider vs Direct and Indirect Searches**
M. Garny, A. Ibarra, S. Rydbeck, and S. Vogl
accepted for publication in JHEP, arXiv:1403.4634

Furthermore, this thesis contains some material which has been used in my diploma thesis and was originally published in

[23] **Antiproton constraints on dark matter annihilations from internal electroweak bremsstrahlung**
M. Garny, A. Ibarra, and S. Vogl
JCAP 1107 (2011) 028, arXiv:1105.5367

2. Observational Evidence for Dark Matter

First hints for dark matter were already found in the early 1930s when the velocities of stars in the Milky Way [1] and of galaxies in the Coma cluster [2] were found to indicate a dynamical mass of these systems which exceeds the mass of luminous matter significantly. Later on, a systematic observation of the velocities of stars in galaxies was conducted, see e.g. [27], and the rotation curves of these galaxies were determined. If luminous matter is the dominant contribution to the mass of a galaxy, the virial theorem implies that the circular velocity of stars in the outer part of the galaxy, where the dominant part of the mass of the galaxy is within the stars galactic radius, should scale as $v \propto 1/\sqrt{r}$. However, observations of real galaxies reveal that the radial velocity remains surprisingly constant up to large radii, see e.g. Fig. 2.1. This behaviour can be explained if there is an additional non-luminous, i.e. dark, contribution to the mass of the galaxy which extends significantly beyond the characteristic scale of the visible mass distribution.

Further evidence for dark matter can be obtained by the direct observation of the gravitational impact of dark matter on light. General relativity predicts that the path of light gets distorted by a gravitating mass, which leads to an effect known as gravitational lensing. Strong lensing, which is caused by a large gravitating mass close to the path of light, can distort the image of an object in the background to such an extent that partial arcs or even multiple images appear. The observation of strong lensing confirms that the gravitational mass of clusters exceeds their luminous mass significantly [28]. However, strong lensing is a rather rare phenomenon since the presence of a sufficiently large mass very close to the line of sight is required to achieve such an effect. A rather more common phenomenon than strong lensing is weak lensing, which only induces a marginal distortion such that the effect on the image of an individual object is not observable. However, weak gravitational lensing can be detected since it induces a coherent distortion of multiple background objects which allows the reconstruction of the matter distribution in the foreground from the statistical properties of the lensed images [29]. This technique has been used successfully to determine the dark matter profile of galaxy clusters [30].

Another confirmation of the existence of dark matter comes from the observation of the rather particular galaxy cluster 1E0657-558, better known as the Bullet Cluster. This object consists of two galaxy clusters which collided recently and passed through each other. Observations of the Bullet Cluster with x-ray telescopes allow to trace the distribution of gas, which is the dominant contribution to luminous matter in this object, while weak gravitational lensing can be employed to determine the mass distribution [25]. As can be seen in Fig. 2.2, the distribution of the gas is completely misaligned with the observed mass distribution, thus indicating that the dominant

DISTRIBUTION OF DARK MATTER IN NGC 3198
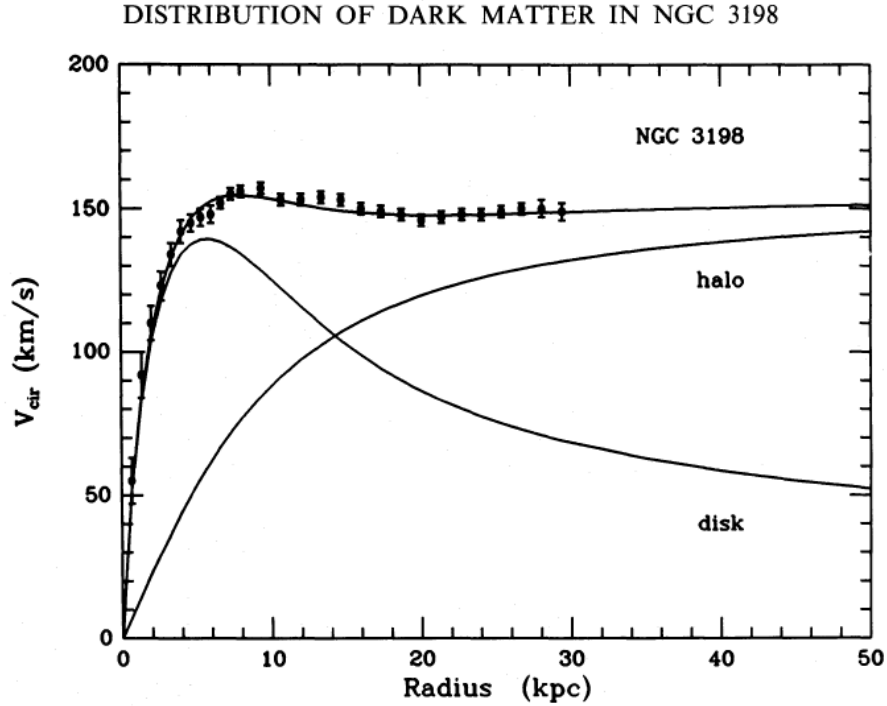
Figure 2.1.: Rotation curve of NGC 3198 and fit with a dark matter halo model. Figure from
         [24].

contribution to the cluster mass is due to a dark and collision-less matter component.

The observation of the Cosmic Microwave Background (CMB) provides us with the most precise determination of the abundance of dark matter to date. Initially proposed by George Gamow in 1948, the CMB was discovered by Penzias and Wilson in 1965. The CMB consists of the photons from the early universe which were emitted at the time of last scattering when electrons and protons combined to form neutral hydrogen such that the universe became transparent to photons. The spectrum of the CMB can be described by a black body with a temperature of 2.73 K and small temperature anisotropies at the level of 10^{-5}. The temperature fluctuations of the CMB were discovered by the COBE mission [31] in 1993 and later on high precision measurements were conducted by WMAP [32], which was operational from 2001 to 2010, and Planck [3], which released their cosmological results in 2013. In order to analyse these temperature anisotropies in a quantitative way they are usually expanded in spherical harmonics Y_{lm} as

$$\Delta T(\hat{n}) \equiv T(\hat{n}) - T_0 = \sum_{l,m} a_{lm} Y_{lm}(\theta, \phi) \, , \tag{2.0.1}$$

where T_0 is the average temperature, θ and ϕ are spherical pole angles and a_{lm} are the coefficients of the expansion. The power spectrum can be defined as

$$C_l = \frac{1}{2l+1} \sum_{m=-l}^{l} |a_{lm}|^2 \, . \tag{2.0.2}$$
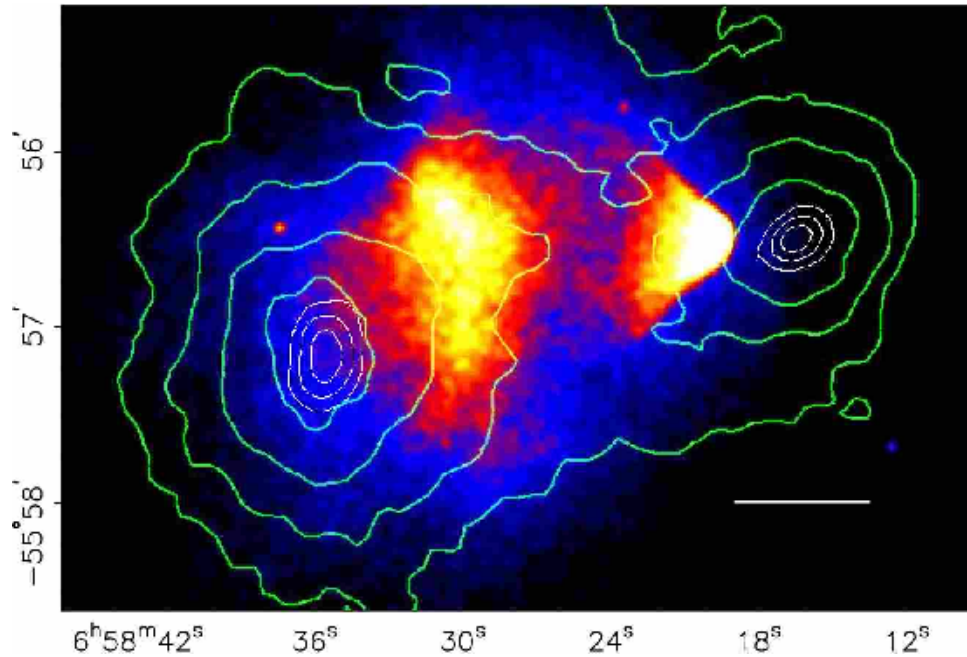
Figure 2.2.: Image of the bullet cluster depicting the mass distribution inferred from weak lensing (green contours) superimposed on the X-ray emission (indicated by a color code). Figure from [25].

In the plot often referred to as the power spectrum it is conventional to plot $l(l + 1)C_l/2\pi$ against l. An example of the power spectrum inferred from Planck data as well as a fit with the Standard Model of cosmology, ΛCDM, can be seen in Fig. 2.3. The power spectrum of these temperature fluctuations can be used to determine the matter content of the universe and calculate the abundance of both baryonic and dark matter. In general, the connection between the amplitude of the power spectrum and the cosmological parameters is complicated and far from intuitive, for an useful introduction to the CMB anisotropies and their interpretation see [33]. Using the most precise measurement of the CMB by the Planck satellite [3] and accounting for weak gravitational lensing, the energy content of the universe has been determined to be

$$\Omega_\Lambda = 0.693 \pm 0.019 \quad \text{and}$$
$$\Omega_m = 0.307 \pm 0.019 \,,$$

where Ω_Λ and Ω_m are the energy density of dark energy and matter normalized to the critical energy density of the universe, respectively. The matter density can be decomposed further into baryons and dark matter, which yields, after rescaling by h^2,

$$\Omega_b h^2 = 0.02217 \pm 0.00033 \quad \text{and}$$
$$\Omega_c h^2 = 0.11805 \pm 0.0031 \,,$$

where $\Omega_b h^2$ denotes the abundance of baryons while $\Omega_c h^2$ is the abundance of cold dark matter. As becomes apparent from these numbers, the total abundance of dark matter exceeds the abun-

Figure 2.3.: The temperature angular power spectrum of the CMB as measured by the Planck satellite. The vertical scale is $l(l+1)C_l/2\pi$. Figure from [26].

dance of baryons in the universe by about a factor of 5 and agrees nicely with the astrophysical observation that the mass of clusters and galaxies is dominated by their dark matter component.
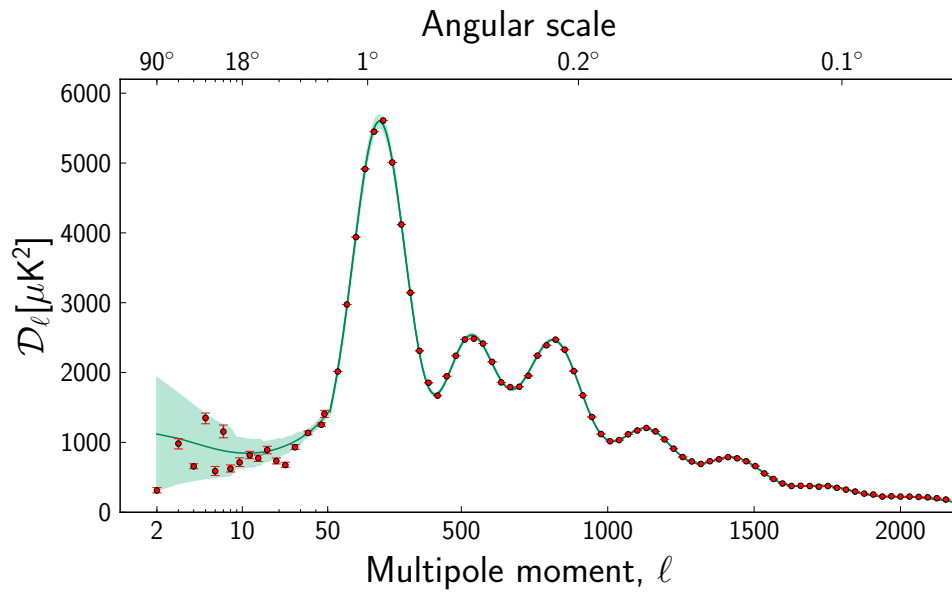
3. Simplified Models for Thermal Majorana Dark Matter

In the following we will briefly describe our fundamental assumptions regarding the nature of dark matter and comment on its role in the evolution of the universe. In the beginning the universe is assumed to be in a hot and dense initial state. At that stage, the universe can be described by a hot plasma of SM and exotic particles, one of which is later going to constitute dark matter. As the universe expands the temperature and, accordingly, the density of all particles decreases and eventually the density of a given particle species becomes so low that the interaction rate of this particle with the plasma can no longer keep it in thermal equilibrium. At this point the particle decouples from the thermal bath and becomes a thermal relic.

In this chapter we will first discuss briefly some of the properties of dark matter and argue that simplified models for dark matter and its interactions with SM particles can provide valuable information about the expected phenomenology of dark matter candidates. Furthermore, we are going to introduce the thermal freeze-out mechanism and comment in a little more detail on a well known exception to the standard calculation which can be relevant for the scenarios considered in this thesis.

3.1. Simplified Majorana Dark Matter

Unfortunately, the compelling evidence for dark matter from astrophysics and cosmology does not allow us to address the question regarding the nature of dark matter. In order to detect dark matter as a particle and determine its interactions with the SM we therefore need to conduct further experiments. However, currently there is no compelling theory for dark matter which could guide our experimental efforts and, even if we subscribe to the WIMP paradigm, we need to make certain assumptions about the properties of dark matter in order to proceed. An intriguing possibility for the study of dark matter phenomenology is the construction of a minimal model. While not being subject to the restrictions immanent to a full theory, e.g. minimal supersymmetry or extra dimensions, such a framework allows to explore the possible signals of dark matter in experiments and analyse their correlations. In the following we present the basic features of a simplified model for Majorana dark matter which we will revisit at some points in the phenomenological analysis presented in the later chapters. We consider a minimal extension of the Standard Model by a Majorana fermion χ, which we assume to constitute all the dark

matter in the Universe, and a beyond the SM scalar η, which mediates interactions with SM fermions. The Lagrangian of this model is given by

$$\mathcal{L} = \mathcal{L}_{SM} + \mathcal{L}_\chi + \mathcal{L}_\eta + \mathcal{L}_{int} \ . \tag{3.1.1}$$

Here $\mathcal{L}_{SM}$ stands for the pure SM Lagrangian, while $\mathcal{L}_\chi$ and $\mathcal{L}_\eta$ are the terms in the Lagrangian involving only the Majorana fermion χ and the scalar η, respectively. $\mathcal{L}_\chi$ and $\mathcal{L}_\eta$ can be written as

$$\mathcal{L}_\chi = \frac{1}{2}\bar{\chi}^c i\partial\!\!\!/\chi - \frac{1}{2}m_\chi\bar{\chi}^c\chi \ , \text{ and}$$
$$\mathcal{L}_\eta = (D_\mu\eta)^\dagger(D^\mu\eta) - m_\eta^2\eta^\dagger\eta \ , \tag{3.1.2}$$

where D_μ corresponds to the covariant derivative. Finally, $\mathcal{L}_{int}$ denotes the terms which are responsible for the interactions of the dark sector with the SM fields. $\mathcal{L}_{int}$ can be split into two parts, $\mathcal{L}_{int}^{fermion}$, which describes the interactions with SM fermions, and $\mathcal{L}_{int}^{scalar}$, which contains the term coupling the scalar η to the Standard Model Higgs doublet H.

Depending on the details of the model a number of different terms can arise here. On the one hand, the quantum numbers of χ under the SM gauge group $SU(3)_C \times SU(2)_L \times U(1)_Y$ are partially constrained by the requirement that dark matter is electrically neutral and does not carry a colour charge. On the other hand, the quantum number under $SU(2)_L$ is free provided the hypercharge is chosen such that no electric charge is generated. In the following we will restrict the discussion to the case of a $SU(2)_L$ singlet and refer the reader to [17] for details regarding $SU(2)_L$ doublet dark matter. Furthermore, there is some freedom regarding the SM fermions which are coupled to dark matter. In principle, χ can interact with all SM fermions, i.e. all generations of quarks and leptons and with all chiralities, provided the quantum numbers of the mediator η are chosen such that the interaction Lagrangian $\mathcal{L}_{int}$ is invariant under the Standard Model gauge group. For the sake of simplicity we will focus here on the scenario with dark matter coupling to right-handed SM fermions such that η is a singlet under $SU(2)_L$. In this case the interaction Lagrangian with fermions reads

$$\mathcal{L}_{\text{int}}^{fermion} = -f_{ij}\bar{\Psi}_{Ri}\chi\eta_j + \text{h.c.} \ , \tag{3.1.3}$$

where Ψ_{R_i} denotes a right-handed fermion of flavour i. In particular in the quark sector, this kind of interactions with the dark matter can generate dangerously large flavour changing neutral currents (FCNCs) thus forcing us to impose further restrictions on the parameter space of the model. We find two possibilities to avoid large FCNCs:

1. We take the scalar η to couple exclusively to right handed up quarks. Such a scenario corresponds to an alignment type set-up of the squark sector in the minimal supersymmetric Standard Model (MSSM) and can be realized by appropriate flavour symmetries at a high scale [34].

2. We consider a pair of mass degenerate scalars η_i and η_j which couple to right handed quarks of the first and second generation with an universal coupling f. Such a scenario is motivated

by the paradigm of minimal flavour violation [35] which requires flavour universality among quarks with the same gauge quantum numbers while allowing a separation of particles belonging to different multiplets.

We show explicitly in Appx. A that with these assumption the stringent constraints from FCNCs can be avoided. Furthermore, we consider dark matter coupling exclusively to bottom quarks. In the lepton sector the flavour constraints are less severe. Nevertheless, we assign the appropriate flavour quantum number to η and couple the scalar exclusively to one lepton flavour. Finally, we impose a new discrete Z_2 symmetry under which all Standard Model particles are even and all particles of the dark sector are odd in order to ensure dark matter stability.

Finally, the part of the interaction Lagrangian which describes interactions between the scalar mediator and the SM Higgs reads

$$\mathcal{L}_{\text{int}}^{scalar} = -\lambda_3 (HH^\dagger)(\eta_i \eta_i^\dagger) \, , \tag{3.1.4}$$

where λ_3 is an a priori free four scalar coupling. This term provides an additional contribution to the mass of η, but this can be absorbed in the tree level mass by the substitution $m_\eta^2 + \lambda_3 v_{EW}^2 \to m_\eta^2$ where v_{EW} is the vacuum expectation value of the Higgs field. Furthermore, this term induces a coupling between η and H, which could in principle have an impact on dark matter. In practice the influence of this interaction on dark matter phenomenology is limited as direct and indirect detection are only sensitive to the interactions of the dark matter particle χ while collider searches probe only the gauge and Yukawa interactions of η. The scalar interactions could modify the relic density in the coannihilation scenario discussed in more detail in the next section, but numerical checks showed that only rather large values of $\lambda_3 > 1$ have an impact on the dark matter abundance.

Interestingly, it is not possible to characterize the phenomenology of this model in terms of a small set of effective operators and higher order effects can be relevant. For instance, the constraints from indirect detection are dominated by two-to-three and loop induced annihilation channels. This is due to two reasons; on the one hand, the tree-level two-to-two processes are suppressed by helicity and velocity while, on the other hand, channels such as $\chi\chi \to q\bar{q}\gamma$ and $\chi\chi \to \gamma\gamma$ ($Z\gamma$) produce high energy gamma rays which lead to a most distinct signature for gamma-ray telescopes like H.E.S.S. or Fermi-LAT. Furthermore, in direct detection the lowest order operators generating spin-independent interactions happen to vanish for a Majorana fermion with chiral interactions and, consequently, the leading contributions are due to either spin-dependent interactions or higher order effects. Finally, the most intriguing signature at the LHC is not related to the production of dark matter itself but to the production of the scalar mediator η. Therefore, collider searches open a completely different way of constraining the dark sector, which we find to be complementary to direct and indirect detection.

3.2. The Relic Density

Probably the most convincing argument in favour of WIMP dark matter is the fact that such a particle can be produced thermally in the early universe and quite generically freezes out with an abundance close to the value $\Omega h^2 = 0.11805 \pm 0.0031$ [3] observed by the Planck satellite. Qualitatively, thermal decoupling, which is known to be responsible for the relic abundance of regular matter in the universe, can be described rather intuitively [36]. Initially, the hot universe is assumed to be in thermal equilibrium such that this state can be described exclusively by a temperature T, which is the highest scale in all processes and compared to which the masses of all particles, including the dark matter particle χ, are small $m_\chi \ll T$. As the universe expands the temperature of the plasma decreases and at a certain time the temperature T becomes comparable to the dark matter mass. Then the rate $\Gamma(\chi\chi \leftrightarrow \text{SM SM})$ with which dark matter χ and Standard Model particles are converted into each other begins to be suppressed by the comparatively low abundance of sufficiently energetic particles. Once the rate $\Gamma(\chi\chi \leftrightarrow \text{SM SM}) \lesssim H$, where H is the expansion rate of the universe, the evolution of the dark matter density begins to be dominated by H exclusively and thermal equilibrium can no longer be maintained.

3.2.1. The Standard Calculation

In order to obtain a more quantitative picture of thermal freeze-out it is necessary to solve the Boltzmann equation for the evolution of a particle distribution in an expanding universe [36, 37, 38]. The appropriate equation to describe the evolution of the number density of WIMPs n_χ can be written as

$$\frac{\mathrm{d}n_\chi}{\mathrm{d}t} + 3Hn_\chi = -\langle \sigma v \rangle (n_\chi^2 - n_{\chi,eq}^2) , \tag{3.2.1}$$

where H is the Hubble rate, $\langle \sigma v \rangle$ corresponds to the thermally averaged annihilation cross section and $(n_\chi^2 - n_{\chi,eq}^2)$ parametrizes the departure from the thermal equilibrium number density $n_{\chi,eq}$. It is convenient to re-express this equation in terms of the comoving number density $Y_\chi = n_\chi/s$ and x, where s is the entropy density of the universe and the dimensionless number x is the ratio of the dark matter mass and the temperature $x = m_\chi/T$. Assuming entropy conservation Eq. 3.2.1 simplifies and yields the following equation for Y,

$$\frac{\mathrm{d}Y_\chi}{\mathrm{d}x} = -\frac{\langle \sigma v \rangle s}{Hx}(Y_\chi^2 - Y_{\chi,eq}^2). \tag{3.2.2}$$

The evolution of H during the radiation dominated phase of the universe is given by

$$H = \frac{\pi T^2}{M_{Pl}} \sqrt{\frac{g_*}{90}} , \tag{3.2.3}$$

where $M_{Pl} = 2.4 \times 10^{18}$ GeV is the Planck mass and g_* is the number of effective degrees of freedom. For completely general $\langle \sigma v \rangle$ and without making a priori assumptions about the freeze-out temperature T_F Eq. 3.2.2 needs to be solved numerically, however, approximate analytic

solutions can be derived if decoupling occurs while χ is either fully relativistic of fully non-relativistic. In this work, only the non-relativistic case is of interest.

In the non-relativistic limit, i.e. for freeze-out temperature $x_F = m_\chi/T_F \gg 3$, $\langle\sigma v\rangle$ has a significant impact on the relic abundance since $Y_{\chi,eq}$ decreases exponentially with T and $\langle\sigma v\rangle$ determines how long thermal equilibrium can be kept. In most cases it is useful to simplify $\langle\sigma v\rangle$ using the partial wave expansion

$$\langle\sigma v\rangle = a + b\langle v^2\rangle + \mathcal{O}(\langle v^4\rangle) = a + \frac{6b}{x} + \mathcal{O}(\frac{1}{x^2}) \ , \tag{3.2.4}$$

and neglect terms of order $\mathcal{O}(\frac{1}{x^2})$ and higher. In this limit the relic abundance can be approximated by the following analytic formula,

$$Y_{\chi\infty} = Y_\chi(x \to \infty) = \frac{1}{1.3 m_\chi M_{Pl}\sqrt{g_{*(x_F)}}(a/x_F + 3b/x_F^2)} \ . \tag{3.2.5}$$

A visualization of the qualitative behaviour of the freeze-out solution can be seen in Fig. 3.1. Using $\Omega_\chi h^2 = m_\chi s Y_{\chi,\infty}/\rho_c$, where $\rho_c = 3H_0^2 M_{Pl}^2$ is the critical density of the universe and $s_0 \simeq 2900\,\mathrm{cm}^{-3}$ is the present entropy density, we can recast the relic abundance in a more conventional form as

$$\Omega_\chi h^2 = 2.7 \times 10^8\, Y_{\chi\infty} \left(\frac{m_\chi}{1\ \mathrm{GeV}}\right) = \frac{8.5 \times 10^{-11} x_F \mathrm{GeV}^{-2}}{\sqrt{g_{*(x_F)}}(a + 3b/x_F)} \ . \tag{3.2.6}$$

It is interesting to note that $\Omega_\chi h^2$ is inversely proportional to $\langle\sigma v\rangle$ and does not depend explicitly on the dark matter mass m_χ. Furthermore, as is well-known, the freeze-out temperature depends only logarithmically on the WIMP mass m_χ and x_F is usually found in the range $x_F \simeq 20-25$. Thus, a reasonable estimate of the relic density is given by the famous relation

$$\Omega_\chi h^2 = \frac{3 \times 10^{-27} \mathrm{cm}^2\mathrm{s}^{-1}}{\langle\sigma v\rangle} \ , \tag{3.2.7}$$

which leads to the canonical thermal cross section of $\langle\sigma v\rangle = 3 \times 10^{-26}\mathrm{cm}^2\mathrm{s}^{-1}$. Inserting the appropriate expressions for a and b in Eq. 3.2.6 the relic density for the dark matter candidate presented in Sec. 3.1 reads (see e.g. Ref. [23])

$$\Omega_{\mathrm{DM}} h^2 \simeq 0.11\frac{1}{N_c}\left(\frac{0.35}{f}\right)^4\left(\frac{m_\chi}{100\mathrm{GeV}}\right)^2\frac{(1+\mu)^4}{1+\mu^2} \ , \tag{3.2.8}$$

where $\mu = m_\eta^2/m_\chi^2$ and N_c denotes a colour factor.

3.2.2. Coannihilations

As pointed out by [39], the standard calculation of the relic density fails if there are further particles of the dark sector with a mass close to the dark matter mass. In that case these additional particles need to be included in the Boltzmann equation and can induce significant deviations from the canonical freeze-out result.
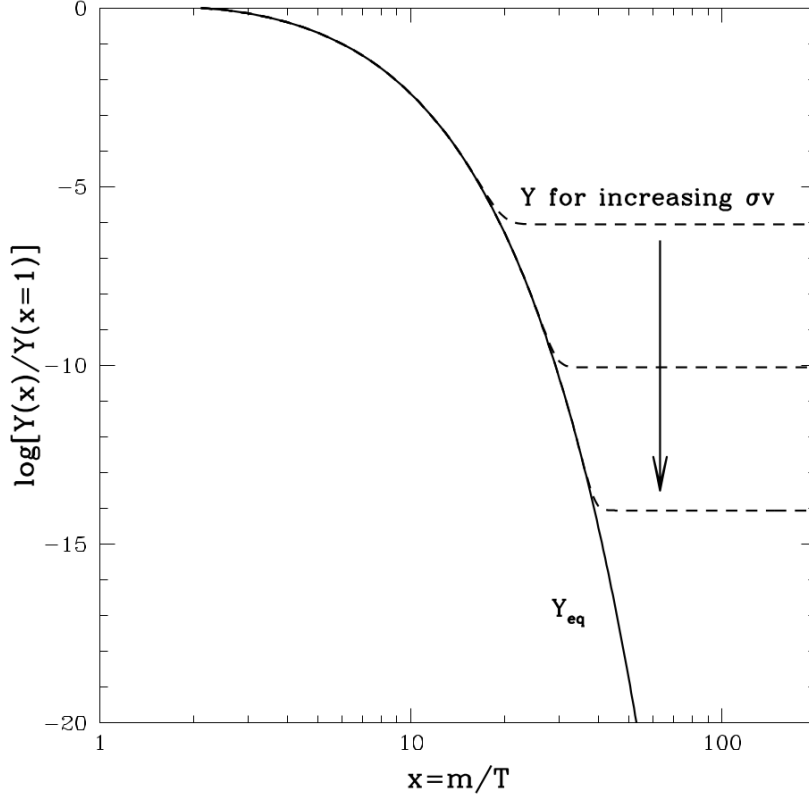
Figure 3.1.: Qualitative evolution of the dark matter abundance Y with x. Figure from [36].

Let us consider for instance the particle model presented in the previous section. When the mass of the scalar particle η and the Majorana fermion χ are quasi-degenerate, coannihilations can become important. Consequently, it is necessary to include all possible annihilation and coannihilation processes $X_i X_j \to$ SM SM into Standard Model particles in the scattering term in Eq. 3.2.1, where $X_i = \chi, \eta, \bar{\eta}$. As many different processes can contribute, a complete description of coannihilations is complicated and cumbersome. In order to ascertain that all relevant processes are taken into account we use a fully numerical calculation of thermal freeze-out performed with the public code MicrOMEGAS2.4 [40] in all our quantitative results. We have compared the numerical solution against a semi-analytic approximation [41]. The analytic correction to the relic density can be parametrized as

$$R = \frac{\Omega_0}{\Omega} = \frac{\sigma v_{eff}}{\sigma v_0} \frac{x_f}{x_{f0}} \, , \tag{3.2.9}$$

where the quantities with subscript zero are derived without coannihilations. Furthermore, the effective annihilation cross section can be expressed as

$$\sigma v_{eff} = \sum_{ij} \frac{n_i^{eq} n_j^{eq}}{\left(\sum_k n_k^{eq}\right)^2} \sigma_{ij} v \, , \tag{3.2.10}$$

where $n_i^{eq} = g_i(m_i T/(2\pi))^{3/2} e^{-m_i/T}$ and g_i counts the number of internal degrees of freedom of the particle species i. For Majorana dark matter $g_\chi = 2$ and for a coloured mediator $g_\eta = g_{\bar{\eta}} = 3$. In the case of dark matter coupling to light quarks we find four leading contributions to σv_{eff}; the annihilation of a dark matter pair $\chi\chi \to q\bar{q}$, the annihilation of a mixed initial state $\chi\eta \to qg$ and the annihilation of a pair of scalars $\eta\bar{\eta} \to gg$ or $\eta\eta \to qq$. The Feynman diagrams contributing to this set of leading processes are shown in Fig. 3.2. The cross section $\sigma(\chi\chi \to q\bar{q})$ is suppressed by helicity or velocity,

$$\sigma v(\chi\chi \to q\bar{q}) = \frac{3f^4 m_q^2}{32\pi(m_\chi^2 + m_\eta^2)^2} + \frac{f^4 v^2}{16\pi m_\chi^2}\frac{1 + m_\eta^4/m_\chi^4}{(1 + m_\eta^2/m_\chi^2)^4} \,, \qquad (3.2.11)$$

while the cross sections for the processes $\chi\eta \to qg$, $\eta\eta \to qq$, and $\eta\bar{\eta} \to gg$ have a non-zero s-wave contribution for $m_q \to 0$ [19],

$$\begin{aligned}
\sigma v(\chi\eta \to qg) &= \frac{f^2 g_s^2}{24\pi}\frac{1}{m_\eta(m_\eta + m_\chi)} \,, \\
\sigma v(\eta\bar{\eta} \to gg) &= \frac{7g_s^4}{216\pi m_\eta^2} \,, \\
\sigma v(\eta\eta \to qq) &= \frac{f^4}{6\pi}\frac{m_\chi^2}{(m_\chi^2 + m_\eta^2)^2} \,.
\end{aligned} \qquad (3.2.12)$$

Finally, we need to consider the correction to the freeze-out temperature, which is given by

$$\frac{x_{f0}}{x} \approx 1 + x_{f0}\ln(\frac{g_{eff}\sigma_{eff}}{g_\chi\sigma_0}) \,, \qquad (3.2.13)$$

where $\sigma = a + 6bx$ and $g_{eff} = \sum_i(m_i/m_\chi)^{3/2}e^{-(m_i-m_\chi)/T}$. We find that the results obtained with this semi-analytic approach are in good qualitative and quantitative agreement with our numerical result, thus confirming that both methods lead to a reasonable description of thermal freeze-out. The general outline of the procedure is completely analogous for a leptophilic η, however, the number of relevant processes is larger and we prefer to present only the numerical results in this case.

Once we require a relic density which matches the value observed by the Planck satellite $\Omega h^2 = 0.1199 \pm 0.0027$ [3] the three dimensional parameter space of the model is reduced and we can express $f = f_{th}(m_\chi, m_\eta)$. Note that not all possible choices of m_χ and m_η yield a physical solution for the thermal coupling constant f_{th}. In particular when small mass splittings make coannihilations more important the required values of the coupling f reduce dramatically. In very degenerate scenarios, $m_\eta/m_\chi \lesssim 1.1$, coannihilations can be so efficient that the total dark matter relic abundance cannot be produced thermally if $m_\chi \lesssim 200$ GeV (50 GeV) for dark matter coupling to quarks (leptons). This interesting feature, the absence of light relics, can be understood in terms of a simplified argument. In the coannihilation regime, the effective thermal cross section is of the form

$$\sigma v_{eff} = \sigma v(\chi\chi) + \sigma v(\chi\eta)e^{-\frac{m_\eta-m_\chi}{T}} + \sigma v(\eta\eta)e^{-\frac{2(m_\eta-m_\chi)}{T}} \,, \qquad (3.2.14)$$
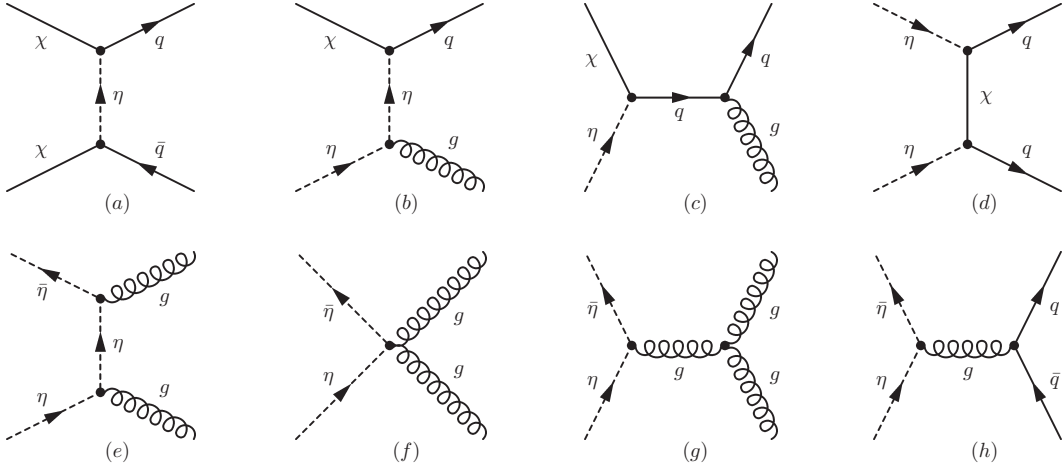
Figure 3.2.: Feynman diagrams showing the leading (co-)annihilation processes that contribute to the thermal freeze-out density. Two additional diagrams corresponding to (a) with reversed charge flow and to (d) with flipped legs are not shown, as well as several diagrams for charge conjugated processes. Figure published in [19]

where processes including the coannihilating particle η are Boltzmann-suppressed. In order to get a clearer idea of the mass and coupling dependence, we can isolate these and express the $\chi\chi$ cross section as $\sigma v(\chi\chi) = \frac{f^4}{m_\chi^2} C_{\chi\chi}$ (and likewise for the other processes), where $C_{\chi\chi}$ is a function of mass and temperature ratios only. Absorbing the Boltzmann factors into the C_{ij} functions and using the relation between the relic abundance and the effective cross section we obtain [21]

$$\Omega h^2 \sim \frac{1}{\sigma v_{eff}} = \frac{m_\chi^2}{f^4\, C_{\chi\chi} + f^2\, g^2\, C_{\chi\eta} + g^4\, C_{\eta\eta}}\,,\qquad(3.2.15)$$

where g denotes a gauge coupling. As can be seen from this equation, for $g^4 C_{\eta\eta} \neq 0$ there will always be a lower limit on the mass $m_{\chi,min} \lesssim m_\chi$ below which the relic abundance cannot be maintained even for $f = 0$. In our scenario, which includes strong coupling and only a relatively mild Boltzmann suppression this lower bound $m_{\chi,min}$ can be $\mathcal{O}(100 \text{ GeV})$ for dark matter coupling to quarks.

4. Indirect Searches: The Gamma-Ray Feature

If dark matter in the universe is a thermal relic from the hot and early universe, we expect dark matter to annihilate into SM particles today and contribute to the flux of cosmic-rays, e.g. antiprotons, positrons and neutrinos, or gamma-rays. However, an excess of these fluxes is hard to identify as that requires an excellent understanding of all possible backgrounds and, furthermore, the ability to reject non-standard astrophysical processes as a possible source of the excess. For example, the production of positrons in pulsar magnetospheres could lead to a modification of the positron fraction from secondary production [42, 43, 44, 45] which could account for the positron excess observed by Pamela [46] and AMS-2 [7], while acceleration of secondaries in supernova remnants can have a similar impact on the antiproton-to-proton ratio [47]. Among all these messengers, gamma-rays are particularly interesting as they are more easily probed than neutrinos and, in contrast to antimatter, travel basically without interactions, thus preserving spectral and spatial information about their production. Furthermore, a sharp feature in the gamma-ray spectrum is expected to be a smoking gun for dark matter annihilations as no astrophysical process can mimic such a signal (a possible exception has been proposed in Ref. [48]). While this possibility has been pointed out long ago [49], the excellent energy resolution of modern gamma-ray observatories has led to a tremendous increase in sensitivity to such a signature rather recently. Apart from a gamma-ray line from direct annihilations into photons, also internal bremsstrahlung can induce a hard spectral feature close to the highest accessible energies $E_{max} = m_\chi$, which is, with current instruments, indistinguishable from a line.

In this chapter we will first discuss the relevant annihilation cross sections in Sec. 4.1 before describing the details of our method for the derivation of limits on gamma-ray features in Sec. 4.2. We present our results in Sec. 4.3 and compare our limits with previous results from dwarf galaxies, cosmic-ray antiprotons and precision observables in Sec. 4.4. Parts of this chapter have been published previously in [18], [21] and [22]. For a recent review of searches for gamma ray features see [50].

4.1. The annihilation cross section

Before discussing the techniques used to search for line-like spectral features in the gamma-ray sky, it is interesting to identify the processes which contribute to dark matter annihilations, compare the different final states and single out the conditions under which they are relevant.

The first process which needs to be considered is the annihilation of WIMPs into pairs of SM
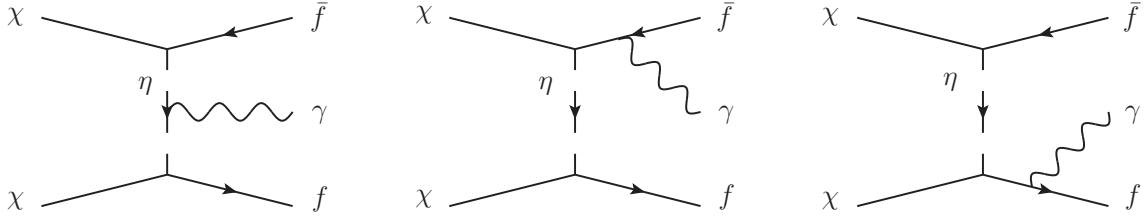
Figure 4.1.: Feynman diagrams of the processes that contribute to leading order to the three-body annihilation cross section and produce internal bremsstrahlung. This figure was originally published in [18].

fermions. After expanding the cross section into partial waves, the lowest order contribution in the dark matter velocity v to the s-wave is given by

$$(\sigma v)^{s\text{-wave}}_{2\text{-body}} = \frac{f^4 N_c}{32\pi m_\chi^2} \frac{m_f^2}{m_\chi^2} \frac{1}{(1+\mu)^2} \; , \tag{4.1.1}$$

where $\mu = (m_\eta/m_\chi)^2$ parametrizes the mass splitting between the dark matter χ and the scalar mediator η, m_f is the mass of the SM fermion in the final state and N_c is a colour factor which is one for leptons and three for quarks. Furthermore, the p-wave contribution to $\mathcal{O}(v^2)$ reads

$$(\sigma v)^{p\text{-wave}}_{2\text{-body}} = v^2 \frac{f^4 N_c}{48\pi m_\chi^2} \frac{1+\mu^2}{(1+\mu)^4} \; . \tag{4.1.2}$$

It is interesting that, on the one hand, the s-wave contribution is suppressed by helicity, i.e. scales like $(m_f/m_\chi)^2$, which is a fairly small number for all SM fermions except the top quark. On the other hand, the p-wave contribution is of higher order in the velocity and thus suppressed by the small value of the velocity $v \simeq 10^{-3}$ in the galaxy today. Consequently, the total tree-level annihilation cross section is very small and higher order corrections can become relevant.

A second class of processes which has been shown to contribute significantly to dark matter annihilations are three-body processes, known as internal bremsstrahlung (IB) or virtual internal bremsstrahlung (VIB) [1], in which a hard boson B is emitted in association with the fermion pair [52, 53, 54, 55, 56, 57, 58, 59, 60, 61, 62, 63, 23, 17, 64, 65, 66]. The additional boson in the final state lifts the helicity suppression and generates an s-wave contribution at $\mathcal{O}(m_f^0)$ such that the cross section of the $2 \to 3$ channel can be comparable or even dominate over $\sigma v(\chi\chi \to f\bar{f})$ even though it is suppressed by an additional power of the coupling constant and the three-body phase space. For the special case of photon emission we show the contributing Feynman diagrams in Fig. 4.1 [2]. The lowest order s-wave cross section for the emission of one

---

[1] The usage is not consistent in the literature. In the following we will use both expressions interchangeably.

[2] Note that the diagrams in Fig. 4.1 contribute both to IB and the well-known soft and collinear divergent final state radiation (FSR). These contributions interfere and a clear separation is only possible after expanding σv in v and m_f.
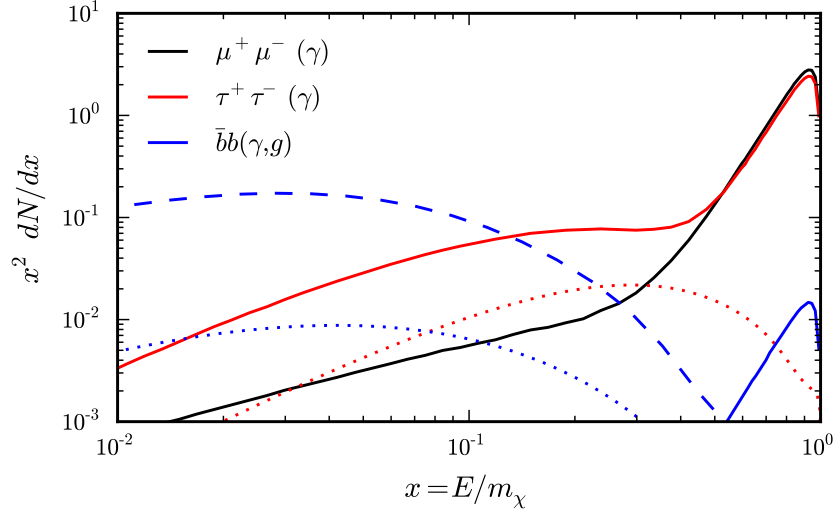
Figure 4.2.: Gamma-ray spectrum (N denotes the number of photons produced *per annihilation*) as predicted by our toy model for different flavours of final-state fermions, assuming $m_\chi = 200$ GeV and a mass-splitting of $\mu = 1.1$. *Solid lines* show contributions from three-body final states, including the IB photons close to $x = 1$; *dashed lines* show contributions from two-body final states (in case of muons, the two-body final state is strongly suppressed and not visible on the plotted scales). Branching ratios are calculated according to Eq. (4.1.1) and (4.1.3). Note that we convolve the spectra shown here with the Fermi LAT energy dispersion as derived from the instrument response functions (about $\Delta E \sim 10\%$ at around 100 GeV [51]) before fits to the data are performed. This figure was originally published in [18].

hard IB photon and a pair of massless Standard Model fermions can be expressed analytically and is given by [67, 58]

$$(\sigma v)_{\text{3-body}} \simeq \frac{\alpha_{\text{em}} f^4 N_c Q_f^2}{64\pi^2 m_\chi^2} \left\{ (\mu+1) \left[\frac{\pi^2}{6} - \ln^2\left(\frac{\mu+1}{2\mu}\right) - 2\text{Li}_2\left(\frac{\mu+1}{2\mu}\right) \right] \right.$$
$$\left. + \frac{4\mu+3}{\mu+1} + \frac{4\mu^2 - 3\mu - 1}{2\mu} \ln\left(\frac{\mu-1}{\mu+1}\right) \right\} , \qquad (4.1.3)$$

where Q_f is the electric charge of f in units of $|e|$ and $\text{Li}_2(z) = \sum_{k=1}^{\infty} z^k/k^2$ is the dilogarithm. This cross section can exceed the tree-level $2 \to 2$ cross section by orders of magnitude for sufficiently small values of μ. The most interesting property of this kind of process is that the energy spectrum of the gamma rays from IB peaks at energies close to the kinematic cut-off $E_\gamma = m_\chi$. The differential cross section of IB photons as a function of the photon energy fraction $x = E_\gamma/m_\chi$ reads

$$v\frac{d\sigma}{dx} \simeq \frac{\alpha_{\text{em}} f^4 N_c}{64\pi^2 m_\chi^2} (1-x) \left\{ \frac{2x}{(\mu+1)(\mu+1-2x)} - \frac{x}{(\mu+1-x)2} \right.$$
$$\left. - \frac{(\mu+1)(\mu+1-2x)}{2(\mu+1-x)^3} \ln\left(\frac{\mu+1}{\mu+1-2x}\right) \right\} . \qquad (4.1.4)$$
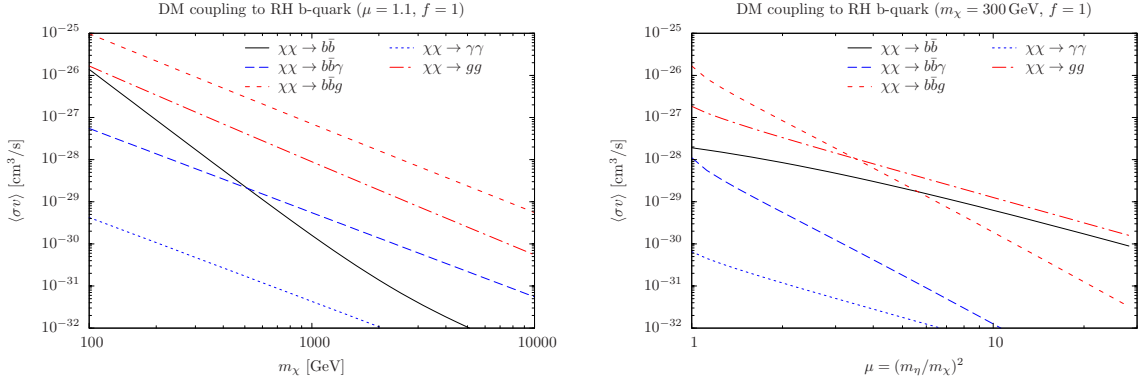
Figure 4.3.: Annihilation cross sections of a dark matter particle which couples via a Yukawa interaction to the right-handed bottom-quarks and a coloured scalar η. The left plot shows the cross sections as a function of the dark matter mass for fixed mass ratio squared $\mu = 1.1$, while the right plot as a function of the mass ratio squared μ for fixed dark matter mass $m_\chi = 300$ GeV. In both cases we adopted for definiteness a coupling $f = 1$. These figures were originally published in [21].

We report the differential cross sections for the other three body processes for $SU(2)_L$ singlet and doublet dark matter in Appx. B.

In order to visualize this behaviour we show three exemplary gamma-ray spectra in Fig. 4.2 for a dark matter mass $m_\chi = 200$ GeV, a mass splitting $\mu = 1.1$ and annihilations into μ, τ and bottom quarks in the final state. In this figure we include both photons from FSR and secondary photons generated in the decay or fragmentation of the SM fermion simulated with PYTHIA6.4 [68]. A further complication in the case of annihilations to quarks which needs to be taken into account arises from the annihilation $\chi\chi \to q\bar{q}g$ since the gluon final state is enhanced with respect to the photon by α_s/α_{em}. As becomes apparent from Fig. 4.2, photons from internal bremsstrahlung dominate the spectrum at the highest energies for small mass splittings and produce a pronounced peak close to m_χ, while secondary photons and FSR are only relevant at lower energies. Furthermore, it is interesting to note that while the total cross section depends strongly on μ, the form of the spectrum is fairly independent of the mass degeneracy for values of $\mu \lesssim 2$.

Finally, a third class of processes which is of importance for indirect detection is the loop-induced annihilation into pairs of gauge bosons $\chi\chi \to \gamma\gamma$, γZ, ZZ, WW, gg [69, 70, 71, 72]. These processes are suppressed by an even higher power of the coupling constant compared to the $2 \to 3$ process but have only a two-body phase space and generate an helicity-unsuppressed s-wave. The two most interesting final states are $\gamma\gamma$ and $Z\gamma$, both of which generate a gamma-ray line. As the analytic expressions for the cross section into these states are rather lengthy and cumbersome, we refer the reader to [69, 70, 71] and discuss their features qualitatively in the following.
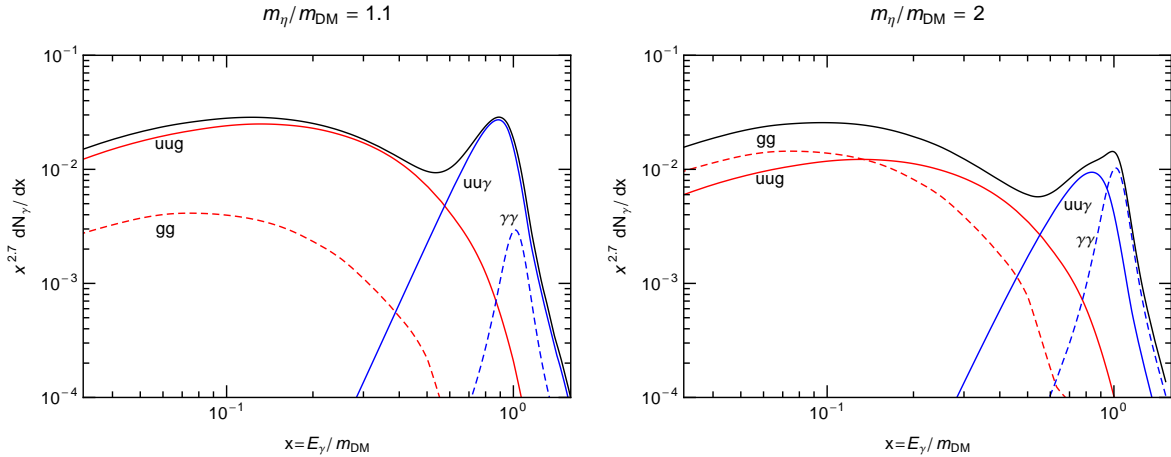
Figure 4.4.: Energy spectrum of gamma rays produced in the annihilation channels $u\bar{u}\gamma$, $\gamma\gamma$ as well as $u\bar{u}g$ and gg convolved with the Fermi-LAT energy resolution, for $m_\chi = 100\,\text{GeV}$, $m_\eta = 1.1 m_\chi$ (left panel) and $m_\eta = 2 m_\chi$ (right panel). The black line indicates the total spectrum. These figures were originally published in [22].

The relative importance of the different final states depends strongly on the masses of the different particles relevant for the annihilation, i.e. m_χ, m_η and m_f. We show in Fig. 4.3 the dependence of σv on the dark matter mass m_χ (left) and the mass degeneracy parameter μ (right) for the exemplary case of dark matter coupling to bottom quarks with a coupling $f = 1$. Note that photons from IB or $\gamma\gamma$ dominate the spectrum at the highest energies even for branching fractions $\text{BR} \lesssim 10^{-2}$. As can be seen, both the tree-level and the loop-induced $2 \to 2$ cross section scale as $1/\mu^2$ while three-body processes scale as $1/\mu^4$. Therefore, the loop induced annihilation into gauge bosons dominates the total cross section at large values of μ, while $2 \to 3$ channels receive a considerable enhancement as μ decreases. For example the intensity of photons from IB and from $\gamma\gamma$ are approximately equal for $\mu = 25$ with IB dominating at smaller values and loop induced photons at higher values. Current instruments do not have the energy resolution necessary to disentangle the contributions from IB and the gamma-ray line (see Fig. 4.4). In a full analysis spanning the complete parameter space the limits should therefore be derived based on the combined spectrum. However, the contribution of loop photons is negligible for small μ (see Fig. 4.4 (left)). As the total enhancement of the hard gamma spectrum is most pronounced for $\mu \sim 1$, we will focus on values $\mu \leq 2$ in the following analysis and neglect the photon line. However, in Ch. 5, when we revisit the constraints from searches for gamma-ray features in a less restricted parameter space, we consider the full spectrum in our statistical analysis.

4.2. Searching for gamma-ray features with Fermi-LAT

With current instruments the sharp gamma-ray peak from internal bremsstrahlung is virtually indistinguishable from a gamma-ray line, therefore, we adopt techniques developed for line

searches and modify them to better fit the needs of IB. As the signal of dark matter annihilation is highly concentrated in energy it is possible to restrict the analysis to a fairly narrow energy window, in practice only a few times the energy resolution of the instrument, around the dark matter mass. We assume that in such a small energy range the astrophysical background can be described locally as a simple power law, the spectral index and normalization of which we derive directly from the data. Since no detailed understanding about the origin of the background is necessary, it is possible to select difficult but highly promising target regions like the Galactic Center. In our analysis we focus on dark matter masses in the range $40\,\mathrm{GeV} \leq m_\chi \leq 300\,\mathrm{GeV}$. This choice for the lower end of the energy range is motivated by the lower limit on the mass of charged scalars from LEP $m_\eta \gtrsim 40\,\mathrm{GeV}$ [73] which excludes much lighter dark matter in the mass-degenerate scenarios $m_\chi \approx m_\eta$ considered here. The upper limit is due to the fact that dark matter heavier than 300 GeV would produce a spectral feature outside the energy range of Fermi-LAT.

4.2.1. Dark Matter signal from the galactic halo

Dark matter annihilations in the galaxy contribute to the gamma-ray flux from a given direction with an intensity which is proportional to the density squared integrated along the line of sight

$$\frac{dJ_\gamma}{dEd\Omega}(\xi) = \frac{\langle \sigma v \rangle}{8\pi\, m_\chi^2} \frac{dN}{dE} \int\limits_{\mathrm{l.o.s.}} ds\, \rho_\chi^2(r) \,, \tag{4.2.1}$$

where dN/dE represents the energy dependence of the gamma-ray spectrum produced in the annihilation and ξ is the angle to the Galactic Center. The integration variable $s \geq 0$ denotes the distance along the line of sight and the radial coordinate r, which measures the distance to the Galactic Center, can be expressed as $r(s,\xi) = \sqrt{(r_0 - s\cos\xi)^2 + (s\sin\xi)^2}$, where $r_0 = 8.5\,\mathrm{kpc}$ is the distance between the Solar System and the center of the Milky Way.

Here, we will consider a generalized Navarro-Frenk-White (NFW [74, 75]) profile

$$\rho_\chi(r) \propto \frac{1}{(r/r_s)^\alpha \, (1 + r/r_s)^{3-\alpha}} \,, \tag{4.2.2}$$

which we normalize to $\rho_\chi = 0.4\,\mathrm{GeV}\,\mathrm{cm}^{-3}$ at the position of the Earth [76, 77] and a scale radius $r_s = 20\,\mathrm{kpc}$. The standard NFW profile is recovered for $\alpha = 1$ while larger values of α, which are motivated as a mean to parametrize the effect of adiabatic contraction [78, 79, 80, 81], correspond to a steeper inner slope of the dark matter halo. We take values of α in the range $1 \leq \alpha \leq 1.4$ which are allowed by microlensing and dynamical observations [82].

4.2.2. Event and target region selection

The data measured by Fermi LAT is publicly available [83]. We consider 43 month of data taken between the Fourth of August 2008 and the Sixth of February 2012 and use only events from the
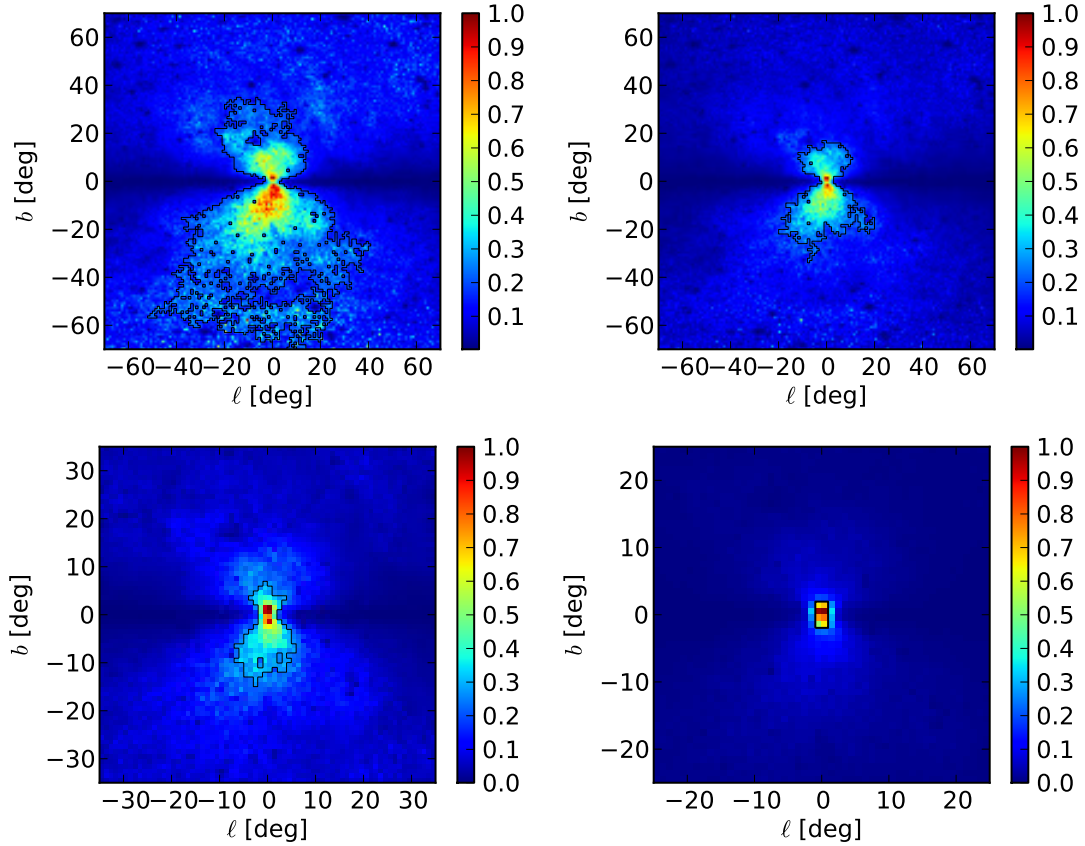
Figure 4.5.: Target regions used in our spectral analysis (solid black lines). From top left to bottom right, Reg1, Reg2, Reg3 and Reg4 are respectively optimized for DM profiles with inner slopes of $\alpha = (1.0, 1.1, 1.2, 1.4)$ as described in the text. The optimization maximizes the signal-to-*noise* ratio. For comparison, the colours show the expected signal-to-*background* ratio, normalized in each case to 1 for the central pixel. These figures were originally published in [18].

P7CLEAN_V6 event class. In our analysis we include both front- and back-converted events in the energy range 1–300 GeV. In order to minimize contamination by photons from the Earth Albedo we reject events with a zenith angle $\theta > 100°$ and apply a quality filter cut DATA_QUAL==1. We have used the 06/10/2011 version of ScienceTools v9r23p1 throughout our analysis.

In order to search for spectral features it is of utmost importance to select an appropriate target region since an inefficient region of interest can lead to unnecessary background levels and thus reduce the significance or even hide a signal. We optimize our signal region with a data-driven method based on the expected signal-to-noise ratio and determine optimal signal regions for four different generalized NFW halo models with $\alpha = 1.0$, 1.1, 1.2 and 1.4.

First, we divide the full data set into two distinct energy ranges, a low energy sample $1\,\mathrm{GeV} \leq E_\gamma \leq 40\,\mathrm{GeV}$, which we use in our optimization procedure, and a high energy sample $40\,\mathrm{GeV} \leq E_\gamma \leq 300\,\mathrm{GeV}$, which is employed in the actual search for IB. Next, we construct a

two dimensional equirectangular count map covering angles with $|b| \leq 90°$ in galactic latitude and $-90° \leq l \leq +90°$ in galactic longitude with a pixel size $\Delta b = \Delta l = 1°$. As the gamma-ray flux is falling rapidly with energy, the number of gamma ray events c_i observed in a given pixel i in the energy range $1\,\text{GeV} \leq E_\gamma \leq 40\,\text{GeV}$ is dominated completely by the lowest energies, i.e. events with $E_\gamma \approx 1\,\text{GeV}$. Under the assumption that the spatial distribution of the astrophysical gamma-ray emission at $1\,\text{GeV}$ and in the search region $40\,\text{GeV} \leq E_\gamma \leq 300\,\text{GeV}$ are similar we can use the low-energy data to estimate the spatial distribution of the background for our search. Furthermore, we can derive the expected number of signal events in a pixel μ_i from Eq. 4.2.1 up to an overall normalization. At this point the normalization is undetermined as we leave σv and dN/dE unspecified here. As the halo profiles considered here are all spherically symmetric, μ_i depends only on the angle ξ relative to the Galactic Center and the halo model parameter α. It should be noted that we neglect the angular resolution of Fermi-LAT, which is $\Delta\theta \lesssim 0.2°$ for $E_\gamma \geq 40\,\text{GeV}$. Now we can determine the expected signal-to-noise ratio as $R_i \propto \mu_i/\sqrt{c_i}$ where we have assumed that the signal is small compared to the background, i.e. $\mu_i \ll c_i$.

In principle the optimal target region is given by the set of pixels $\mathcal{T}_o$ which maximizes the total signal-to-noise ratio

$$\mathcal{R}_{\mathcal{T}_o} \equiv \frac{\sum_{i\in\mathcal{T}_o} \mu_i}{\sqrt{\sum_{i\in\mathcal{T}_o} c_i}} \,. \tag{4.2.3}$$

As there are in total $\sim 2^{180^2}$ possible combinations of pixels it is not feasible to calculate the optimal set $\mathcal{T}_o$ exactly by simple scanning. Instead, we use an iterative procedure to construct an approximate target region by using the following algorithm:

1. We start by selecting the pixel with the single highest signal-to-noise ratio $\mathcal{R}_i$ as a seed.

2. We check for every pixel not in $\mathcal{T}$ whether adding it increases the total $\mathcal{R}_{\mathcal{T}}$, then all pixels which were found to improve the total signal to noise ratio are included at once.

3. We determine for each pixel in $\mathcal{T}$ if its subtraction increases $\mathcal{R}_{\mathcal{T}}$ and remove all pixels for which we found $\mathcal{R}_{\mathcal{T}}$ to improve at once.

4. Step 2 and 3 are repeated until the number of pixels in $\mathcal{T}$ remains constant.

5. Finally, we clean up our sample by removing small regions which are disconnected from the main target region around the Galactic Center.

It should be mentioned that the removal of separated regions in step 5 of our algorithm has very little impact on our results and just cleans the border of the target region. Furthermore, we find only very little dependence on the initial seed and observe that the selection process always prefers regions around the Galactic Center.

We consider four values for the halo parameter $\alpha = 1.0$, 1.1, 1.2 and 1.4 and obtain four different target regions, Reg1, Reg2, Reg3 and Reg4 which are indicated in Fig. 4.5 with a solid black line. For illustration we use a colour code to show the expected signal-to-background ratio normalized to one for the pixel for which this ratio is maximized. As can be seen in Fig. 4.5, the

optimal target region is large for $\alpha = 1.0$ and reaches up to galactic latitudes $|b| \lesssim 70°$ while larger values of α lead to a drastic contraction of the target region and a strong concentration on the Galactic Center. General features which are present in all the regions are a certain north/south asymmetry which prefers the galactic south since the diffuse gamma-ray emission of our galaxy is stronger in the north. Furthermore, we find that the galactic disc is strongly disfavoured.

4.2.3. Spectral analysis

In our search for an IB feature in the gamma-ray spectrum we use a *sliding-energy-window* technique which has been discussed in the context of line searches in [84, 75, 85, 86] and choose a small energy window around a given dark matter mass. To be precise, we take the energy range to be $E = m_\chi \epsilon^{-0.7} \ldots \min[m_\chi \epsilon^{0.3}, 300 \, \text{GeV}]$, where ϵ is an energy dependent parameter which controls the width of the energy window. Numerically we use $\epsilon \simeq 1.8$ at 40 GeV and increase it to $\epsilon \simeq 7$ for $m_\chi = 300$ GeV. This parametrization of the window size is identical to the one used in Ref. [85], where it was shown explicitly to allow a good background fit for line searches. As the IB spectrum is expected to peak at energies $0.7 \, m_\chi \leq E_{peak} \leq 0.9 \, m_\chi$ the window taken here is not symmetric around the dark matter mass m_χ but shifted towards lower energies in order to increase the sensitivity. Furthermore, we want to stress that we expect secondary photons from decay and fragmentation to be irrelevant for our analysis as they do not contribute significantly to the gamma-ray flux in the energy window chosen in this analysis.

For each dark matter mass m_χ and a given mass splitting μ, we fit the gamma-ray spectrum measured in the corresponding energy window for the four target regions discussed in Sec. 4.2.2 with a three-parameter model. We describe the astrophysical background as a single power law with the spectral index and the normalization as free parameters while the IB-signal, the spectrum of which is fixed for a given choice of m_χ and μ, has only the normalization as a free parameter. Note that the IB normalization is required to be positive in order to be physical.

We perform a binned analysis of the measured gamma-ray spectrum in the energy window and divide the observed events into a large number of energy bins (200 per decade). Since the size of these energy bins is small compared to the energy resolution of Fermi-LAT this procedure is essentially equivalent to an unbinned analysis. In a given energy bin j we observe a number of events c_j. The expected number of events μ_j in bin j can be calculated by convolving our three-parameter model for the gamma-ray flux described above with the energy resolution and the exposure of the instrument. We infer the energy resolution directly from the instrument response function of the P7CLEAN_V6 event class and calculate the exposure maps with ScienceTools v9r23p1. Furthermore, we average properly over front- and back-converted events and take the effect of different impact angles into account using our own software. Now the signal can be fitted to the data by maximizing the likelihood function $\mathcal{L} = \Pi_j P(c_j | \mu_j)$ with respect to the three parameters of our model. Here $P(c|\mu)$ is the Poisson probability of observing c_j events when μ_j events were expected.

On the one hand, limits on the significance of a dark matter signal can be derived with the profile likelihood method [87]. In order to obtain one-sided 95% CL upper limits on the IB cross section we increase the normalization of the dark matter signal of our model while refitting the background parameters until $-2\ln\mathcal{L}$ increased by 2.71. On the other hand, the significance of a signal can be determined from the test statistics (TS)

$$TS = -2\ln\frac{\mathcal{L}_{\text{null}}}{\mathcal{L}_{\text{best-fit}}}\,,\tag{4.2.4}$$

where $\mathcal{L}_{\text{best-fit}}$ is the likelihood of the best fit and $\mathcal{L}_{\text{null}}$ the likelihood of the null hypothesis. As the dark matter signal is bound to be positive for physical reasons, TS is expected to follow a $0.5\chi^2_{k=0}+0.5\chi^2_{k=1}$ distribution (see e.g. Ref. [85]), where $\chi^2_{k=0}$ and $\chi^2_{k=1}$ have zero and one degree of freedom, respectively. A value for TS measured for a dark matter mass m_χ corresponds to a significance of slightly more than $\sqrt{TS}\sigma$.

Finally, we need to take into account that we perform more than one statistically independent trial. We scan both over m_χ and four different target regions, and thus the chance of finding a pure statistical fluctuation is increased. In order to take this so-called looking-elsewhere effect (LEE) into account we approximate the distribution of maximal TS value from which we determine the significance of our signal by $4\times4=16$ trials over a $\chi^2_{k=2}$ distribution. Four of our trials come from the four different target regions we consider, while the other four are due to the scan over m_χ (see Appx. C for details). Therefore, the global significance of an observed signal can be determined by solving $P(\chi^2_{k=2}<TS)^{\#\text{trials}}=P(\chi^2_{k=1}<\sigma^2)$ for σ, where $P(\chi^2_{k=2}<TS)$ is the probability of observing a value smaller than x when drawing from a χ^2_k distribution.

4.3. Significance of a gamma-ray spectral feature

We do not find a gamma-ray feature with a significance of more than 5σ in our analysis. Therefore, we derive the 95% CL upper limits on the IB cross section for $\mu=1.1$ in the four different target regions depicted in Fig. 4.5 and show the results in Fig 4.6. As can be seen the limits on the cross section for the three less contacted profiles, $\alpha=1.0$, 1.1 and 1.2, agree up to a factor ≤3 while the limits on the cross section for the steepest profile $\alpha=1.4$ can exceed the weaker limits by more than one order of magnitude. We are able to exclude cross sections larger than $10^{-26}\text{cm}^3\text{s}^{-1}$ for almost all masses and can even exclude cross sections as low as $10^{-28}\text{cm}^3\text{s}^{-1}$ for $\alpha=1.4$ and $m_\chi\lesssim100$ GeV. Furthermore, the grey cross in Fig. 4.6 indicates the theoretical prediction for the CMSSM benchmark point BM3 (stau coannihilation) of [53]. Unfortunately, it turns out that the theoretical expectation in this SUSY scenario still remains below the upper limits and IB features from stau coannihilation cannot be tested with current observations.

Even though we cannot claim the detection of a dark matter signal at 5σ, it is interesting to analyse the observed significance of a spectral feature in some more detail. We show in the left panel of Fig. 4.7 the TS value of an IB-feature for $\mu=1.1$ and the four target regions described in Sec. 4.2.2. As can be seen from the plot we find the highest significance for a dark matter
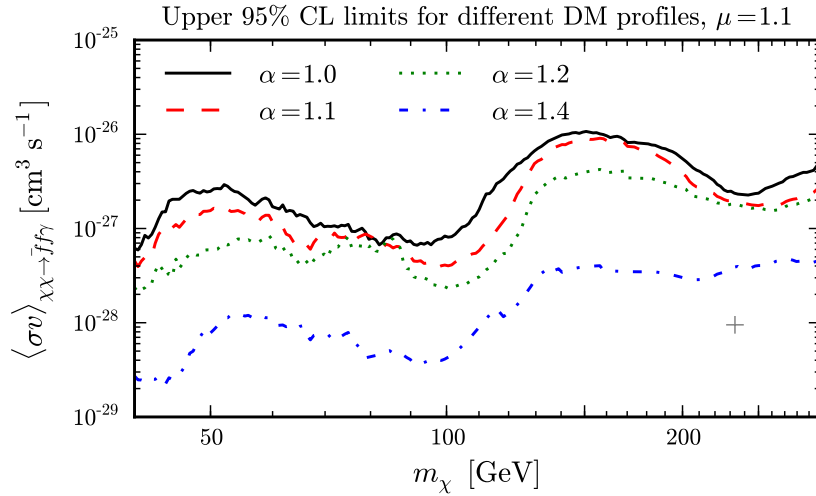
Figure 4.6.: Our results for the 95% CL limits on the *three-body* (IB) annihilation cross section of $\chi\chi \to \bar{f}f\gamma$, for different values of the dark matter profile inner slope α. The limits are obtained by a spectral analysis of the gamma-ray flux in the corresponding target regions shown in Fig. 4.5. We assume a mass splitting of $\mu = 1.1$. Note that the limits do not directly depend on the nature of the final state fermion f, as they are derived from the IB feature *only*. The gray cross shows the CMSSM benchmark point BM3 from Ref. [53]. This figure was originally published in [18].

mass $m_\chi \approx 150$ GeV in Reg2, and a similar, though less significant, indication for a gamma-ray excess in Reg1, Reg3 and Reg4. The local statistical significance of a dark matter contribution to the gamma-ray flux is $\sqrt{TS} = 4.3\sigma$, which corresponds to global significance of 3.1σ once the look-elsewhere effect is taken into account.

In the right panel of Fig. 4.7 we show the gamma ray data and the fit to the signal in Reg2 where the spectral feature is clearly visible by eye. It should be noted here that an IB signal from $m_\chi \approx 150$ GeV corresponds to a gamma-ray excess at $E_\gamma \approx 130$ GeV since the IB spectrum peaks at energies slightly below m_χ. The additional, less significant, fluctuation at 50 GeV is in complete agreement with statistical expectations and should not be taken as an indication for dark matter annihilations. Finally, we would like to comment on $TS = 0$ which we observe for certain mass ranges. This value of TS is essentially due to the fact that at these masses the fit prefers a negative normalization of the spectral feature such that, since we enforce a positive normalization, the likelihood of the best fit model becomes identical to the likelihood of the null model, i.e. $TS = 0$.

We investigate the possibility that our signal is due to some unexpected systematic error by performing a number of tests. On the one hand, masking different halves of the sky has no effect on the presence of the signal and we find an excess independently in four different parts of the sky (east, west, north and south). On the other hand, the signal vanishes completely once we shift the target regions by $10 - 20$ degrees away from the Galactic Center as expected
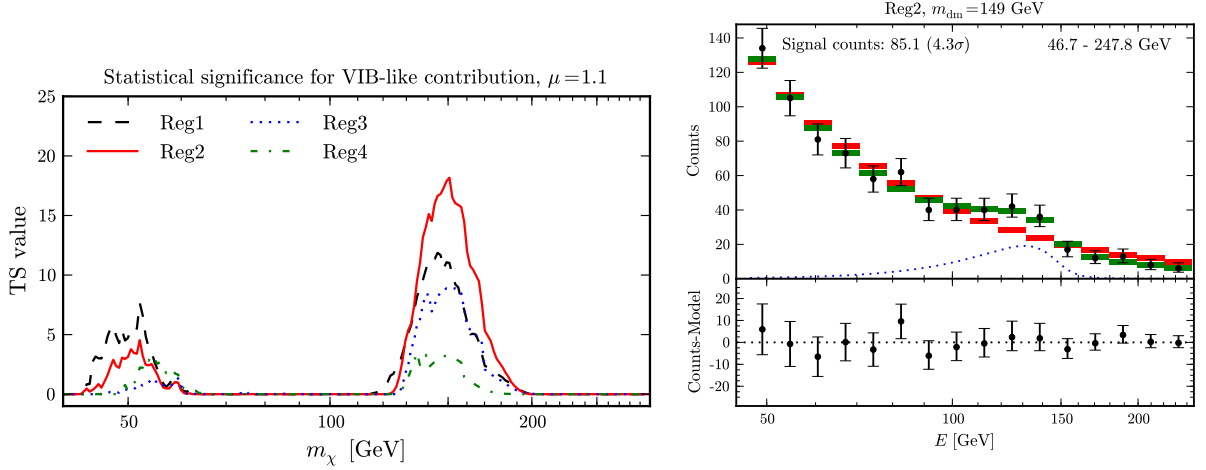
Figure 4.7.: Left panel: statistical significance for VIB-signal in terms of the TS value, as function of m_χ and for the different target regions shown in Fig. 4.5. Right panel: fits to data in Reg2 for the best signal candidate at $m_\chi = 149$ GeV. We show the background-only fit without dark matter signal as red bars. The green bars show the background plus DM signal fit, the blue line the corresponding VIB signal flux. In the right panel, we rebinned the data into (9 times) fewer bins than actually used in our statistical analysis in order to improve the optical appearance of the figure. Note that the shown fluxes are already integrated over the individual energy bins and properly convolved with the LAT IRF. These figures were originally published in [18].

for a genuine dark matter signal. Furthermore, an analysis of the P7ULTRACLEAN_V6 and P7SOURCE_V6 event classes reveals the same gamma-ray excess as do back- and front-end converting events separately. Finally, the uncertainty of the effective area is 2% [88] and thus much too small to account for the full signal flux. Neither of these tests is able to exclude a dark matter interpretation of the gamma-ray excess.

The best fit IB cross section is $\langle \sigma v \rangle = (6.2 \pm 1.5\ ^{+0.9}_{-1.4}) \times 10^{-27}$cm^{3}s^{-1} for $\alpha = 1.1$ and $m_\chi = 149 \pm 4\ ^{+8}_{-15}$GeV; the errors are respectively statistical and systematic [3]. The 130 GeV gamma-ray excess can also be fitted with a gamma-ray line from $\chi\chi \to \gamma\gamma$ with a cross section $\sigma v \simeq 10^{-27}$cm^{3}s^{-1} and a dark matter mass $m_\chi \simeq 130$ GeV. This interpretation has been under considerable scrutiny in the past two years and the presence of an excess at the $\gtrsim 3\sigma$ level has been confirmed in a number of independent studies [89, 90]. Recently the Fermi Collaboration published the results of their search for gamma-ray spectral features. Using reprocessed data with an improved energy resolution they find a decreased significance of 3.3σ locally [91].

---

[3]The systematic error is due to the uncertainty of the total effective area and the uncertainty of the energy calibration (cf. [88]).
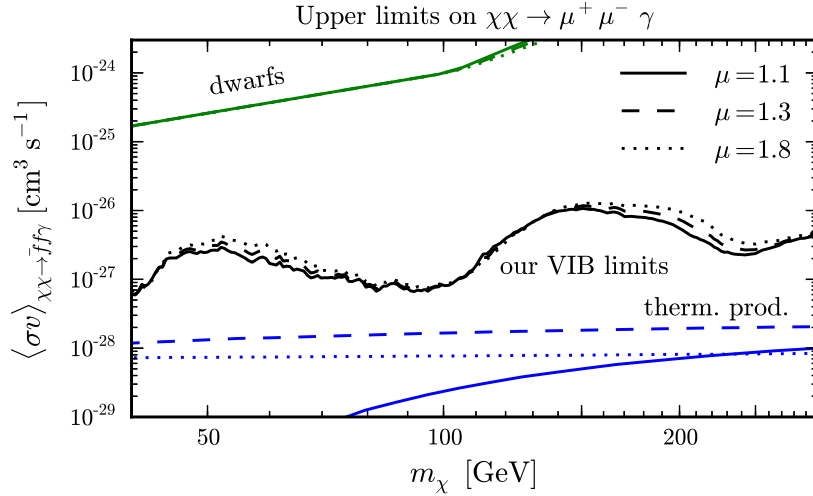
Figure 4.8.: Comparison of different upper limits on the three-body annihilation cross section of $\chi\chi \to \mu^+\mu^-\gamma$, for three reference values of the mass splitting μ. Black lines show 95% CL upper limits that come from our spectral analysis of the Galactic Center fluxes as shown in Fig. 4.6, assuming a standard NFW profile. Green lines (partially overlapping) show the corresponding limits derived from dwarf galaxy observations, taking into account both two- and three-body annihilation channels. Blue lines show upper limits on the annihilation cross section that are derived from requiring that the relic density predicted by our toy model does not *undershoot* the observed value. Updated version of figure published in [18].

4.4. Comparison with other constraints

In the following we will confront the limits from IB photons with other constraints. As the limits on σv_{3-body} were derived exclusively from the IB spectrum it is particularly interesting to assess how these limits compare to the bounds derived from the emission of continuum photons. Furthermore, we will analyse the implications of the upper limits for the cross section expected for a thermal relic, discuss the relevance of precision observables and comment on the contribution to the cosmic antiproton flux.

4.4.1. Continuum photons from dwarf galaxies

As is well-known, dwarf galaxies are one of the most promising targets for the observation of continuum gamma-rays from dark matter annihilations. Dwarf galaxies are expected to be among the most dark matter dominated objects in the universe while they host only moderate astrophysical activity and no relevant gamma-ray emission from astrophysical sources is expected. To date no excess over the background expectation has been measured from dwarf galaxies and there are stringent upper limits on the gamma-ray flux from dark matter annihilations [92, 93, 94]. In this work, we derive constraints on the three-body annihilation cross section based on the model
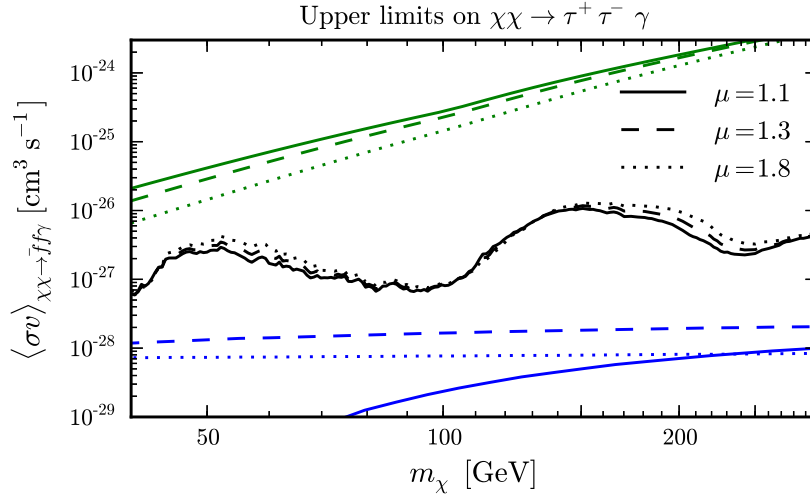
Figure 4.9.: Same as Fig. 4.8, but for annihilation into $\tau^+\tau^-\gamma$. Updated version of figure published in [18].

independent limits on the gamma-ray flux published in [94]. This bound can be parametrized as

$$\langle\sigma v\rangle < \frac{8\pi\ m_\chi^2}{N_\gamma^{\rm tot}} \cdot 5.0\times 10^{-30}{\rm cm}^3{\rm s}^{-1}{\rm GeV}^{-2}\ , \tag{4.4.1}$$

where $N_\gamma^{\rm tot}$ is the average number of photons emitted per dark matter annihilation in the energy range 1–100 GeV. We calculate $N_\gamma^{\rm tot}$ taking into account both the photons from the IB process and the tree level annihilation into fermion pairs. Note that we approximate the spectrum of low energy continuum gamma-rays from the three-body process with the spectrum from annihilations into $f\bar{f}$ thus overestimating $N_\gamma^{\rm tot}$ slightly.

We show the limits on the IB cross section for different values of μ and three different choices of the final state flavour in Figs. 4.8, 4.9 and 4.10. As can be seen from the plots, the limits derived from our search for a gamma-ray spectral feature exhibit only a mild dependence on the degeneracy parameter μ and are almost independent of the flavour of the fermions. This is essentially due to the fact that for moderate values of $\mu \lesssim 2$ the shape of the spectral feature has only a mild dependence on the mass splitting. The limits from dwarf galaxies exhibit a stronger dependence on μ for couplings to b quarks or τs, while in the $\mu^+\mu^-$ channel there is hardly any dependence at all since IB always dominates the total cross section in that case. Interestingly, the limits from the gamma-ray feature surpass those from continuum photons by orders of magnitude for dark matter coupling to leptons while the signal from dwarfs is more constraining for coupling to b quarks. The reason for this comparatively high sensitivity of dwarf searches to IB is that the process $b\bar{b}\gamma$ is always accompanied by $b\bar{b}g$, which has a huge branching fraction and produces a featureless gamma-ray spectrum.
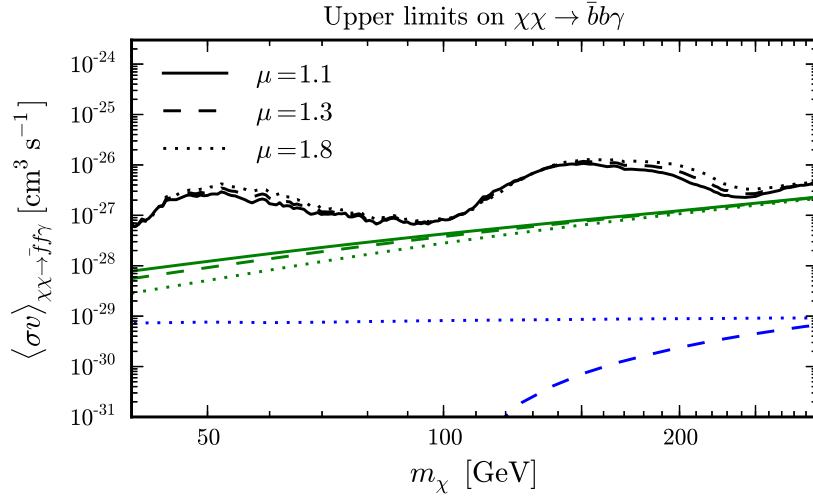
Figure 4.10.: Same as Fig. 4.8, but for annihilation into $\bar{b}b\gamma$. Note that we include $\bar{b}bg$ final states when calculating the dwarf limits [64, 17]. Updated version of figure published in [18].

4.4.2. Relic density

As already discussed in Sec. 3.2 we generically expect the relic density of this model to be given by Eq. 3.2.8. However, we are particularly interested in the regime of $\mu \leq 2$ and are therefore prone to corrections from coannihilations. We perform a full numerical calculation of the relic density with MicroMEGAS [40] and find that the analytic estimate of the relic density neglecting coannihilations is only approximately correct for $\mu \geq 1.3$ for leptons and $\mu \geq 1.8$ for dark matter coupling to bottom quarks.

With the results of our numerical simulation we are now able to calculate the three body annihilation cross section expected for a thermal relic. As apparent from Figs. 4.8-4.10 the upper limits from the search for a gamma-ray feature are still more than one order of magnitude away from the thermal expectation and we cannot hope to observe such a signature with Fermi-LAT unless either a astrophysical enhancement or a particle physics correction changes these results significantly.

4.4.3. Precision observables

Muon $g - 2$. For dark matter coupling to muons a dark matter-mediator loop can contribute to the muon $g - 2$. In our model the contribution to $g - 2$ can be written as [95]

$$\Delta a_\mu^{\text{DM}} = -\frac{f^2}{16\pi^2} \frac{m_\mu^2}{m_\chi^2} F(\mu) , \tag{4.4.2}$$

where $\mu \equiv (m_\eta/m_\chi)^2$ parametrizes the mass splitting, m_μ is the muon mass and the loop function $F(x)$ is given by

$$F(x) = \frac{2 + 3x - 6x^2 + x^3 + 6x \log x}{6(x-1)^4} \ . \tag{4.4.3}$$

As is well known, the measurement of $g - 2$ exhibits a long standing 3σ deviation from the theoretical expectation [96]

$$a_\mu^{\text{exp}} - a_\mu^{\text{SM}} = (29 \pm 9) \times 10^{-10} \ . \tag{4.4.4}$$

Unfortunately, the contribution from our dark matter model has the wrong sign and therefore any additional contribution can only worsen the agreement between theory and experiment. Since even the Standard Model is already excluded at 3σ we choose to interpret the current observation as a statistical fluctuation and demand that the total theoretical prediction should agree with the experiment at the 5σ level. In the limit $\mu \to 1$ the measurement constrains the coupling $y \lesssim 1.7(m_\chi/100\,\text{GeV})$, which corresponds to an upper bound on the cross section for $\chi\chi \to \mu^+\mu^-\gamma$ given by

$$\langle \sigma v \rangle_{\text{3-body}} < 2.5 \times 10^{-26} \text{cm}^3\text{s}^{-1} \left(\frac{m_\chi}{100\,\text{GeV}} \right)^2 \ . \tag{4.4.5}$$

Typically this limit is weaker than the bounds from gamma-rays presented in Fig. 4.6 and we do not get an additional constraint from $g - 2$.

Furthermore, the model considered here contains new scalar particles which are charged under $SU(2)_L \times U(1)_Y$ and can thus induce corrections to the oblique parameters S, T and U [97, 98]. However, as long as the scalar particle is an $SU(2)_L$ singlet, the three oblique parameters do not receive any exotic modifications.

4.4.4. Antiproton observations

In the case where the scalar η is colour charged the annihilation channel $\chi\chi \to q\bar{q}g$, which contributes to the cosmic antiproton flux due to the decay and the fragmentation of the gluon and the quarks, is allowed. As the gluon cross section is proportional to α_s^2 and not α_{em}^2, this process is enhanced with respect to the photon-IB channel by a factor ~ 100 [56, 99, 17, 64]. Therefore, the constraints on $q\bar{q}\gamma$ which can be derived from antiproton measurements are remarkably strong and can be comparable to or even stronger than the limits from gamma-rays for certain choices of cosmic-ray propagation parameters [17, 64], however, it should be noted that the uncertainty due to cosmic-ray propagation is large.

There is also a contribution to the antiproton flux in leptophilic model due to the $\chi\chi \to f\bar{f}Z$ channel which has a cross section comparable to $\chi\chi \to f\bar{f}\gamma$ for dark matter masses sufficiently larger than m_Z [100, 57, 60, 58, 23, 61, 17]. In this case the limits from antiprotons are less important and in the mass range $m_\chi \sim 100 - 300$ GeV antiproton limits are weaker than the bounds from our search for any choice of cosmic-ray propagation parameters.

4.5. Summary of internal bremsstrahlung searches

One of the main challenges for indirect dark matter searches is to find a reliable way to discriminate between an actual signal from dark matter annihilations and astrophysical backgrounds. Since a sharp gamma-ray feature, which could be created by annihilations into a pair of photons or by the internal bremsstrahlung process, cannot be mimicked by astrophysical sources this class of signatures are most promising for dark matter detection.

We adapted methods developed for line searches and conducted, for the first time, a dedicated search for an IB-like feature using 43 month of public Fermi-LAT data. Furthermore, we propose a new data-driven technique for the determination of the optimal target region based on the maximization of the expected signal to background ratio.

We derived upper limits on the annihilation cross section which exceed the limits from dwarf galaxies and antiproton measurements for dark matter coupling to leptons. However, we find that these limits fall short of the expected thermal cross section by about one order of magnitude and the exclusion of a heavy thermal relic remains impossible unless the annihilation rate is enhanced by astrophysical boost factors.

We find a weak indication for a gamma-ray excess at $E_\gamma \simeq 130$ GeV which could be explained by an internal bremsstrahlung feature from the annihilation of dark matter with a mass $m_\chi = 149 \pm 4 \; {}^{+8}_{-15}$GeV and a cross section $\langle \sigma v \rangle_{\chi\chi \to \bar{f}f\gamma} = (6.2 \pm 1.5 \; {}^{+0.9}_{-1.4}) \times 10^{-27}$cm^{3}s^{-1}. It is also possible to fit the signal with a gamma-ray line for a dark mass $m_\chi \simeq 130$ GeV and a cross section $\langle \sigma v \rangle_{\chi\chi \to \gamma\gamma} \sim 10^{-27}$cm^{3}s^{-1}. The local statistical significance of this signal is 4.3σ which corresponds to a global significance of 3.1σ once the look-elsewhere effect is taken into account. It should be noted that the preferred cross section is surprisingly large and is not easily explained by conventional models. So far no conclusive explanation of the excess has been found. However, a recent analysis by the Fermi Collaboration reported a decrease of the significance which could indicate a statistical fluctuation. Nevertheless, the observation of a gamma-ray feature remains an intriguing possibility for the detection of dark matter.

5. Direct Searches: Complementarity and Spin-dependent Sensitivity

The second main way to probe dark matter interactions with the Standard Model is the search for the scattering of WIMPs off SM matter. As the Earth is immersed in the dark matter halo of our galaxy, we expect a huge flux of dark matter particles through the Earth at any time. In direct detection we search for the energy deposit of dark matter recoiling against regular matter, usually nuclei, and thus probe the interactions between dark matter and the SM. However, the scattering cross section is expected to be very low and the observation of this signature requires a high level of background suppression, making the direct search for dark matter a technically very challenging endeavour. Nevertheless, the field has made tremendous progress in the last decade and pushes the sensitivity of direct detection experiments to unprecedented 10^{-45}cm^2. All considered, the current status of direct searches is rather puzzling. On the one hand, a number of experiments, for example DAMA [101], CRESST [102], CoGeNT [103] and CDMS-Si [104], observe anomalous recoil events compatible with a 10 GeVish dark matter particle. However, on the other hand, these observations are in tension with null results from XENON100 [4], LUX [5] or CDMS-Ge [105]. In the following we will remain agnostic as to the origin of these low mass signatures and concentrate on the uncontested limits on the interactions of higher mass dark matter.

In this chapter we will first discuss the theoretical interpretation of direct detection before deriving explicit limits on the Majorana Dark Matter Model presented in Sec. 3.1 and comment on the complementarity of direct and indirect detection. Finally, we argue that the spin-dependent interactions can contribute significantly to the recoil rate in XENON100 and could even be detected before spin-independent interactions in upcoming experiments. Parts of this chapter have been published previously in [19], [20] and [21]. Useful reviews of the various aspects of direct detection can be found in [106, 107, 108].

5.1. The recoil rate

As mentioned above, the key observable in direct detection experiments are nuclear recoil events induced by the scattering of dark matter off the detector material. Since the velocity of WIMPs in the galaxy is of order $10^{-3}c$, the scattering process is highly non-relativistic and the recoil

energy is given by

$$E_R = \frac{\mu_N^2 v^2 (1 - \cos\theta)}{m_N} \, , \qquad (5.1.1)$$

where m_N is the mass of the recoiling nucleus, $\mu_N = m_\chi m_N / (m_\chi + m_N)$ the dark matter nucleus reduced mass, v the relative velocity of the incoming particles and θ the scattering angle in the center of mass system. For dark matter masses $\mathcal{O}(10 - 100 \text{ GeV})$, typical values of the recoil energy are in the range $1 - 100$ keV, i.e. the energy scale of WIMP nucleus scattering is very small compared to the mass scale of dark matter. Therefore, the momentum transfer in the scattering process is negligible and dark matter nucleus scattering can be described as a contact interaction.

The differential recoil rate requires input from both astrophysics and particle physics and can be written as

$$\frac{dR}{dE_R} = \frac{\rho_0}{m_\chi m_N} \int\limits_{v_{min}}^{\infty} dv \, v f(v) \frac{d\sigma_{\chi N}}{dE_R}(v, E_R) \, , \qquad (5.1.2)$$

where ρ_0 is the local dark matter density and $f(v)$ is the local dark matter velocity distribution, while the lower limit of the integration is set by the minimal velocity $v_{min} = \sqrt{m_N E_R / (2\mu_N^2)}$ required to produce a recoil event with energy E_R and $d\sigma / dE_R$ is the differential WIMP nucleus cross section. Integrating the above equation over energy we obtain the total rate per kg $\times$ day

$$R = \int\limits_{E_T}^{\infty} dE_R \frac{\rho_0}{m_\chi m_N} \int\limits_{v_{min}}^{\infty} dv \, v f(v) \frac{d\sigma_{\chi N}}{dE_R}(v, E_R) \, , \qquad (5.1.3)$$

where E_T is the threshold energy below which a given detector is unable to measure the recoil reliably.

The astrophysical parameters ρ_0 and $f(v)$ are crucial for a reliable determination of the cross section $\sigma_{\chi N}$ and a precise determination of their value is highly desirable. Unfortunately, these parameters are hard to probe with current observations and there is a considerable uncertainty associated with them. Unless stated otherwise we will adopt a set of fiducial parameters which is well within the range of commonly considered values. In the following we use $\rho_0 = 0.4 \text{ GeV/cm}^3$ [76] and assume that the velocity distribution in the galactic rest frame is given by a truncated Maxwellian

$$f(v) = \frac{1}{\sqrt{2\pi}\sigma} \exp\left(\frac{-v^2}{2\sigma^2}\right) \Theta(v_{esc} - v) \, , \qquad (5.1.4)$$

where $v_{esc} = 544$ km/s [109] is the escape velocity and the velocity dispersion $\sigma = \sqrt{3/2} v_0$ is related to the local circular velocity $v_0 = 230$ km/s [108]. In principle, this velocity distribution is further modified by the movement of the solar system with respect to the galaxy and the rotation of the Earth around the sun, however, given the uncertainty of v_0 we do not take these effects into account here.

5.2. The direct detection cross section

The dark matter nucleus cross section depends on the microscopic interactions between the dark matter particle and the constituents of nuclear matter, i.e. quarks and gluons. Since the energy scale of recoil events in direct detection experiments is small compared to the mass scale of dark matter, these interactions can be described in terms of an effective Lagrangian $\mathcal{L}_{eff}$. Naturally, the coefficients of the effective operators have to be determined by matching to the appropriate amplitudes in the fundamental theory, however, by exploiting some properties of $\mathcal{L}_{eff}$ it is possible to simplify the problem considerably without subscribing to a full theory. In particular, as has already been noted in [110], the non-relativistic limit of axial-vector interactions describes interaction between the spins of the WIMP and the quarks, while scalar, vector and tensor interactions reduce to the same form and couple to the mass of the nucleus. Consequently, the differential scattering cross section $\mathrm{d}\sigma/\mathrm{d}E_R$ can be decomposed into a spin-independent (SI) and a spin-dependent (SD) cross section

$$\frac{\mathrm{d}\sigma_{\chi N}}{\mathrm{d}E_R} = \frac{\mathrm{d}\sigma_{\chi N}^{SI}}{\mathrm{d}E_R} + \frac{\mathrm{d}\sigma_{\chi N}^{SD}}{\mathrm{d}E_R} \; . \tag{5.2.1}$$

Furthermore, we need to take into account that for $E_R \gtrsim 10$ keV the wavelength associated with the momentum transfer $q = \sqrt{2m_N E_T}$ becomes comparable to the scale of the nucleus. When this happens the scattering process begins to resolve the inner structure of the nucleus and coherence is partially lost. Conventionally, this is taken into account by introducing a form factor $F(E_R)$ which is normalized to unity at zero momentum transfer, $F(0) = 1$. Thus, the differential cross section can be rewritten as

$$\frac{\mathrm{d}\sigma_{\chi N}}{\mathrm{d}E_R} = \frac{m_N}{2\mu_N^2 v^2} \left(\sigma_0^{SI} F_{SI}^2(E_R) + \sigma_0^{SD} F_{SD}^2(E_R) \right) \; , \tag{5.2.2}$$

where σ_0^{SD} and σ_0^{SI} are the SD and SI cross sections at zero momentum transfer and the appropriate form factors are included. In the following we will discuss each of these two interaction types separately.

5.2.1. Spin-dependent scattering

For fermionic dark matter the leading contribution to spin-dependent interactions is induced by coupling the dark matter current to the axial-vector quark current in the nucleus, as described by the following effective Lagrangian

$$\mathcal{L}_{eff}^{SD} = d_q \bar{\chi}\gamma^\mu\gamma^5\chi\bar{q}\gamma_\mu\gamma_5 q \; . \tag{5.2.3}$$

In order to calculate the WIMP nucleus cross section we need to evaluate the quark current in the nucleon and obtain

$$\langle n|\bar{q}\gamma_\mu\gamma_5 q|n\rangle = 2s_\mu^{(n)}\Delta q^{(n)} \; , \tag{5.2.4}$$

where $s_\mu^{(n)}$ is the spin of the nucleon and the coefficients $\Delta q^{(n)}$, which can be measured in polarized scattering experiments, parametrize the quark spin content of the nucleon. Having evaluated the nucleon matrix element it is possible to write down the effective Lagrangian for the SD interaction of dark matter with the nucleons

$$\mathcal{L}_{eff}^{SD} = d_q \bar{\chi} \gamma^\mu \gamma^5 \chi \bar{n} s_\mu n \sum_{q=u,d,s} 2 d_q \Delta q^n \ , \tag{5.2.5}$$

where we sum over the quark flavours which contribute to the total spin of the nucleon. After rewriting the coupling of dark matter to protons and neutrons as

$$a_p = \sum_q \frac{d_q}{\sqrt{G_F}} \Delta q^{(p)}, \ \ \text{and} \ \ a_n = \sum_q \frac{d_q}{\sqrt{G_F}} \Delta q^{(n)}, \tag{5.2.6}$$

the total spin-dependent cross section reads

$$\frac{\mathrm{d}\sigma_{\chi N}^{SD}}{\mathrm{d}E_R} = \frac{16 m_N}{\pi v^2} \Lambda^2 G_F^2 J(J+1) \frac{S(E_R)}{S(0)} \ , \tag{5.2.7}$$

where G_F is the Fermi constant, J the total spin of the nucleus and $S(E)$ is a form factor which parametrizes the effects of nuclear structure while the constant Λ is given by

$$\Lambda = \frac{1}{J} \left[a_p \langle S_p \rangle + a_n \langle S_n \rangle \right] \ . \tag{5.2.8}$$

For the presentation of the form factor it is convenient to replace a_p and a_n with the isoscalar coupling $a_0 = a_p + a_n$ and the isovector coupling $a_1 = a_p - a_n$. Then the total form factor which contains a pure isovector, a pure isoscalar and an interference term can be written as

$$S(E) = a_0^2 S_{00}(E) + a_1 a_0 S_{01}(E) + a_1^2 S_{11}(E) \ , \tag{5.2.9}$$

where the $S_{ij}(E)$ are structure functions which need to be determined from nuclear physics calculations.

In order to allow a better comparison of experimental results obtained with different target materials, i.e. in order to compare different WIMP nucleus cross section with each other, experiments report their results in terms of the SD-proton or -neutron cross section σ_p^{SD} and σ_n^{SD} under the assumption that only one of these terms is different from zero. In the case when only SD-proton scattering contributes

$$\sigma_{\chi N}^{SD} = \frac{\mu_N^2}{\mu_p^2} \langle S_p \rangle^2 \frac{4}{3} \frac{J+1}{J} \sigma_p^{SD} \ , \tag{5.2.10}$$

and the case of exclusive scattering off neutrons can be obtained with the appropriate replacements.

5.2.2. Spin-independent scattering

In contrast to SD interactions, the SI cross section can receive relevant contributions from a rather large set of effective operators: both couplings to quarks and gluons or even higher order operators can give sizeable contributions. Therefore, we postpone the discussion of the effective dark matter quark/gluon Lagrangian at this point and will revisit it later in the next section in the context of the simplified model introduced in Sec. 3.1.

For Majorana fermions spin-independent interactions at the WIMP nucleon level can be described in terms of an effective scalar Lagrangian

$$\mathcal{L}_{eff}^{SI} = f_n \bar{\chi}\chi \bar{n}n \; , \tag{5.2.11}$$

where n represents the proton or neutron and f_n is the coupling to the respective nucleon. The contributions from the different nucleons in a given nucleus interfere constructively such that we get the following expression for the dark matter nucleus scattering cross section

$$\sigma_0^{SI} = \frac{4\mu_N^2}{\pi} \left[Zf_p + (A-Z)f_n \right]^2 \; , \tag{5.2.12}$$

where Z and A are the proton and the mass number of the nucleus, respectively. As can be seen, the cross section is enhanced with A^2, leading to an improved experimental sensitivity to spin-independent interactions for heavy target nuclei. Finally, we need to take momentum transfer dependent decoherence effects into account and after including the form factor $F(E_R)$ the differential cross section reads

$$\frac{\mathrm{d}\sigma_{\chi N}^{SI}}{\mathrm{d}E_R} = \frac{m_N \sigma_0^{SI} F^2(E_R)}{2\mu_N^2 v^2} \; . \tag{5.2.13}$$

In a large class of models the coupling of dark matter to nucleons is isospin independent, $f_p = f_n$. It is customary to assume implicitly that this condition holds and present experimental results in terms of a single spin-independent direct detection cross section

$$\sigma_{\chi N}^{SI} = \frac{\mu_N^2}{\mu_p^2} A^2 \sigma_p^{SI} \; . \tag{5.2.14}$$

5.3. Complementarity of direct and indirect detection

Having established the theoretical framework necessary for the interpretation of direct detection experiments we can now exploit the wealth of observational data and put dark matter models to test. One intriguing possibility is to analyse the direct detection properties of the dark matter model described in Sec. 3.1 and analyse the complementarity between direct detection and searches for gamma-ray features.

5.3.1. Effective operators

The starting point from which the interactions of dark matter with the nucleons can be derived is the Lagrangian of our model

$$\mathcal{L}_{\text{int}}^{fermion} = -f\bar{\chi}\Psi_{Ri}\eta_i + \text{h.c.} \ , \tag{5.3.1}$$

which allows for direct interactions between dark matter and the quarks. The first and most obvious contribution to dark matter quark scattering is due to the s-channel exchange of the scalar η. This interaction induces spin-dependent and spin-independent scatterings off nucleons, while further contributions to SI scattering arise from loop level interactions with both the quarks and the gluons [107]. The leading contribution to SD interactions can be described by the dimension-six axial-vector dark matter quark interaction in Eq. 5.2.3 with a strength d_q given by

$$d_q = \frac{1}{8}\frac{f^2}{m_\eta^2 - (m_\chi + m_q)^2} \ . \tag{5.3.2}$$

Interestingly, in the case of SI scattering the coefficient f_q of the scalar term in the effective Lagrangian $\mathcal{L}_{\text{eff,scalar}}^{\text{SI}} = f_q\bar{\chi}\chi\bar{q}q$ vanishes for chiral interactions at dimension six and, furthermore, vector interactions $\bar{\chi}\gamma^\mu\chi\bar{q}\gamma_\mu q$ vanish to all orders since χ is a Majorana fermion. Consequently, the leading contribution to the SI coupling between dark matter and the nucleons has to be generated at higher order. Expanding the scalar exchange beyond dimension six, the first non-vanishing contribution arises from a dimension eight derivative term [111]

$$\mathcal{L}_{eff}^{SI} = g_q\bar{\chi}\gamma^\mu\partial^\nu\chi(\bar{q}\gamma_\mu\partial_\nu - \partial\bar{q}\gamma_\mu q) \ , \tag{5.3.3}$$

with the strength of the interaction given by

$$g_q = -\frac{1}{8}\frac{f^2}{(m_\eta^2 - (m_\chi + m_q)^2)^2} \ , \tag{5.3.4}$$

and thus suppressed compared to the spin-dependent interaction. As can be seen, both d_q and g_q are enhanced if the mass splitting is small which leads to an improved sensitivity of direct detection to mass-degenerate scenarios[1]. A further contribution to the dark matter nucleus coupling, which is subdominant for light quarks but can become relevant for quarks of the third generation, is induced by the scattering of dark matter off the gluon content of the nucleon via a scalar-quark loop, which generates a dimension-seven effective operator [107],

$$\mathcal{L}_{eff}^{gluons} = b\alpha_S\bar{\chi}\chi G_{\mu\nu}^a G^{a\mu\nu} \ , \tag{5.3.5}$$

where $G^{\mu\nu}$ is the gluon field strength tensor. The strength of this coupling is given by

$$b = \left(B_S - \frac{m_\chi}{2}B_{2S} - \frac{m_\chi^2}{4}B_{1S}\right) \propto f^2 \ , \tag{5.3.6}$$

---

[1]For light quarks both d_q and g_q seem to possess a pole for $m_\eta \to m_\chi$. However, it should be noted that the expansion which leads to these expressions is only valid while $m_\eta - m_\chi \geq \Lambda$, where Λ is the characteristic energy scale of the quarks in the nucleus. Conservatively, we always impose $m_\eta - m_\chi \geq 1$ GeV.

where the B_i represent loop functions which are reported in [111][2]. After evaluating the nuclear matrix elements the effective dark matter proton coupling reads

$$\frac{f_p}{m_p} \quad = \quad -\frac{m_\chi}{2}\sum_{q=u,d,s} f_{T_q}^{(p)}g_q \;-\; \frac{8\pi}{9}bf_{TG}^{(p)} \;-\; \frac{3}{2}m_\chi\sum_{q=u,d,s,b} g_q\left(q^{(p)}(2)+\bar{q}^{(p)}(2)\right) \quad , \quad (5.3.7)$$

where $f_{T_q}^{(p)}$ and $f_{TG}^{(p)}$ parametrize the quark and the gluon content of the proton respectively, while $q^{(p)}(2)$ and $\bar{q}^{(p)}(2)$ correspond to the second moments of the parton distribution functions (PDF).

The nuclear physics entering the calculation is encoded in a number of parameters: $\Delta q^{(p,n)}$ for SD scattering and $f_{T_q}^{(p,n)}$, $f_{TG}^{(p,n)}$, $q^{(p,n)}(2)$ and $\bar{q}^{(p,n)}(2)$ for SI interactions. It is possible to simplify the $f_{T_q}^{(p,n)}$ and $f_{TG}^{(p,n)}$ coefficient further and express them in terms of the π-nucleon sigma term $\Sigma_{\pi n}$ and the parameter σ_0 which can be determined in scattering experiments [112]. The fiducial values for these parameters can be found in [112, 113]. It should be noted that these parameters are known to be prone to uncertainties and in particular the uncertainty of the parameters $\Delta s^{(p,n)}$, $\Sigma_{\pi n}$ and σ_0 has a sizeable impact on the results [114]. Here, we use the values from [112]

$$\begin{aligned}
\Delta s^{(p)} &= \Delta s^{(n)} = -0.09 \pm 0.03\,, \\
\Sigma_{\pi n} &= 64 \pm 8 \text{ MeV}\,, \\
\sigma_0 &= 36 \pm 7 \text{ MeV} \quad .
\end{aligned} \qquad (5.3.8)$$

Furthermore, the uncertainty of the parton distribution function $u(x)$ $(d(x))$ is at the level of 10 to 25% (10 to 50%) as can be seen in Fig. 9 of [115]. In the following we always take the most conservative choice of nuclear parameters for our analysis, however, we later use the fiducial values in the discussion of collider limits in order to facilitate comparison with other works.

5.3.2. Experimental searches

As discussed in more detail in Chapter 4, the most prominent indirect detection signature in this model is the gamma-ray feature produced by the annihilation $\chi\chi \to f\bar{f}\gamma$ and the loop induced process $\chi\chi \to \gamma\gamma$. Apart from this contribution to the gamma-ray flux the model also predicts a sizeable dark matter nucleon scattering cross section which can be enhanced significantly for small mass differences $\Delta m = m_\eta - m_\chi$. In the following we will describe briefly the method used in our analysis and comment shortly on the additional data used with respect to the analysis presented in Chapter 4.

Spectral features and indirect detection

Apart from Fermi-LAT the Galactic Center has also been observed by the H.E.S.S. Cherenkov telescope which recently published an analysis of 112h of data collected in four years [8]. The

---

[2]The analytic expressions in [111] contain errors, the appropriate corrections are reported in [107].

target region selected by H.E.S.S. is a narrow cone with a radius of $1°$ around the Galactic Center. Additionally, $|b| \geq 0.3°$ is required in order to exclude the galactic disk and thus suppress the astrophysical background. The main background is due to misidentified cosmic-ray protons even though stringent cuts were employed to reduce this contamination. Using this data, the H.E.S.S. collaboration performs a search for a spectral feature and reports limits on the flux of photons both from a gamma-ray line and internal bremsstrahlung in the range from $500\,\mathrm{GeV} - 25\,\mathrm{TeV}$.

A further improvement of the limits on spectral features with future experiments can be achieved by a better energy resolution, a larger effective area or a better background suppression. In the following we will consider the prospects of two projected gamma ray telescopes, the GAMMA-400 satellite experiment [116] and the ground based Cherenkov Telescope Array (CTA) [117]. On the one hand, GAMMA-400 is a prime example for an instrument with an excellent energy resolution as it aims to achieve an accuracy at the percent level in energy while the effective area is expected to be a modest $\mathcal{O}(1\mathrm{m}^2)$. CTA, on the other hand, is going to possess a huge effective area with $A_{eff} \simeq 0.02, 0.3, 2.3\,\mathrm{km}^2$ at energies of 100 GeV, 1 TeV and 10 TeV, respectively [118].

Note that the hard gamma-ray spectrum in the model considered here is always given by a superposition of a gamma-ray line and an internal bremsstrahlung feature. As we consider a large range in μ we always take the full mass dependence of the gamma-ray spectrum into account. In our analysis we compute the differential gamma-ray flux as seen from the Earth under the angle ξ with respect to the Galactic Center,

$$\frac{d\Phi}{dEd\Omega} = \frac{1}{4\pi} \left(\frac{d\sigma v_{q\bar{q}\gamma}}{dE} + 2\sigma v_{\gamma\gamma}\delta(E - m_\chi) \right) \int_0^\infty ds \, \frac{1}{2} \left(\frac{\rho_\chi(r)}{m_\chi} \right)^2 , \qquad (5.3.9)$$

where $r = \sqrt{(r_0 - s\cos\xi)^2 + (s\sin\xi)^2}$, $r_0 = 8.5\,\mathrm{kpc}$. Here the radial dark matter distribution is taken to be given by an Einasto profile

$$\rho_\chi(r) \propto \exp\left(-\frac{2}{\alpha_E} \left(\frac{r}{r_s} \right)^{\alpha_E} \right) , \qquad (5.3.10)$$

with $\alpha_E = 0.17$ and scale radius $r_s = 20\,\mathrm{kpc}$ [119], normalised to $\rho_0(r_0) = 0.4\,\mathrm{GeV/cm}^3$. This primary energy spectrum has to be convoluted with the energy resolution of Fermi-LAT [120] and H.E.S.S. [8], respectively. Finally, we use a binned profile likelihood analysis and derive one-sided 95% CL upper limits on a dark matter signal on top of a smoothly varying background spectrum, which was fitted to the Fermi-LAT data presented in [121] (search region 3, Pass7 SOURCE sample) and the H.E.S.S. data from [8] (CGH region). For Fermi-LAT we employ the same energy range and the same background parametrization as in Ch. 4 while we follow [8] closely for the search conducted with the H.E.S.S. Cherenkov telescope. Comparing our results for a pure gamma-ray line with the limits reported in [121, 8] we find agreement better than 20% in the complete energy range.

Furthermore, we calculate the expected limit for CTA and GAMMA-400 by generating a large number of background-only data samples with Poissonian fluctuations around the expected

background flux in each energy bin. Each of these mock data samples is then analysed for a signal and we determine the expected upper limits on a gamma-ray feature by averaging the individual upper bounds on a logarithmic scale. For modelling GAMMA-400 we follow [122] and use the search region, observation time, background flux, effective area and energy resolution given therein, however, we employ the same parametrization of the energy window as in Ch. 4 since this is optimized for internal bremsstrahlung searches. Comparing our prospected limits for a gamma-ray line with [122] we find good agreement. In the case of CTA we use the effective area and energy resolution from [118] (MPIK settings) and assume 50h of observations of a region with a 2° radius around the Galactic Centre. Our background model for CTA consists of the gamma-ray emission close to the Galactic Centre measured by H.E.S.S. and misidentified cosmic-ray electrons and protons. We adopt the same electron and proton fluxes as in [86] and assume a proton/photon discrimination efficiency of 1% and an absolute observation probability of 80%. Finally, we employ the same background parametrization as in Ch. 4 and use a sliding energy window $(m_\chi/\epsilon^{0.7}, m_\chi\epsilon^{0.3})$ with $\epsilon = 3$ (4) at $m_\chi = 1$ (10) TeV. A comparable approach is used in [123].

Direct searches

In this analysis we use the latest results from the XENON100 experiment [4]. The XENON collaboration has collected 225 live days of data with an effective exposure of 2323.7 kg days. In this data set 2 WIMP-like recoil events were observed in the energy window $E_R = 6.6 - 30.5$ keV while 1.0 ± 0.2 background events were expected. Using the Feldman-Cousins procedure [124] we obtain a 95% CL upper limit on the total number of recoil events $N \leq 5.72$ which can be translated into an upper limit on the coupling f for a given set of dark matter mass m_χ and scalar mass m_η. We use the limit on the total recoil rate and not the upper limit on the spin-independent cross section reported by the collaboration and, therefore, derive implicitly constraints on the model parameters from the combined bound on spin-dependent and spin-independent interactions. For the calculation of our prospects we use the expected sensitivity of XENON1T [125].

5.3.3. Results for coupling to quarks

In this section we will present the limits on interactions with up or bottom quarks derived from direct and indirect detection. Furthermore, we discuss the prospects for future experiments and comment on the complementarity of projected direct and indirect detection experiments.

Current limits for coupling to quarks

Searches for a gamma-ray feature are sensitive to the high energy gamma-rays produced either by internal bremsstrahlung or by a gamma-ray line. Annihilations into a gamma-ray line should
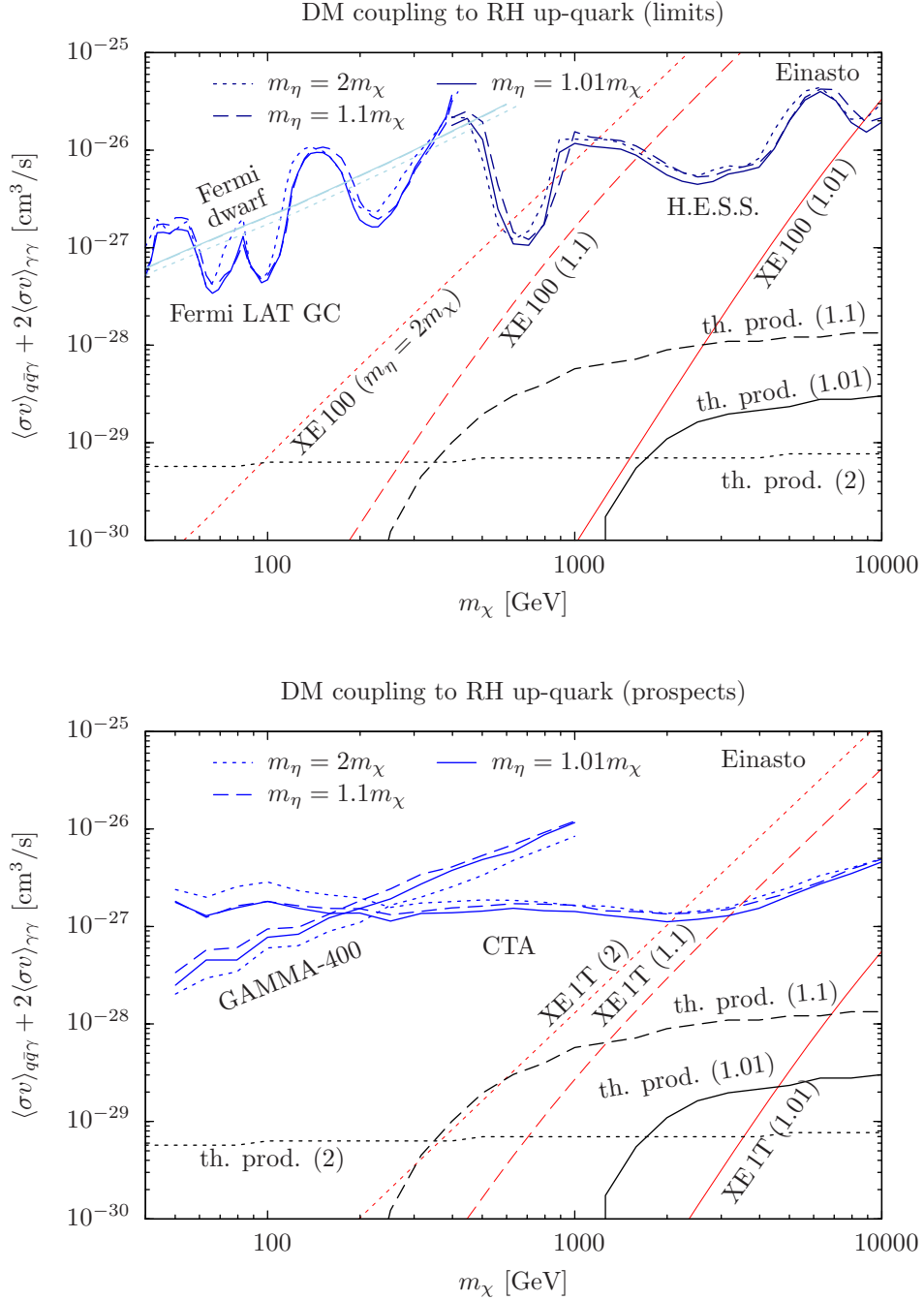
Figure 5.1.: Upper limits (95% CL) on the annihilation cross section obtained from searches for a spectral feature in the gamma-ray spectrum using Fermi-LAT and H.E.S.S. observations (blue lines), for three values of the mass splitting $m_\eta/m_\chi = 1.01, 1.1, 2$ and assuming an Einasto profile. Also shown are complementary constraints from direct searches (XENON100, red lines) and constraints on secondary gamma rays from Fermi-LAT observations of dwarf galaxies (light blue lines), both of which were translated into limits on the annihilation cross section $\langle \sigma v_{q\bar{q}\gamma} \rangle + 2\langle \sigma v_{\gamma\gamma} \rangle$. The black lines indicate the cross section expected for a thermal relic. The lower frame shows an estimate for the upper limit that can be achieved by searches for spectral features by GAMMA-400 and CTA, respectively, as well as the prospect for XENON1T. Here, we assumed that dark matter interacts with right-handed up-quarks. These figures were originally published in [21].
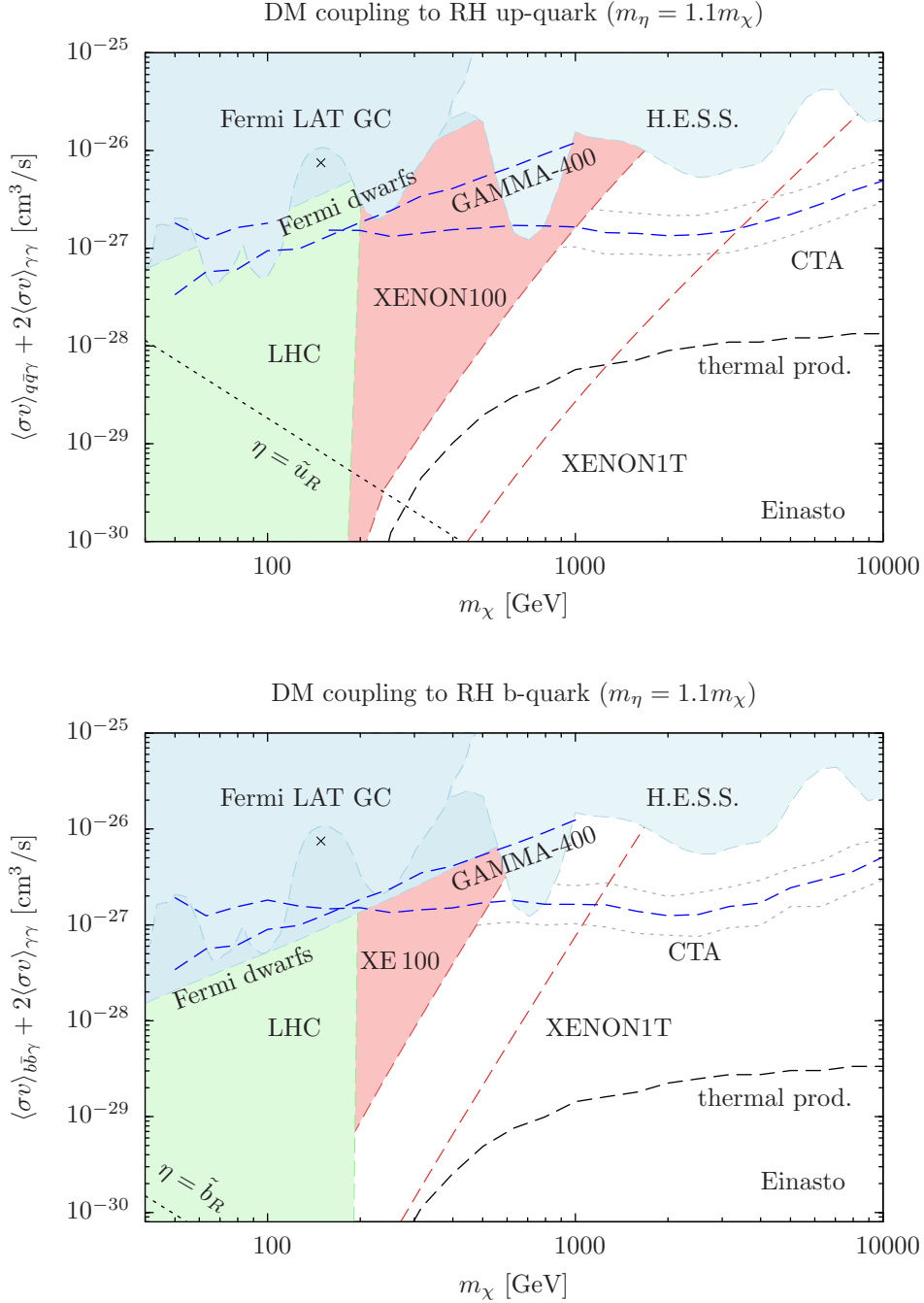
Figure 5.2.: Comparison of future prospects for searches for spectral features in gamma-rays (GAMMA-400, CTA) and direct searches (XENON1T) in the case where dark matter couples to right-handed up- and bottom-quarks, respectively in the top and bottom frames, and $m_\eta/m_\chi = 1.1$. The shaded areas are excluded by various present experiments as discussed in the text. The dashed black line shows the cross section expected for a thermal relic, and the dotted black line refers to the case where the Yukawa coupling is fixed to $f = 0.33$ (0.16) for u (b), as is appropriate in the supersymmetric case. The dotted grey lines correspond to the $\pm 1\sigma$ range for the expected upper limit for CTA. These figures were originally published in [21].

be considered for $m_\eta \gtrsim 2m_\chi$ and we present therefore upper limits on the combined cross section $\sigma v_{q\bar{q}\gamma} + 2\sigma v_{\gamma\gamma}$. However, this implies that we need to adapt the previous analysis of Fermi-LAT data [18] and the H.E.S.S. search [8] as these consider only pure internal bremsstrahlung. In Fig. 5.1 (top), we show the resulting upper limits (95% CL) obtained for $q = u_R$ and three values of the mass ratios $m_\eta/m_\chi = 1.01, 1.1, 2$, ranging from $10^{-27}-10^{-26}$ cm^3/s for $m_\chi = 40-10^4$ GeV. As can be seen, the observational limits depend only mildly on the mass splitting. On the one hand, the limits on a pure IB feature worsen slightly when m_η/m_χ increases as the peak of the spectrum gets broadened [18]. On the other hand, this tendency only holds until the contribution from the gamma-ray line becomes relevant as the line leads to a more strongly peaked spectrum such that the limits improve with increasing $\sigma v(\chi\chi \to \gamma\gamma)/\sigma v(\chi\chi \to q\bar{q}\gamma)$. Once both effects are included, we observe that the limits first degrade slightly up to $m_\eta/m_\chi \sim \mathcal{O}(2-4)$ before becoming slightly stronger again. The dependence on the mass ratio typically remains small. Furthermore, as can be seen from Fig. 5.2, the limits exhibit only a weak dependence on the quark flavour. Note that only the observational limits depend weakly on the mass splitting; the theoretical expectations for a thermal relic or a fixed coupling depend quite strongly on the mass splitting.

The limit from the observation of dwarf galaxies constrain the production of secondary gamma-rays, most of which arise from the $\chi\chi \to q\bar{q}g$ final state. The Fermi-LAT bounds on this channel are basically independent of the mass splitting and the quark flavour since any dependence of the low energy spectrum on these parameters is washed out after fragmentation and hadronization. The translation of the limits on $\sigma v_{q\bar{q}g}$ into limits on $\sigma v_{q\bar{q}\gamma}$ is mainly given by the branching ratios into these channels and, consequently, the bounds on annihilations into bottom quarks exceed those on up quarks by a factor $Q_u^2/Q_d^2 = 4$. As becomes apparent in Fig. 5.2, the limits from dwarfs on dark matter coupling to bottom quarks are stronger than limits from line searches up to dark matter masses of a few hundred GeV while the line search limits on coupling to up quarks become competitive at lower energies. Finally, we would like to stress that the relative strength of theses two searches depends strongly on the dark matter distribution in dwarf galaxies and in the center of the Milky Way and, therefore, their comparison should be taken with a grain of salt.

Furthermore, the interactions of dark matter with quarks can be tested by direct detection experiments. As explained earlier in this section, the scattering rate receives an enhancement for small mass splittings $m_\eta - m_\chi$. For $m_\eta/m_\chi = 1.1$ the constraints from XENON100 dominate over the limits from indirect detection up to dark matter masses $m_\chi \lesssim 2$ (cf. the top frame of Fig. 5.1). Furthermore, the limits get even stronger for very small splittings and can exceed the limits from Fermi-LAT and H.E.S.S. up to dark matter masses of 8 TeV for $m_\eta/m_\chi = 1.01$. However, larger mass splittings lead to weaker bounds and, for $m_\eta/m_\chi = 2$, the limits from direct detection become comparable to the bounds from H.E.S.S. at $m_\chi \gtrsim 500$ GeV. Dark matter coupling to bottom quarks cannot be probed as efficiently by direct detection experiments, therefore, the bounds weaken by about one order of magnitude compared to dark matter coupling to up quarks

(cf. Fig. 5.2). Nevertheless, limit on scenarios with coupling to bottom quarks are still competitive and dominate over Fermi-LAT and H.E.S.S. limits on spectral features for $m_\chi \lesssim 600$ GeV if $m_\eta/m_\chi = 1.1$. It is interesting to note that the dark matter interpretation of the tentative 130 GeV gamma-ray excess discussed in Ch. 4 and indicated by a cross in Fig. 5.2 is firmly excluded by XENON100 in models of dark matter with couplings to quarks.

Finally, we want to caution that these results are only valid in the simplified Majorana dark matter model considered here. While we expect minor extensions of the model, like for example the presence of another scalar or coupling to left-handed quarks, to leave our main results unchanged, it is not possible to draw robust conclusions if more general extensions of the model are considered.

Prospects

Today the sensitivity of both direct and indirect detection is progressing very fast. We can expect that current limits on gamma rays will soon be superseded by observations with GAMMA-400 [116], DAMPE [126] or CTA [117] while XENON1T [127], SuperCDMS [128], EURECA [129] or DARWIN [125, 130] promise to improve the limits on the direct detection cross section by up to three orders of magnitude. Consequently, it is interesting to assess the future prospects of these two detection strategies in the context of mass-degenerate models. We present in Fig. 5.1 (bottom) the expected 95% CL exclusion limit of XENON1T, GAMMA-400 and CTA for three mass ratio $m_\eta/m_\chi = 1.01, 1.1, 2$ for dark matter coupling to up quarks. As can be seen, GAMMA-400 is expected to dominate the bounds from indirect detection up to $m_\chi \sim 200$ GeV while CTA is more constraining at higher masses. Interestingly, the expected limits from CTA exhibit a rather flat behaviour in energy up to a few TeV. This can be understood from the fact that the effective area of CTA increases rapidly with energy in this range and thus compensates the usual m_χ^{-2} dependence induced by the decreasing dark matter number density. Similar to Fermi-LAT and H.E.S.S., the dependence of the gamma-ray constraints on the mass ratio m_η/m_χ remains weak, however, some slight differences with respect to the current limits arise. In particular we observe that the dependence of the GAMMA-400 sensitivity on the mass splitting is inverted relative to CTA. While CTA is most sensitive to a strongly peaked internal bremsstrahlung feature, i.e. to small values of m_η/m_χ, the constraints from GAMMA-400 are strongest for $m_\eta/m_\chi = 2$. The reason for this is that the excellent energy resolution of GAMMA-400 allows to distinguish between an IB feature and a line. The constraints improve since a line becomes more prominent at large mass splittings, i.e $m_\eta/m_\chi = 2$. In this context it should be kept in mind that the energy resolution of Fermi-LAT, H.E.S.S. and CTA does not allow to discriminate between internal bremsstrahlung and a gamma-ray line, and both signatures would be observed as a local distortion of the spectrum. Additionally, we show the projected upper limit from XENON1T in Fig. 5.1 (bottom). As can be seen these limits exhibit the same behaviour with m_η/m_χ as the XENON100 bounds depicted in Fig. 5.1 (top) and discussed in the previous subsection. If dark matter is coupled to up quarks, the projected limits from XENON1T are

excellent for mass-degenerate scenarios and can even test models with quite significant mass differences. For example, we find that the constraints from XENON1T can exceed the limits from indirect detection up to $m_\chi \sim 2-3$ TeV.

In Fig. 5.2 we show a collection of current and future constraints on dark matter coupling to up and bottom quarks for an exemplary mass ratio $m_\eta/m_\chi = 1.1$. As can be seen, we expect the prospected limits from GAMMA-400 to be more stringent than current bounds from Fermi-LAT and to improve by a factor of a few with respect to them. Furthermore, the sensitivity of CTA exceeds H.E.S.S. limits by up to one order of magnitude due to its impressive effective area. We would like to stress that these prospects are conservative and it is quite possible that a better understanding of the instrument might lead to more optimistic conclusions regarding the physics potential. Nevertheless, the precise mapping of the gamma-ray sky provided by highly sensitive experiments, e.g. example H.E.S.S. or Fermi-LAT, does not allow for orders-of-magnitude improvements.

Finally, a comment regarding the complementarity of direct and indirect searches for mass degenerate scenarios is in order. As can be seen in Fig. 5.2, the limits from XENON100 preclude the observation of a spectral feature with GAMMA-400 for couplings to up or bottom quarks and a mass splitting of 10%. Furthermore, similar conclusions hold in a wide range of mass splittings and are not restricted to the 10% case we use for illustration here. Conversely, if we observe an internal bremsstrahlung feature with GAMMA-400, direct detection implies that the gamma-ray feature cannot be attributed to dark matter coupling to light quarks easily. However, leptophilic scenarios do not suffer from such a tension and remain a plausible interpretation of a gamma-ray spectral feature (see Appx. D).

Another most interesting result concerns the complementarity between CTA and XENON1T. As becomes apparent from Fig. 5.2, CTA, on the one hand, is going to improve the limits on spectral features throughout the entire mass range $m_\chi = \mathcal{O}(10)$ GeV $- \mathcal{O}(10)$ TeV in an almost mass independent manner. On the other hand, XENON1T is limited to dark matter masses less than a few TeV, but possesses a sensitive to extremely small cross sections in that mass range. Therefore, the complementarity of indirect and direct detection is excellent and we find that CTA and XENON1T explore the parameter space in a fashion which is almost orthogonal. Furthermore, there is a region of parameter space in which dark matter could be detected by XENON1T and CTA at the same time. In this case the correlation between the different signals could provide valuable information about the properties of dark matter and would strengthen the case of mass degenerate scenarios.

5.4. The spin-dependent sensitivity of XENON100

In light of the excellent sensitivity of XENON100 to spin-independent scattering it is timely to analyse its sensitivity for spin-dependent interactions. Current direct detection experiments can be divided into two classes; experiments either designed to have an excellent sensitivity to

| | ^{129}Xe | | | ^{131}Xe | | |
	$\langle S_p \rangle$	$\langle S_n \rangle$	S_{ij}	$\langle S_p \rangle$	$\langle S_n \rangle$	S_{ij}
"Bonn A"	0.028	0.359	Bonn A [136]	−0.009	−0.227	Bonn A [136]
"Engel"	0.028	0.359	Bonn A [136]	−0.041	−0.236	Engel [137]
"Nijmegen II"	0.0128	0.300	Nijmegen II [136]	−0.012	−0.217	Nijmegen II [136]
"Bonn CD"	−0.0019	0.273	Bonn CD [138]	−0.00069	−0.125	Bonn CD [138]
"Menendez+"	0.010	0.329	Menéndez et al [139]	−0.009	−0.272	Menéndez et al [139]

Table 5.1.: The spin expectation values $\langle S_{p,n} \rangle$ and structure functions S_{ij} of the target nuclei ^{129}Xe and ^{131}Xe. This table was published previously in [20]

the SD or to the SI scattering cross section. More precisely, experiments using light neutron or proton odd target materials, e.g. ^{19}F (COUPP [131] and PICASSO [132]), are mainly sensitive to SD interactions while, due to the A^2 enhancement of the cross section, SI dark matter nucleus scattering can be probed more efficiently with high mass nuclei, e.g. Ge (CDMS [133]), Xe (XENON100 [134] and LUX [5]) or W (CRESST [135]). Nevertheless, SI experiments with high mass target nuclei can have a good sensitivity to the SD cross section, provided there are proton or neutron odd isotopes with a sizeable natural abundance. As is well-known [15, 16], xenon detectors are well suited to constraining SD interactions since the neutron-odd isotopes ^{129}Xe and ^{131}Xe have a significant natural abundance. In 2012 the XENON100 collaboration has published their most constraining measurement to date corresponding to the results of 255 live days of data taking [4] during which they observed no excess above the expected background [3]. In this section we will explore the sensitivity of XENON100 to SD interactions and point out that upcoming ton-scale direct detection experiments in addition to their impressive projected SI limits are certain to probe SD interactions to an unprecedented level. Furthermore, we investigate the effect of the uncertainty of nuclear structure functions and show that SD-proton scattering cannot be probed robustly with xenon detectors unless nuclear calculations provide more precise structure functions. Finally, we demonstrate the importance of SD constraints by analysing their impact in two well motivated particle physics models.

5.4.1. Experimental results and nuclear uncertainty

The XENON100 experiment has observed 3 WIMP-like recoil events in the energy window $E_R = 6.6 - 30.5$ keV, and expects a background of 1.0 events. We calculate the 95% CL upper limit using the Feldman-Cousins procedure [124] and find for the number of dark matter induced recoil events the upper limit $N_R \lesssim 4.91$. A more advanced statistical analysis, e.g. a full likelihood analysis, could exploit further information and is expected to give more stringent limits, however, the method employed here is conservative and thus fit for a phenomenological reanalysis [4]. Once

---

[3]Even though the SI limits of XENON100 have been superseded by LUX [5], XENON100 still provides the best SD limits since LUX has not released their SD results. A reliable reinterpretation of the LUX SI results is not feasible as they were derived using a full likelihood analysis of all recoil events.

[4] After the publication of [20] the XENON100 Collaboration released a SD analysis of their data based on a full likelihood analysis [140]. The limits on the SD cross sections reported by them are stronger then our results by a factor $\lesssim 2$ which proves the validity of our analysis.

the upper limit on N_R is known we can use the procedure described in Ref. [141] and translate it into an upper limit on the SD-proton and SD-neutron cross sections $\sigma_{p,n}^{SD}$, or into a combination of these cross sections.

In order to allow for a better comparison with other experimental results, we deviate in this analysis from our default parameters and use the "standard halo model" [108] with a local dark matter density $\rho_0 = 0.3\,\mathrm{GeV/cm^3}$, a local circular velocity $v_0 = 230$ km/s, a mean Earth velocity $v_E = 244$ km/s and a local escape velocity $v_{esc} = 544$ km/s. Although this set of parameters, which is based primarily on [108] and on [109] for v_{esc}, is subject to astrophysical uncertainties [109, 142], we choose to use it here since it is commonly adopted in the experimental community and allows for a fairer comparison of our results with the literature. The main remaining uncertainties in this analysis are the nuclear parameters, most prominently the structure functions S_{00}, S_{11} and S_{01} of the two contributing xenon isotopes. In an attempt to quantify the total nuclear uncertainty we consider five different nuclear models, the details of which are specified in Tab. 5.1. Three of these, namely "Bonn A" [136], "Engel" [137] and "Nijmegen II" [136] are rather canonical parametrizations, while "Bonn CD" [138] and "Menendez+" [139] were derived from more recent nuclear models.

We encounter two problems in our attempt to quantify the nuclear uncertainty of the SD-proton cross section. On the one hand, we find that the combination relevant for the SD-proton cross section, $S_{00} + S_{11} + S_{01}$, is extremely small in the "Bonn CD" parametrization and appears to be dominated by numerical errors in the energy range of interest here. If taken at face value, these structure functions translate into an upper limit on the SD scattering cross section which is weaker by a factor ~ 1000 than the constraints derived using other nuclear models. On the other hand, the "Menendez+" parametrization provides an error estimate for S_{01} and S_{11}. If these errors are combined naively, the total SD structure function $S_{00} + S_{11} + S_{01}$ is no longer guaranteed to be different from zero and the sensitivity to SD-proton scattering can vanish completely. However, the errors are most likely correlated and such a combination is not permissible. Since the information necessary to include these errors in the appropriate way is not available we do not consider them in the following. These two issues imply that the nuclear uncertainty of SD-proton scattering might be significantly larger than the spread of the canonical models [136, 137] indicates. All considered, a better understanding of the nuclear structure functions is necessary if reliable limits on the SD-proton cross section are to be derived from xenon based experiments. The combination of structure functions relevant for SD-neutron scattering, $S_{00} + S_{11} - S_{01}$, is more robust and does not suffer from any of these issues.

In Fig. 5.3 we show the 90% CL upper limits on the SD-proton (left) and SD-neutron (right) cross-sections from XENON100 and compare them with the best experimental bounds from the literature. We indicate the five different nuclear parameter sets discussed in the previous paragraph by the thick, short dashed, dotted, long dashed and dot-dashed red lines. As can be seen, the effect of nuclear uncertainties on the XENON100 limits is quite large. In particular, the SD-proton limits are very sensitive to the choice of nuclear model and it should be noted that
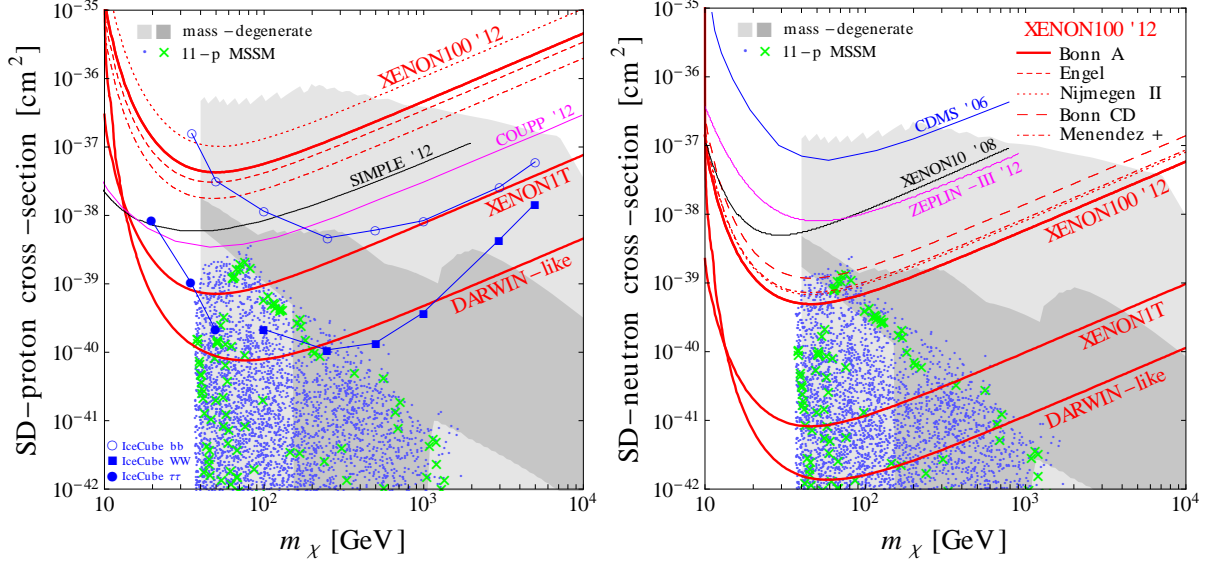
Figure 5.3.: XENON100 90% CL exclusion limits for pure proton (left) and pure neutron (right) SD cross-sections. Shown are the results for five nuclear structure parametrizations: "Bonn A" [136] (thick red), "Engel" [137] (short dashed red), "Nijmegen II" [136] (dotted red), "Bonn CD" [138] (long dashed red) and "Menendez+" [139] (dot-dashed red). The prospects for XENON1T and a DARWIN-like experiment are indicated by the lower thick red curves. For a pure proton coupling (left) additional limits are available from IceCube [143, 144] bb (empty blue circles), WW (filled blue squares), $\tau\tau$ (filled blue circles), SIMPLE '12 [145] (black) and COUPP '12 [131] (magenta). For a pure neutron coupling (right) limits from CDMS '06 [146] (blue), XENON10 '08 [15] (black) and ZEPLIN-III '12 [16] (magenta) are given for comparison. Notice that the "Bonn A" and "Engel" models lead to very similar results on σ_n^{SD} and thus the corresponding limits are indistinguishable, whereas the "Bonn CD" model yields a very weak σ_p^{SD} constraint above the plotted range. The light grey area represents the region of the mass-degenerate model as described in the text, while the dark grey region exhibits the measured relic density. Furthermore, we show a scan of the 11-parameter MSSM with the light blue dots; the green crosses indicate the points of the parameter space yielding the measured relic abundance. These figures were published originally in [20].
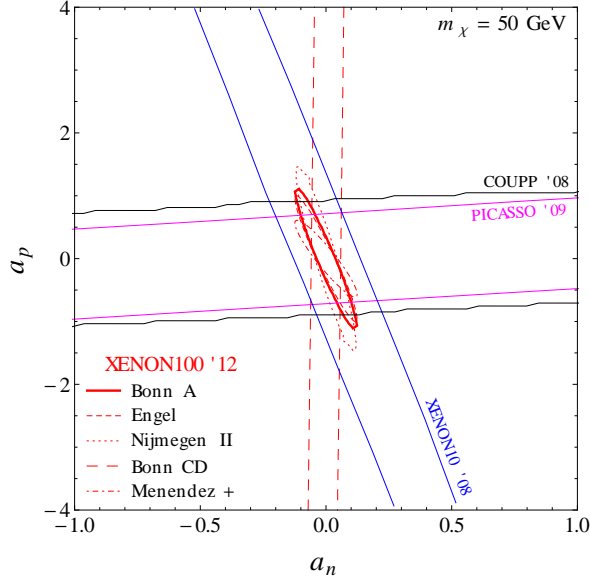
Figure 5.4.: 90% CL exclusion region in the a_n - a_p parameter space for a WIMP mass of 50 GeV. The line code is as in Fig. 5.3. We also show the limits from XENON10 '08 [15] (blue), COUPP '08 [147] (black) and PICASSO '09 [132] (magenta). This figure was published in [20].

the limits using the "Bonn CD" set-up are completely outside of the plot range. Essentially this means that it is not possible to derive robust limits on σ_p^{SD} from xenon based experiments, however, the effect of nuclear uncertainties on σ_n^{SD} is rather mild and typically $\lesssim 2$. Furthermore, XENON100 limits on SD-proton scattering are not competitive and lag considerably behind SIMPLE and COUPP even for an optimistic choice of nuclear parameters. XENON100 constraints on the SD-neutron cross-section, on the other hand, are by far the most stringent limits and surpass previous results by about one order of magnitude.

In addition to the bound from direct detection experiments mentioned above, there are limits on SD interactions from mono-jet searches at the LHC which can reach a sensitivity of 10^{-40} cm^2 for axial-vector contact interactions [148, 13, 149]. However, these limits have been derived using an effective operator approach, the applicability of which is questionable if the interactions are mediated by an additional light degree of freedom [150, 151, 152]. Furthermore, there are stringent bounds on SD scattering from neutrino telescopes, however, these are not completely model independent and rely on the equilibration of capture and annihilation rate which has not necessarily been reached today (see e.g. [153] for a scenario without equilibrium).

Furthermore, we show in Fig. 5.3 the prospects for the projected experiments XENON1T and DARWIN assuming the "Bonn A" structure functions. In the case of XENON1T we use prospects presented in [125] and estimate the sensitivity to be 60 times better than in XENON100 whereas for modelling a DARWIN-like detector we follow [154] and assume 2.00 ton.yr of effective xenon exposure and a background level of one event in the energy range $E_R = 10 - 100$ keV. We
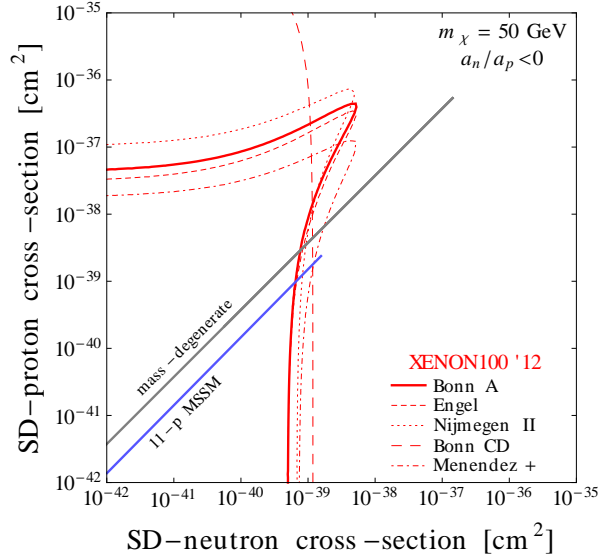
Figure 5.5.: 90% CL exclusion region in the σ_n^{SD} - σ_p^{SD} parameter space for a WIMP mass of 50 GeV and $a_n/a_p < 0$. The line code is as in Fig. 5.3. Also shown is the theoretical expectation in the mass-degenerate model (grey) and in the 11-parameter MSSM (light blue). This figure was published previously in [20].

find that the prospects depicted in Fig. 5.3 are very encouraging and constraining SD-neutron cross-sections of $10^{-42} - 10^{-41}$cm^2 appears to be possible with future experiments. If we assume the "Bonn A" form factors, XENON1T has the potential to probe SD-proton cross sections beyond the current limit from SIMPLE and COUPP while DARWIN could even compete with neutrino telescopes. However, we need to caution that a robust interpretation of xenon based experiments in terms of SD-proton requires an improved understanding of nuclear structure.

As the issues which plague the SD-proton interactions do not influence the sensitivity to SD-neutron interactions the potential of future experiments should be taken very seriously. In the next section we will show explicitly in the framework of two different well-motivated dark matter models that the expected limits on the SD-neutron cross section of experiments such as XENON1T and DARWIN are able to rule out region of parameter space which cannot be probed by their SI interactions. Needless to say, for a fair comparison with other experiments it should be kept in mind that not only xenon based experiments but also LHC searches [148], neutrino telescopes [155] and SD direct detection experiments such as COUPP [156] are going to improve in the next decade.

Fig. 5.4 depicts the XENON100 90% CL limits on the effective coupling to neutrons and protons $a_{n,p}$ for $m_\chi = 50$ GeV and compares then to previous limits. Even though nuclear uncertainties can once again degrade the limits significantly, it is nonetheless clear that XENON100 contributes important information and constraints the parameter space considerably in a direction which is not probed by COUPP and PICASSO efficiently. Finally, we present in Fig. 5.5

the limit on the combined SD cross section for $m_\chi = 50$ GeV and $a_n/a_p < 0$. This choice for the sign of a_n/a_p is based on the theoretical expectation in the particle physics models we discuss in the next section.

5.4.2. Study of particle physics models

In the following we will demonstrate the importance of the XENON100 limits on the SD cross section in two exemplary dark matter models, the simplified model for dark matter interacting with up quarks introduced in Sec 3.1 and the MSSM. We begin by considering the simplified model and take the Yukawa coupling f, the dark matter mass m_χ and the mass degeneracy parameter $m_\eta/m_\chi \gtrsim 1$ to be free parameters.

As discussed earlier in this chapter both the SD and the SI cross section receive a considerable enhancement if the mass splitting is small. For a fixed mass ratio $m_\eta/m_\chi \gtrsim 1$, the relative importance of the SD and SI interactions depends strongly on the dark matter mass and, using Eq. 5.3.2 and Eq. 5.3.4, we find the relation $\sigma_p^{SD}/\sigma_p^{SI} \propto d_u^2/(m_\chi g_u)^2 \propto m_\chi^2$ between the different scattering cross sections. Consequently, the total recoil rate will always be dominated by SD scattering provided the dark matter mass is sufficiently heavy. Similarly, for any given dark matter mass the direct detection rate is always dominated by SD interactions for a sufficiently large mass ratio m_η/m_χ. In order to identify the conditions under which SD scattering dominates over SI interactions we scan the parameter space $(f, m_\chi, m_\eta/m_\chi)$ of the model in the ranges $10^{-4} \leq f \leq 10$, $m_\chi \geq 40$ GeV, $10^{-2} \leq m_\eta/m_\chi - 1 \leq 10^2$ and $m_\eta - m_\chi > 1$ GeV. The last condition is necessary to ensure the validity of the expansion leading to the effective Lagrangian with the couplings as given by Eq. 5.3.2 and Eq. 5.3.4. We require that each parameter point is in agreement with collider searches, namely ATLAS [157], L3 [158] and monophoton searches [159], and exclude points with a SI cross section above the upper limit from XENON100. Projecting the resulting parameter space into the dark matter mass m_χ and the SD cross section $\sigma_{SD}^{(n)}$ plane, we obtain the light gray region in Fig. 5.3. The dark grey shading indicates regions in which thermal freeze-out yields the correct dark matter relic density. As can be seen, the constraints on the SD cross section are able to rule out a significant part of the parameter space which is in agreement with the SI limits. This confirms our earlier estimate that there are non-negligible regions in parameter space for which the recoil rate in xenon based experiments is dominated by SD scattering. The result of the scan can also be seen as the grey line in Fig. 5.5 for $m_\chi = 50$ GeV. Note that in this model the relative strength of the proton and neutron coupling is fixed by the relative abundance of up quarks in the nucleons, $a_n/a_p = \Delta u^{(n)}/\Delta u^{(p)} \simeq -0.52$, such that the parameter space of the scan reduces to a line in Fig. 5.5.

Another interesting model to consider is the MSSM. Given the stringent bounds from collider searches and the observed Higgs mass $m_h \simeq 125$ GeV, thermal dark matter is highly constrained in some of the more restrictive realizations of supersymmetry, for a discussion of the post-LHC status of supersymmetric dark matter in the constrained minimal supersymmetric Standard Model (CMSSM) see [160, 161, 162, 163]. Furthermore, if the constraints on the SI scattering

Parameter	M_1	M_2	$|\mu|$	$m_{\tilde{q}_{1,2}^L}$	$m_{\tilde{q}_{1,2}^R}$	$m_{\tilde{q}_3^L}$	$m_{\tilde{q}_3^R}$	$m_{\tilde{\ell}}$	$\tan\beta(M_Z)$	m_A	A_t
Min [GeV]	10	80	80	1000	1000	500	500	80	5	500	-4000
Max [GeV]	2000	2000	2000	3000	3000	3000	3000	3000	25	2000	4000

Table 5.2.: Parameter ranges for the MSSM scan. The gluino mass parameter is fixed to $M_3 = 2$ TeV, $A_{u,d,b} = 0$ and $m_{\tilde{\ell}} \equiv m_{\ell,i}^{L,R}$. All parameters except $\tan\beta$ and the pole mass m_A are given at $Q = 1$ TeV. This table was published previously in [20].

cross section from XENON100 are imposed on the parameter space the allowed SD cross section is typically below $10^{-42}\,\mathrm{cm}^2$ [162] and thus undetectable even with future experiments like XENON1T or DARWIN.

However, it is important to keep in mind that the conclusions drawn in the CMSSM depend on the severe restrictions imposed by the model and need not hold in more general realizations of supersymmetry. In order to determine the implications of lifting these assumptions we perform a random scan of an 11-parameter MSSM with DarkSUSY [164]. We vary the parameters of the model within the ranges indicated in Tab. 5.2 and impose constraints from LEP, Tevatron, $b \to s\gamma$ and the ρ-parameter, which are implemented in DarkSUSY 5.0.5, and require a Higgs mass in the range $m_h = 125.5 \pm 1.5$ GeV. Since light squarks are constrained severely by LHC searches and a dedicated analysis of LHC limits on the squark sector is beyond the scope of our work, we impose conservative limits on the squark masses $m_{\tilde{q}_{1,2}} > 1.5\,\mathrm{TeV}$ and $m_{\tilde{q}_3} > 500\,\mathrm{GeV}$ which are allowed within simplified models containing squarks, gluino and a nearly massless neutralino [165, 166]. Furthermore, all points are required to be compatible with the XENON100 limits on the SI scattering cross sections and contribute to the gamma-ray flux from dwarf galaxies at a level allowed by [93]. We show the range of SD cross sections that is in agreement with all experimental constraints in Fig. 5.3 (blue circles) and the range of point with the correct relic density (green crosses). We find that both regions overlap and the relic density is not correlated with a suppressed SD interactions. Quantitatively we find SD cross sections as large as $10^{-39}\,\mathrm{cm}^2$ for neutralino masses around 100 GeV which decreases to $10^{-41}\,\mathrm{cm}^2$ at $m_\chi \simeq 1000$ GeV. Here, the neutralino is a mixed bino-higgsino state and the correct relic density is achieved by annihilations with a Z in the s-channel or t-channel chargino exchange. Interactions with scalar superpartners contribute only little to the relic density since the large squark masses suppress the cross section efficiently.

In the case with heavy sfermions and a mixed bino-higgsino as dark matter, the dominant contribution to SI interactions is Higgs exchange, while SD scattering is mainly caused by Z exchange [112]. The leading effects governing the relative importance of SD and SI scattering in this scenario can be understood by considering the lowest-order contributions to the effective Lagrangian given by

$$\mathcal{L} = \alpha_{2i}\bar{\chi}\gamma^\mu\gamma^5\chi\bar{q}_i\gamma_\mu\gamma_5 q_i + \alpha_{3i}\bar{\chi}\chi\bar{q}_i q_i \,, \tag{5.4.1}$$

where the first term induces SD and the second term SI interactions. For simplicity we consider only quarks of the first generation, $i = u$ or d, in the following argument, however, we include

twist-2 operators and loop-induced couplings in our numerical analysis. In the decoupling/heavy squark limit, the coefficients for a neutralino $\chi = Z_{\chi 1}\tilde{B} + Z_{\chi 2}\tilde{W} + Z_{\chi 3}\tilde{H}_u + Z_{\chi 4}\tilde{H}_d$ are given by (we use the notation of [112])

$$
\begin{aligned}
\alpha_{2i} &= -\frac{g^2 T_{3i}}{8 M_Z^2 c_W^2}\left(|Z_{\chi 3}|^2 - |Z_{\chi 4}|^2\right) &&\text{(5.4.2)}\\
&\simeq -\frac{g^2 T_{3i} t_W^2}{8(t_\beta^2 + 1)(\mu^2 - M_1^2)^2}\left(t_\beta^2(\mu^2 - M_1^2) - 2\mu M_1\right)\,,\\
\alpha_{3i} &= -\frac{g^2 m_{qi}}{4 M_W m_h^2}\mathrm{Re}\left[(s_\beta Z_{\chi 4} - c_\beta Z_{\chi 3})(Z_{\chi 2} - t_W Z_{\chi 1})\right]\\
&\simeq -\frac{g^2 m_{qi} t_W^2 t_\beta}{4 m_h^2 (t_\beta^2 + 1)(\mu^2 - M_1^2)}\left(2\mu + t_\beta M_1\right)\,. &&\text{(5.4.3)}
\end{aligned}
$$

These approximations are valid while $M_1 \lesssim |\mu| \ll M_2$ and for large $t_\beta \equiv \tan\beta$. Generically, there is a strong correlation between these two terms, however, our scan of the 11-parameter MSSM reveals a non-negligible region of parameter space in which the SI cross section is suppressed with respect to SD scattering. A more detailed look at the parameter space shows that this region is characterized by small negative values for $\mu < 0$ and $|\mu|/M_1 \gtrsim \mathcal{O}(1)$. Essentially, this behaviour is due to the fact that there are blind spots in the parameter space where the SI cross section vanishes (cf. [167]). Quantitatively, we find a non-negligible region in parameter space where $\sigma_{p,n}^{SI} \lesssim 10^{-46}\mathrm{cm}^2$ and thus beyond the projected sensitivity of XENON1T while a SD cross section $\sigma_n^{SD} \sim 10^{-40}\mathrm{cm}^2$ induces a sufficiently large recoil rate to be detected in future experiments. At the LHC this scenario would be characterized by comparatively light charginos.

Finally, we would like to note that this region of parameter space is typically excluded within the latest CMSSM analyses, because LHC and Higgs mass constraints would require very large scalar soft terms $m_0 \sim 10\,\mathrm{TeV}$ [160]. The reason is the large running of $M_{H_u}^2$ induced by the large trilinear term. Once we relax the CMSSM assumptions and allow the soft Higgs and squark mass terms to vary independently a thermally produced neutralino with an observable SD cross-section remains a quite reasonable possibility even though LHC searches for supersymmetry are constraining this scenario.

5.5. Summary of direct searches

Due to the increasing sensitivity of dark matter searches a proper assessment of the complementarity of different search strategies is becoming more important. In this chapter we considered the impact of direct and indirect detection on the parameter space of dark matter, concentrating on searches for a gamma-ray feature with current and upcoming gamma-ray telescopes, i.e. Fermi-LAT, GAMMA-400 and CTA, and compared them to the existing bounds from XENON100 and the prospects for XENON1T and DARWIN. It turned out that XENON100 is already able to exclude thermal dark matter up to hundreds of GeV depending on the mass splitting, while gamma-ray searches fall short of probing the expected cross section of a thermal relic unless

an astrophysical boost factor increases the gamma-ray flux. Furthermore, existing limits have implications for future gamma-ray searches and we find that given the stringent constraints from XENON100 even future satellite born gamma-ray telescopes with an improved energy resolution, e.g GAMMA-400, cannot hope to observe an IB signal from dark matter coupling to light quarks. However, it appears that XENON1T and CTA are complementary as XENON1T efficiently probes dark matter masses lighter than 1 TeV, while CTA is expected to be chiefly sensitive in the multi TeV regime.

We demonstrated that in view of the stringent upper limits on the dark matter nucleon cross section from direct detection experiments, it is important to consider both SD and SI interactions. Using the latest XENON100 data we derived constraints on the SD cross section and find that these limits exceed the previous best limit on SD-neutron scattering by about one order of magnitude. In order to illustrate the relevance of SD direct detection we demonstrated in two well motivated dark matter models that the scattering rate can be completely dominated by SD interactions and showed that neglecting this bound can lead to a significant overestimation of the allowed parameter space. Furthermore, we commented on the nuclear uncertainties of SD scattering and find that xenon based experiments can be used to derive robust limits on the SD-neutron cross section whereas a reliable interpretation in terms of SD-proton scattering requires a better understanding of nuclear form factors. Finally, prospects for the detection of thermal dark matter with the projected direct detection experiments XENON1T and DARWIN are promising and should not be disregarded.

6. Collider Searches: Probing the Dark Sector

Beside indirect and direct searches, collider experiments are the third main way to probe dark matter. A striking difference between collider searches and the other approaches to dark matter detection is that the LHC probes the interactions of the complete dark sector with the Standard Model and not only the interactions of the dark matter particle.

However, constraining dark matter at the LHC is rather challenging, as the interpretation of collider searches is highly model dependent and requires a good understanding of both theory and experiment. One particularly enticing possibility to address this issue is to use simplified models and classify the expected collider phenomenology while avoiding the constraints present in a full theory. Here, we will focus our attention on the simple scenario of a Majorana dark matter particle coupling to quarks via a scalar mediator we introduced in Sec 3.1. The collider phenomenology of this model is rather different from that of the popular effective operator approach [148, 150, 168], as the production and decay of the scalar mediator η leads to final states with multiple jets and missing energy, which can be searched for rather efficiently at the LHC. Collider aspects of related models have been discussed in [169, 170, 171, 172] (see also [173, 174, 175] for a discussion of leptophilic models).

In this chapter we discuss the collider analysis in detail. In particular, we determine the total production cross section at the LHC and find that apart from the standard QCD production additional processes with dark matter exchange in the t-channel can be relevant in this scenario. This possibility has been discussed previously in [169, 170, 171, 172]. In the following we improve the analysis by performing a dedicated re-interpretation of an ATLAS search including jet matching with up to two additional jets in our Monte Carlo simulation. Recently a similar analysis has been performed for Dirac dark matter [152], however, the phenomenology of the two models is different. Our analysis is based on the experimental limits on events with jets and missing energy reported by the ATLAS collaboration in [12]. We derive upper limits on the Yukawa coupling of our model and analyse the complementarity of the indirect detection signatures discussed in Ch. 4, the bounds from direct detection derived with the methods introduced in Ch. 5 and LHC searches. Finally, we analyse different experimental and theoretical uncertainties which affect the LHC analysis and discuss their impact on the robustness of collider limits.

In the following we will first discuss the various contributions to the production cross section of the scalar η in Sec. 6.1 and comment on the details of our LHC re-interpretation in Sec. 6.2. We present our results and discuss the complementarity in Sec. 6.3 before summarizing our main
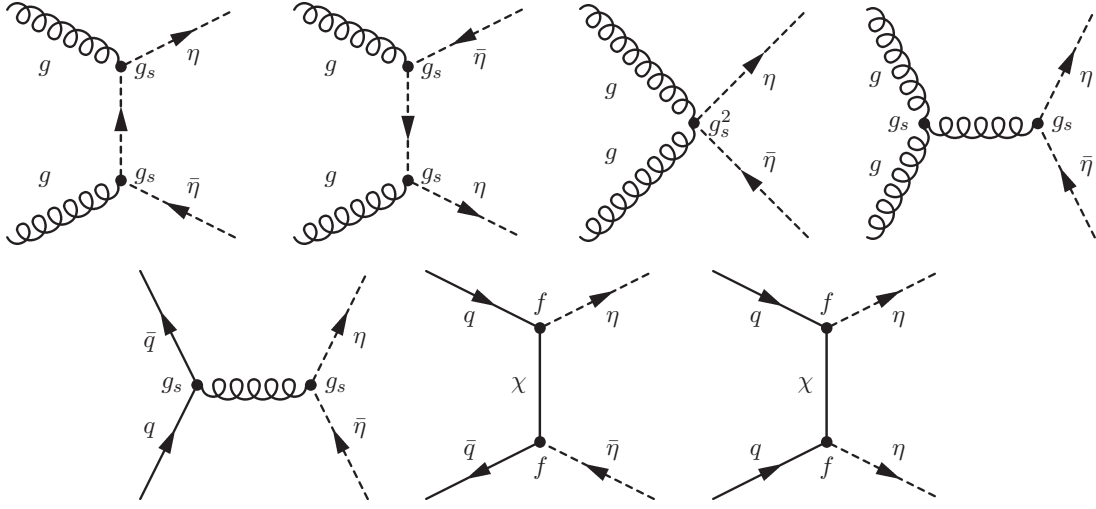
Figure 6.1.: Feynman diagrams contributing to the production of coloured scalar mediators at a hadron collider. This figure was published in [22].

conclusions in Sec. 6.3. Parts of this chapter were published in [22].

6.1. Production at LHC

Probing dark matter at the LHC is a challenge since a good candidate for thermal dark matter can only have interactions of weak strength and thus leaves the detector unobserved. Consequently, the only signature of dark matter in proton proton collisions is the presence of a large amount of missing transverse energy (MET). Recently, searches for mono-jet events with large MET have been employed to constrain dark matter interactions [150, 148]. However, models with additional light degrees of freedom can offer more effective ways to probe the dark sector than mono-jet searches. The most promising signature in the model under scrutiny here is related to the production of pairs of the mediator η. Since η is not stable and decays into a χq pair we expect n-jet events, $n \geq 2$, with large missing energy from $\eta\bar{\eta}$ ($\eta\eta$) production. Such a final state can be searched for very efficiently at the LHC since multi-jet events allow for a better background suppression than mono-jet searches. Furthermore, this channel is particularly interesting since η carries a colour charge and can thus be produced with a large rate at the LHC.

At the LHC the production rate of η receives substantial contributions from three different production modes. First of all, there is the production of $\eta\bar{\eta}$ pairs due to QCD interactions from gg or $q\bar{q}$ initial states, see Fig. 6.1 for the Feynman diagrams contributing to this process. Since this is a gauge interaction, the cross section depends only on the mass of η and neither m_χ nor the Yukawa coupling f are relevant here (cf. Fig. 6.2). Consequently, the importance of the
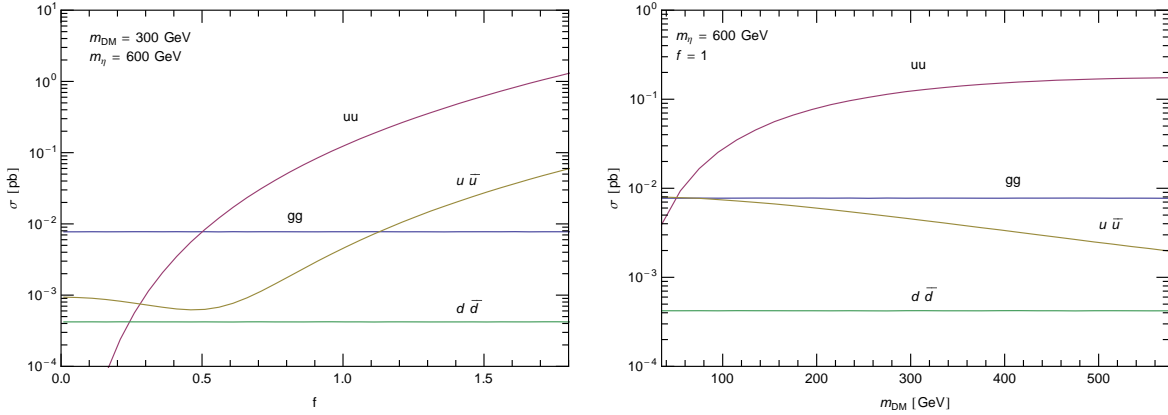
Figure 6.2.: Contributions to the production cross section of the mediator η in proton proton
              collisions with center of mass energy of $8\,\text{TeV}$ as a function of the coupling f for
              $m_\chi = 300\,\text{GeV}$ and $m_\eta = 600\,\text{GeV}$ (left panel) and as a function of the dark matter
              mass for fixed coupling $f = 1$ and $m_\eta = 600\,\text{GeV}$ (right panel). These figures were
              published in [22].

different initial states is set exclusively by their parton luminosities and we find that the largest
contribution is coming from gg with $u\bar{u}$ and $d\bar{d}$ contributing at the $\mathcal{O}(1-10\%)$ level while heavier
quarks are completely negligible. The second process which can be relevant is the production
of $\eta\bar{\eta}$ from the $u\bar{u}$ initial state due to dark matter exchange in the t-channel. Naturally, this
process cannot be considered on its own and the interference with the QCD contribution has
to be taken into account. As apparent from Fig. 6.2 (left panel), the cross section is dominated
by gauge interactions for small values of f, however, for a moderate Yukawa coupling, $f \approx 0.5$,
the t-channel and the QCD diagrams interfere destructively and the cross section receives a
moderate suppression. For larger values of f the t-channel exchange begins to dominate and the
cross section increases with f^4. In addition, there is a third process, which is also caused by dark
matter in the t-channel, the production of a $\eta\eta$ pair. Analogous to squark pair production from
gluino exchange in the MSSM, a chirality flip of the t-channel fermion is required for this process
such that the cross section is proportional to the dark matter mass squared m_χ^2. Consequently,
the cross section $\sigma(\eta\eta)$ vanishes for $m_\chi \to 0$ and increases with increasing m_χ. In a significant
part of the parameter space the cross section $\sigma(\eta\eta)$ actually dominates the production rate since
the parton distribution function of the up quark exceeds that of the anti-up considerably (cf.
[176] for a similar effect related to gluino exchange). For the same reason we do not need to
consider $\bar{u}\bar{u} \to \bar{\eta}\bar{\eta}$ or t-channel processes with charm quarks in the initial state, which could in
principle contribute in our minimal flavour violating set-up with two scalars coupling to up and
charm quarks.

Unfortunately, leading order calculations at the LHC are known to be prone to QCD uncer-
tainties and typically receive substantial corrections from higher order effects. Even though a

full treatment of the NLO corrections is beyond the scope of this work it is still interesting to ask what the plausible range of these corrections is and to derive a first estimate of the impact they have on the interpretation of LHC limits. Useful reference scenarios from which we can get an indication of the size of NLO effects can be found among the more commonly studied supersymmetric models. Consider for instance the pure QCD processes $gg \to \eta\bar{\eta}$ and $dd \to \eta\bar{\eta}$. If all superpartners except for the light squarks are decoupled, as is the case in simplified models of supersymmetry for LHC searches, the SUSY processes are similar to our scenario. Therefore, we can simply use the SUSY cross section, which has been calculated at NLO and next-to-leading-logarithm (NLL), $\sigma_{\text{QCD}}^{\text{NLO+NLL}}$ [177]. We will use the tabulated values available at [178] in our analysis. For squark production with a neutralino (bino) in the t-channel, which is similar to the channels $uu \to \eta\eta$ and $u\bar{u} \to \eta\bar{\eta}$ with t-channel dark matter exchange, there are no NLO corrections available, however, [179] considered the the NLO corrections to squark-squark pair production with the exchange of a gluino in the t-channel and finds $K \approx 1.4$. While this case is not strictly similar to our scenario, namely the gluino is a colour octet and not a colour singlet like our dark matter particle, we expect the size of the corrections in this scenario to be larger than in our case and choose a K factor smaller than this value .

We parametrize the effect of NLO corrections to the total cross section as

$$\sigma = \sigma_{\text{QCD}}^{\text{NLO+NLL}} + K \times (\sigma^{\text{LO}}(f) - \sigma^{\text{LO}}(0)) , \tag{6.1.1}$$

where $\sigma^{\text{LO}}(f)$ denotes the leading-order cross section for a given coupling f, namely $\sigma^{\text{LO}}(0)$ is the LO QCD contribution. We use CalcHEP3.2 [180] to compute the LO cross section and use the CTEQ6 PDF set [115] in our calculation. In order to estimate the impact of QCD corrections, we vary $\sigma_{\text{QCD}}^{\text{NLO+NLL}}$ within the theoretical error given in [177, 178], and the K-factor within the range $0.8 - 1.3$. We would like to stress that these values for the K factors are just estimates of the plausible range and should in principle be derived in a NLO calculation. Furthermore, the calculation of the total cross section at NLO is not even sufficient since a full treatment would require the higher order corrections on the exclusive cross section after cuts, which is clearly beyond the scope of this work. As t-channel processes dominate the production cross section of η in substantial parts of the parameter space this model is significantly different from the simplified SUSY models considered by the experimental searches. We perform a full Monte Carlo simulation of the production and the detector response in order to derive the appropriate limits on the production cross section.

6.2. Re-interpretation of LHC constraints

We use the ATLAS search [12] for two or more jets and missing transverse energy based on $\mathcal{L} = 20.3\,\text{fb}^{-1}$ of data collected at a center of mass energy of $8\,\text{TeV}$, in our analysis of the LHC constraints. The minimal requirements an event need to fulfil in order to be considered in this analysis are missing transverse energy $E_T^{\text{miss}} > 160\,\text{GeV}$, transverse momentum $p_T > 130\,\text{GeV}$

for the leading jet and $p_T > 60\,\text{GeV}$ for subleading jets. The search is further subdivided into signal regions defined by the number of hard jets, with a minimum of two and a maximum of six, and by additional cuts, which allow for further background suppression (see [12] for details). The ATLAS Collaboration has derived the expected Standard Model backgrounds for the different search regions and calibrated the rates against four control regions.

No excess above the background is observed and therefore a 95%CL upper limits S_{95}^{obs} on the number of signal events is reported for each of the search regions. This upper limits S_{95}^{obs} can be translated into the upper limit on the production cross section of a given model by

$$S_{95}^{\text{obs}} = \sigma_{\text{vis}} \times \mathcal{L} = \sigma \times \epsilon \times \mathcal{L}\,, \tag{6.2.1}$$

where $\sigma_{\text{vis}} = \sigma \times \epsilon$ is the visible cross section, and the model dependent efficiency $\epsilon = N_{\text{after cuts}}/N_{\text{generated}}$ is given by the fraction of signal events which pass all the cuts.

It is important to note that, while the observed limits on the signal events are model independent, the interpretation in terms of the excluded cross section relies on the efficiencies which depend on the precise kinematics of the final state and are therefore a model dependent quantity. In our model the production of η is dominated by the $uu \to \eta\eta$ production mode in large parts of the parameter space. As the production in the simplified supersymmetric model considered in [12] is mediated by QCD interactions the efficiencies used in the experimental analysis are not appropriate for a study of our model. A further source of model dependence can be relevant for small mass splitting $m_\eta - m_\chi \lesssim \mathcal{O}(100\,\text{GeV})$. In this regime the jets from η decay are less energetic and additional hard jets from the initial, final or intermediate particles in the diagrams in Fig. 6.1 can become relevant and influence the efficiency considerably.

In order to determine the appropriate efficiencies in our model we perform a dedicated Monte Carlo simulation with MadGraph5 [181] interfaced with the fast detector simulation Delphes (version 3.0.10) [182]. We generate a large number of events with up to two additional partons in the final state and take the double counting of matrix-element level partons and hard jets from hadronization into account by employing the MLM jet matching scheme. The minimum k_t jet measure between partons is taken to be `xqcut`$= m_\eta/4$ and the jet measure cut-off used by Pythia [183] is `QCUT=xqcut`. We cross checked our efficiencies against those presented by the ATLAS Collaboration for a simplified supersymmetric model in [12] and reproduce the cut-flow tables reported in the experimental analysis. In general, the agreement between our results and the official values from ATLAS is rather good; we find the agreement to be typical better than 10% while the largest discrepancies remain $\lesssim 30\%$.

We calculate the efficiencies for all signal regions with $n \leq 4$ jets by generating a large number of events on a two dimensional grid in the $m_\chi, m_\eta/m_\chi$ plane where we set $f = f_{th}(m_\chi, m_\eta/m_\chi)$, the expected coupling for a thermal relic. Based on these efficiencies we compute, using Eq. (6.2.1), the upper limit on the signal cross section. The optimal signal region is selected based on the best expected sensitivity. The efficiencies can be affected by uncertainties introduced by the matching algorithm; in order to estimate the size of these uncertainties we vary

`xqcut` and `QCUT` within a factor of two and find the changes in the efficiencies $\lesssim 30\%$. Furthermore, the uncertainty can also be affected by statistics since only a finite number of events is generated. This effect becomes relevant for small mass differences $m_\eta - m_\chi$ or search regions with $n \geq 3$ jets since in these regions only a relatively small number of events passes all the cuts. In order to minimize this effect we generate up to $N_{generated} \simeq 1.2 \times 10^6$ events and exclude search regions with a statistical uncertainty larger 30%. The size of this uncertainty is visualized by the blue band in Fig. 6.3.

6.3. Results and comparison with indirect and direct searches

In the following we present our results from the re-analysis of the ATLAS search for jets and missing energy [12] and discuss the relative importance of the constraints from direct, indirect and collider searches. We concentrate on two of the minimal scenarios introduced in Sec. 3.1 and present limits for a simple scenario where dark matter couples exclusively to u_R and a scenario with two mass degenerate mediators coupling to u_R and c_R.

It turns out that the observed upper limit on the production cross section depends strongly on the mass splitting $\delta = m_\eta/m_\chi - 1$ (cf. 6.3). For large mass splittings $\delta \gg 1$ the limits are very strong and cross sections as small as ≈ 1fb can be excluded. In this limit the strongest constraints come from search regions with three and four jets and strong cuts, namely B_t and C_t in the notation of [12], as these regions allow for the best background suppression. For smaller values of the mass splittings $\delta = \mathcal{O}(1)$ the efficiencies drop and the best limits can be derived from search regions with looser cuts (B_m and C_m) which have larger statistics than the more restrictive regions. We observe that the limits worsen by several orders of magnitude compared to the limit of large δ. If we consider even smaller mass splittings $\delta \ll 1$, the jets from the decay $\eta \to \chi q$ become soft and additional hard jets emitted from the initial, final or intermediate states are crucial for the determination of the experimental sensitivity. Since hard jets are no longer available from the decay the three and four jet search regions are inefficient in this limit and the most sensitive regions are those with just two jets (A_l and A_m). It should be noted that when we include only one additional parton from the matrix element instead of our default number of two, the constraints weaken in this region, as can be seen from the blue dashed line in Fig. 6.3. For $\delta \ll 1$ we find that the constraints form a plateau at $0.5 - 50$ pb, depending on the mass of the dark matter particles.

In addition to the experimental bounds we show the theoretical expectation for the cross section assuming a thermal production of dark matter (see black lines in Fig. 6.3). The black dashed line depicts the minimal production cross section due to QCD interactions. As can be seen, the new physics contribution from dark matter exchange in the t-channel typically dominates for mass splittings $\delta \gtrsim 0.1$ when we fix $f = f_{th}$ such that the thermal relic abundance is in agreement with the latest observations by the Planck satellite. For $\delta \lesssim 0.1$ coannihilations become relevant for thermal freeze-out and small values for f are favoured. Consequently, the
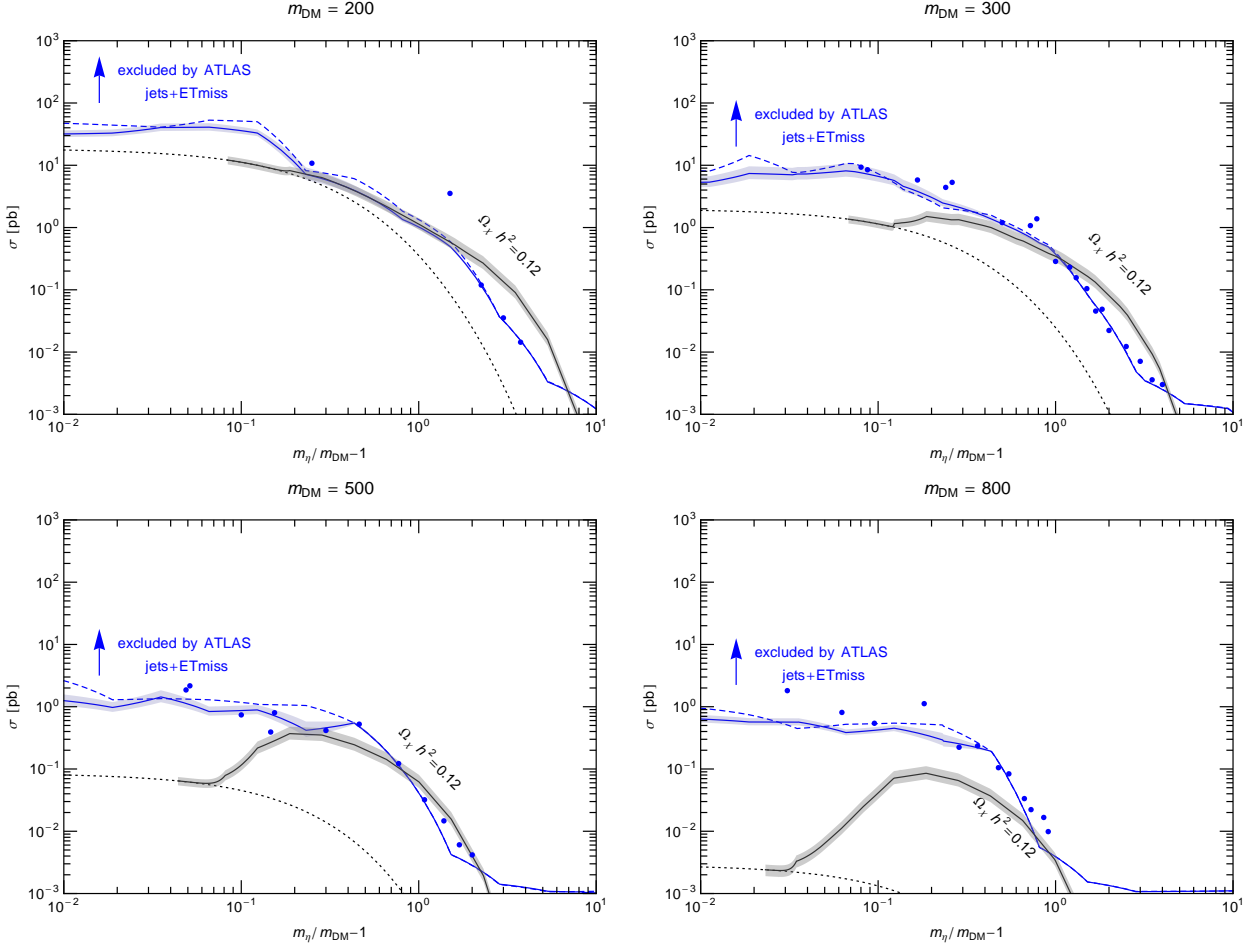
Figure 6.3.: Upper limit on the production cross section from the ATLAS search [12] for jets and missing transverse energy (blue) as a function of the mass splitting between the dark matter and mediator particle. The four panels correspond to $m_\chi = 200, 300, 500, 800\,\text{GeV}$. The black line shows the expected cross section for a thermal WIMP. The black dotted line is the production cross section arising from QCD interactions only (i.e. for $f \to 0$). The blue dashed line corresponds to the limit one would obtain when including only one additional ISR/FSR jet in the matching. For comparison, the blue dots mark the upper limit given by ATLAS [12] for a simplified supersymmetric model containing squarks and neutralino. These figures were published in [22].
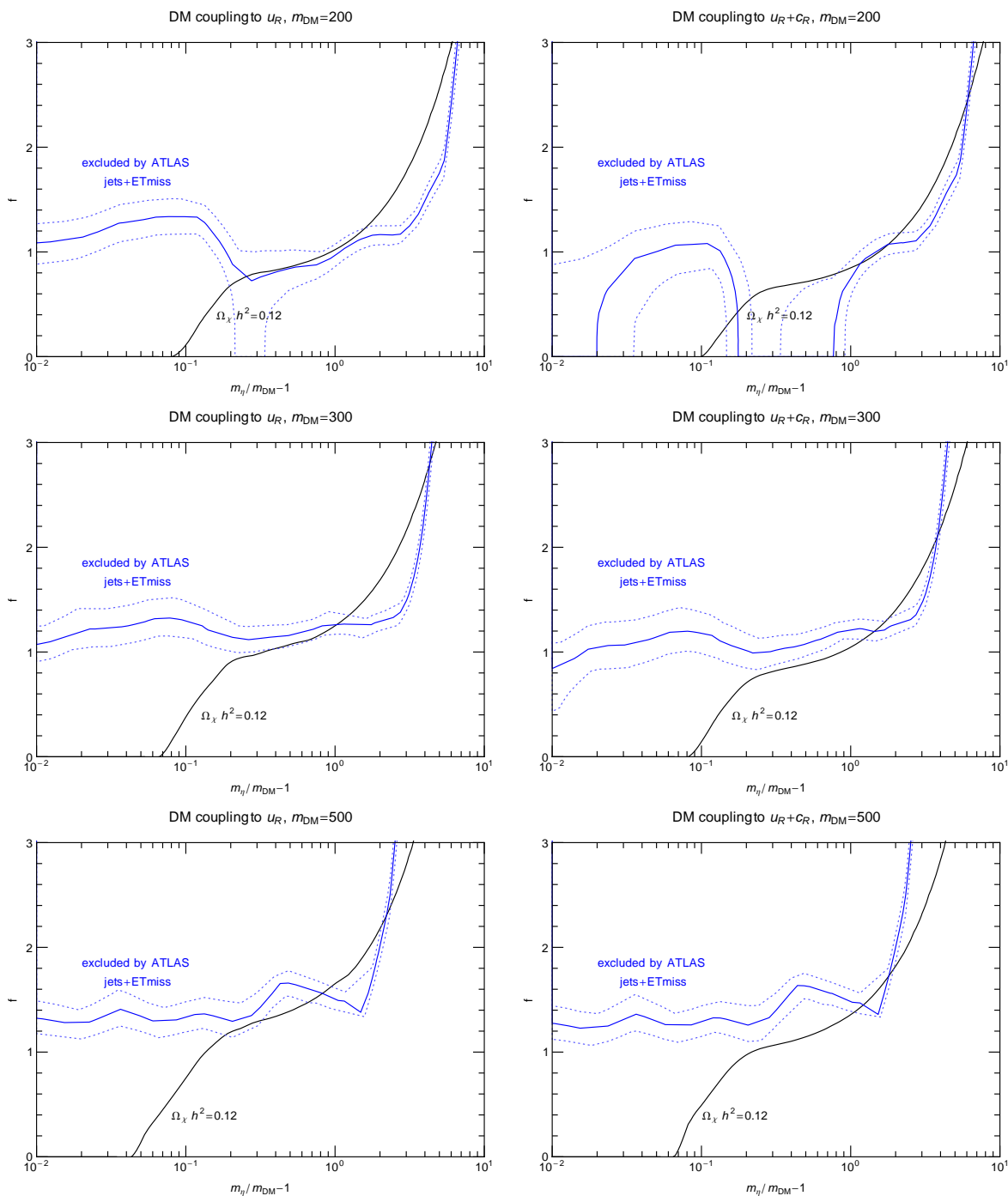
Figure 6.4.: Upper limit on the coupling f inferred from the ATLAS search [12] for jets and missing transverse energy (blue) as a function of the mass splitting between the dark matter and mediator particle, for $m_\chi = 200, 300, 500$ GeV. The left panel corresponds to the case of a single mediator coupling to u_R, and the right to two mass-degenerate mediators coupling to u_R and c_R, respectively. The blue dotted lines indicate the uncertainty (see text for details), and the black line corresponds to a thermally produced WIMP. These figure were published in [22].

cross section of the t-channel process gets suppressed and QCD interactions dominate in this regime. The gray band illustrates the impact of the theoretical uncertainty on the production cross section as estimated in Sec. 6.1.

Furthermore, an interesting possibility is to relax the requirement of a thermal relic and treat the coupling f as a free parameter. In this case the limit on the production cross section can be used to derive an upper limit on the size of f (see Fig. 6.4). The largest allowed values for the couplings f are $\mathcal{O}(1)$ for $\delta \lesssim 2 - 3$ and increase fast beyond this range. The blue dotted lines indicate the maximal combined uncertainty from our estimate of the QCD corrections to the cross section and the statistical uncertainties of the efficiencies. Note that when the QCD production cross section is larger than the excluded cross section the bound on f goes to zero. When this happens the corresponding choice of the dark matter mass m_χ and m_η is excluded irrespectively of the value of f and no contribution to dark matter is allowed.

In the left panel of Fig 6.4 we show the scenario with just one mediating scalar coupling to u_R while the right panel shows the case of two mass degenerate scalars coupling to u_R and c_R. We find that the limits on f are rather similar except for small dark matter masses $m_\chi \lesssim 200$ GeV. In this mass range the QCD cross section can become relevant and, since the pure QCD production rate doubles in the scenario with two scalars, the mass range in which all values of f are excluded gets larger. On the other hand, there is very little impact in the parameter range where the t-channel process dominates as $uu \rightarrow \eta\eta$ remains unchanged and processes with charm quarks are strongly suppressed due to the parton distribution function of the proton. However, there is an additional effect on the thermal coupling which has to be taken into account. If coannihilations can be neglected, the thermal cross section scales like $\sigma v \propto N f^4$ where N is the number of Standard Model fermions χ interacts with. Consequently, the expected thermal coupling changes as $f_{th} \propto N^{-1/4}$. The behaviour in the coannihilation regions is rather complicated and we use results from MicrOMEGAS in all our numerical calculations.

6.3.1. Comparison with direct detection

The upper limits on the value of f can now be translated into constraints on the spin-dependent and spin-independent direct detection cross section. We show the bounds on σ_{SI} and σ_{SD} in Fig. 6.5 and compare them to the experimental upper limits from XENON100 [4, 140] and LUX [5]. As explained in Sec. 5.3, the direct detection cross section is enhanced for mass splittings $\delta \ll 1$, while collider limits get weakened due to the loss of efficiency caused by less energetic jets from η decays. For $\delta = \mathcal{O}(1)$, on the other hand, the collider sensitivity is excellent and the ATLAS limits exceed the bounds from direct detection experiments by orders of magnitude in both SI and SD for dark matter masses in the range $m_\chi = 10^2 - 10^3$ GeV. Furthermore, the LHC limits can even exclude the QCD production of η for $m_\chi \approx 100$ GeV and $\delta = \mathcal{O}(1)$. For these masses the limit on f formally approaches zero which leads to the severe suppression of the inferred direct detection cross sections, as can be seen in the middle row of Fig. 6.5. It should be noted that the impact of collider uncertainties, which is typically small, becomes large
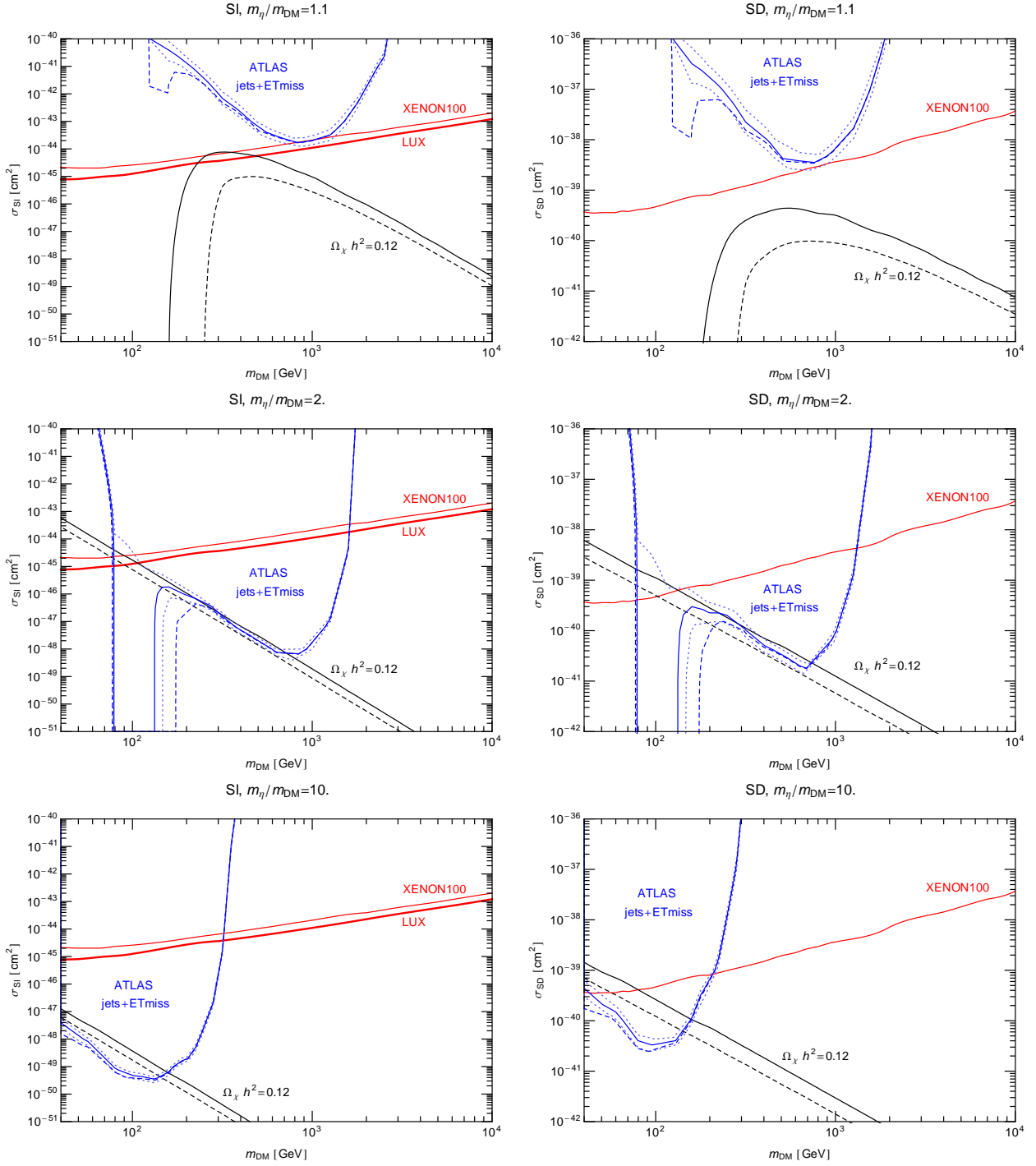
Figure 6.5.: Comparison of constraints inferred from the ATLAS search [12] for jets and missing energy with the spin-independent (-dependent) scattering cross section off protons (neutrons), shown in the left (right) panel. The rows correspond to mass ratios $m_\eta/m_\chi = 1.1, 2, 10$ between the dark matter and mediator mass. Solid lines correspond to the case where dark matter couples to u_R, and dashed where it also couples to c_R. The blue dotted lines indicate the uncertainty of the collider constraint for the case of u_R-coupling (see text for details). These figures were published in [22].

in this region and can change the limits by many orders of magnitude (see the blue dotted lines in Fig. 6.5). In the case of large mass splittings $\delta \gg 1$ the collider bounds still remain excellent for low m_χ, but weaken fast with increasing m_χ and δ since mediators with $m_\eta \gtrsim 2$ TeV cannot be produced efficiently at the LHC. For comparison we also show the LHC limit for the u_R/c_R model as a blue dashed line. The black (dashed) line corresponds to the cross section expected for a dark matter particle χ which has the correct relic density due to interactions with a u_R (u_R/c_R) mediator.

6.3.2. Comparison with indirect detection

The most interesting signature of this model in indirect detection experiments is the presence of a pronounced high energy feature in the gamma-ray spectrum. As explained in more detail in Ch. 4 the spectral feature is dominated by internal bremsstrahlung for $\delta \leq \mathcal{O}(1)$ while the contribution from $\chi\chi \to \gamma\gamma$ becomes more important for $\delta \geq \mathcal{O}(1)$. In Fig. 6.6 we show the constraint on the combined annihilation cross section into hard gamma-rays, $\sigma v_{q\bar{q}\gamma} + 2\sigma v_{\gamma\gamma}$, derived from the ATLAS limit on f and compare it with the bounds from direct detection [21] and the experimental limits from gamma-ray observations of the central galactic halo by Fermi-LAT [18] and H.E.S.S. [8]. As can be seen, the limits from direct detection dominate over the upper limits from the LHC search for small values of δ. However, the LHC bounds are much stronger for $\delta = \mathcal{O}(1)$ and constrain the possibility of observing a spectral feature with present and upcoming instruments strongly for $m_\chi \lesssim 10^3$ GeV. Nevertheless, gamma-ray searches remain the most promising detection techniques for dark matter candidates with masses in the multi-TeV range.

6.3.3. Constraints on thermal relics

Finally, it is interesting to analyse the impact of direct, indirect and collider searches on the allowed parameter space for thermal dark matter. If we demand that the relic density predicted in our scenario matches the observed relic density, we can fix one of our free parameters in terms of the other. To be more specific, in the following we choose m_χ and δ to be our free parameters, fix $f = f_{th}(m_\chi, m_\eta)$ and show the constraints from different experiments in this plane in Fig. 6.7. As can be seen, the ATLAS exclusion region reaches up to dark matter masses $m_\chi \lesssim 10^3$ GeV for $\delta = 1$. For larger or smaller values of δ much lighter dark matter is allowed. The reason for this behaviour is twofold. On the one hand, for $\delta \gtrsim 1$ the mass of the scalar mediator m_η gets heavier, such that η cannot be produced efficiently at the LHC. On the other hand, for $\delta \lesssim 1$ the experimental sensitivity is reduced while at the same time coannihilations become more important which prefer small values for f_{th} such that the production cross section decreases. In order to determine the uncertainty of the exclusion region we vary both the experimental upper limit and the theoretical production cross section within their uncertainties and obtain the region bound by the green dashed line. The excluded region is rather sensitive to these

$m_\eta/m_{\mathrm{DM}}=1.1$
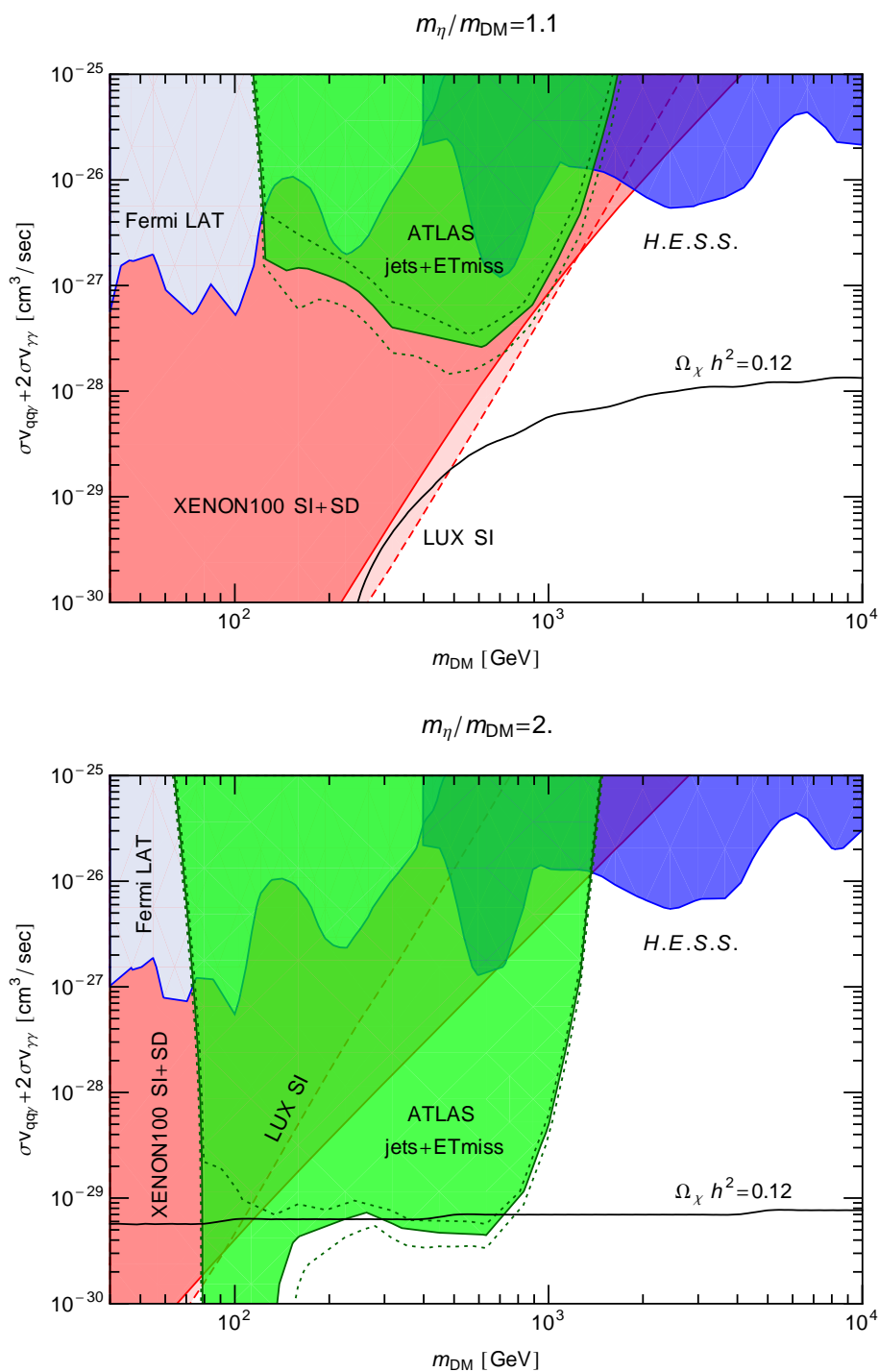

$m_\eta/m_{\mathrm{DM}}=2.$

Figure 6.6.: Comparison of constraints on the annihilation cross section obtained from searches for spectral features by the Fermi-LAT [18] and H.E.S.S. [8] (*cf.* [21]), with constraints inferred from collider searches for jets and missing energy by ATLAS [12], as well as direct detection limits from XENON100 [4] and LUX [5]. The black line corresponds to a thermal WIMP, and the dotted lines indicate the uncertainty of the collider constraint, as discussed before. Note that the results for u_R/c_R mediator are very similar, and are therefore not shown. These figures were published in [22].
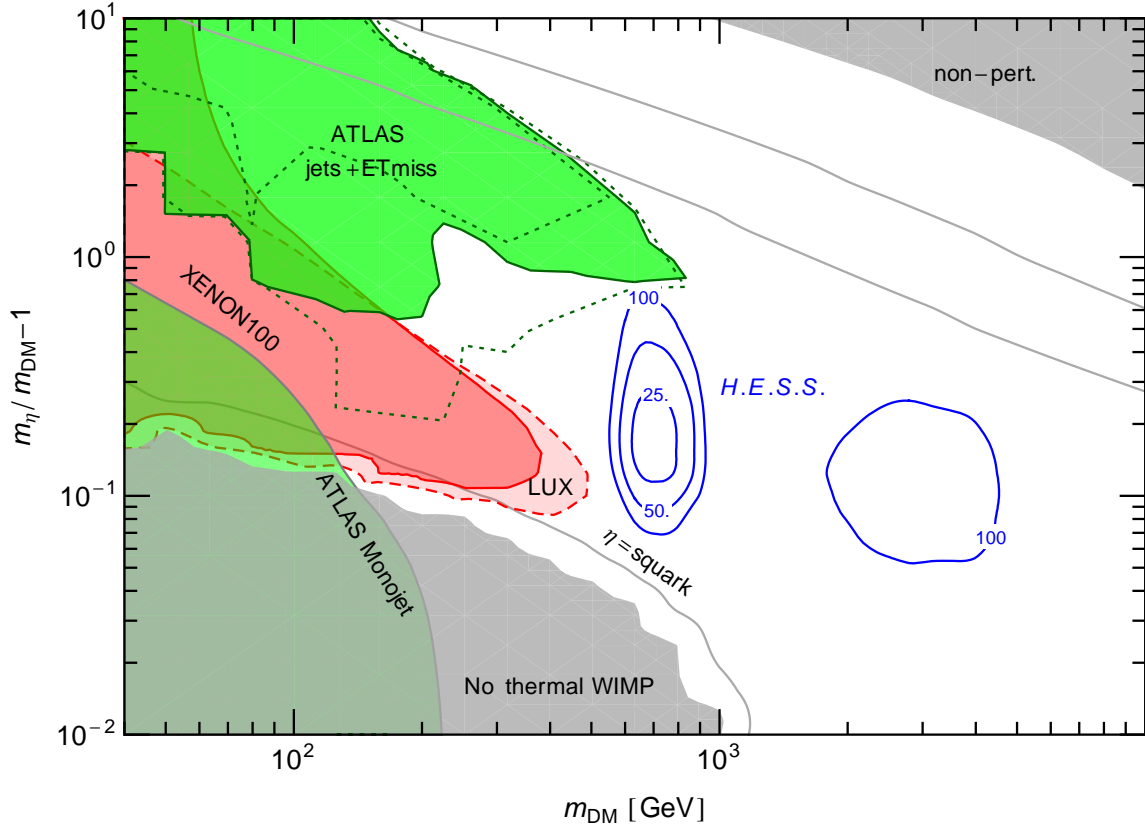
Figure 6.7.: Constraints on thermally produced WIMP dark matter with a coloured mediator particle η. The green region is excluded at 95%CL by the ATLAS search [12] for jets and missing transverse energy. For comparison, the red shaded area is excluded by direct searches. The blue lines indicate the regions excluded by the search for an internal bremsstrahlung feature in the gamma-ray spectrum from the central galactic halo measured by H.E.S.S. [8], assuming a boost factor $25, 50$ or 100, respectively [21]. Within the grey shaded region in the lower left corner, thermal production cannot make up for the whole dark matter abundance due to efficient coannihilations. Within the upper right corner, non-perturbatively large values of $f \gtrsim 10$ would be required. Below the upper(lower) gray line $\Gamma_\eta / m_\eta < 0.5(0.1)$. The gray dashed line indicates the masses for which the coupling of the mediator equals the one of a squark. This figure was published in [22].

uncertainties, since both the excluded cross section and the expected thermal production cross section behave very similar (see also Fig. 6.3). In contrast to the collider search, direct detection mainly probes the region with small mass splitting δ due to the enhancement of the direct detection cross section. The constraints from indirect detection are less stringent and do not exclude the thermal cross section for any choice of m_χ and δ within the ranges considered here, however, H.E.S.S. can become sensitive to the flux from dark matter annihilations in the multi-TeV region if astrophysical boost factors increase the annihilation rate by a factor of $25 - 100$. Finally, we also show for comparison the region of parameter space excluded by a monojet search at the LHC [184], which can be used to probe very mass degenerate scenarios.

6.4. Summary of collider limits

The LHC offers excellent opportunities to probe dark matter provided the mass m_χ is accessible in proton proton collisions at a center of mass energy of 7, 8 or 14 TeV. However, the interpretation of collider searches is very model dependent and in general the definition of an efficient search region requires an understanding of the expected signal. A promising approach to tackle these issues without narrowing the scope of LHC searches by overly specific model conditions is the use of simplified models which offer an effective framework for the description of dark matter phenomenology in a large class of models. Here, we discussed the implications of a simplified model with a Majorana fermion as the dark matter particle χ that interacts with light quarks via a scalar mediator η. An excellent experimental signature in this scenario, which is due to the production and subsequent decay of the mediator η, are events with two or more jets and missing transverse energy.

We calculated the production cross section of η and include in our derivation both the contribution from strong interactions and the production from t-channel exchange of the dark matter particle χ. It is interesting to note that the t-channel process can be relevant and even dominates the total production rate in large regions of parameter space which are consistent with the correct relic abundance from thermal freeze-out. To be more specific, we would like to stress the relevance of the process $uu \to \eta\eta$ as this production channel receives a considerable enhancement compared to other production modes due to the large parton distribution function of the up quark. For large values of the dark matter mass and a mass difference between the dark matter and the scalar mediator of the order of the dark matter mass the cross section of this process can exceed the cross section of the competing QCD processes by more than two orders of magnitude.

We analysed the results of an ATLAS search for jets and missing energy using $\mathcal{L} = 20.3$ fb^{-1} collected at 8 TeV [12] and determined limits on the parameter space of our model. In order to allow a reliable re-interpretation of the ATLAS search we have carefully derived the appropriate efficiencies for our model taking into account jet matching with two additional jets.

The LHC places strong bounds on the allowed parameter space of the model, in particular we

find that thermal dark matter is ruled out in significant regions of parameter space. Furthermore, we investigated the complementarity of collider searches with other experiments. We find that the limits from the LHC and from direct detection are comparable for small mass differences, however, the LHC surpasses direct detection considerably for mass splittings of the order of the dark matter mass and excludes cross sections of $\sigma_{SI} \sim 10^{-45} - 10^{-48}$ for 200 GeV $\lesssim m_\chi \lesssim 1$ TeV and $m_\chi \lesssim 2m_\eta$. The impressive power of collider constraints relative to direct detection can be understood from the fact that the operators mediating spin-independent interactions between the dark matter and the nucleus are suppressed for Majorana fermions with chiral interactions while the production rate at the LHC is enhanced by the $uu \to \eta\eta$ process.

In addition, we find constraints from gamma-rays to be complimentary to both direct detection and collider searches. However, for dark matter masses $m_\chi \lesssim 1$ TeV direct detection and LHC bounds constrain the possibility of observing a signal in the gamma-ray sky severely. As these bounds on the annihilation cross section in the galaxy are derived from collider observables they are not subject to astrophysical uncertainties and are only affected by the uncertainties related to the experimental efficiency and the production cross section which are typically $\lesssim 50\%$. Finally, we also considered an extension of our model motivated by the paradigm of minimal flavour violation in which we include two scalar mediators, one coupling to u_R and the other to c_R, and find that our main conclusions remain essentially unaffected.

7. Conclusion

Determining the nature and the origin of dark matter remains one of the major questions particle physics needs to solve today. In order to understand the microscopic physics which governs the interactions of dark matter with ordinary matter we need to study the phenomenology of dark matter models and exploit the available experimental data efficiently. In this work, we analysed the impact of recent experimental efforts on the allowed parameters of dark matter and discussed the complementarity of different detection strategies.

One of the challenges that must be confronted in indirect dark matter detection is the proper discrimination between a probably feeble signal and the astrophysical background. In particular, gamma-ray features, which can be generated for example by a gamma-ray line or internal bremsstrahlung, are very promising in this regard since this kind of signature cannot be attributed to astrophysical processes easily. Here, we performed for the first time a dedicated search for an IB-signature using the first 43 month of Fermi-LAT data. As an appropriate target region is crucial for an efficient search for spectral features, we proposed a novel technique for the determination of the optimal search region. The limits obtained from the analysis of this region exceed previous constraints from the observation of dwarf galaxies; however, the thermal cross section remains out of reach of gamma-ray searches. Furthermore, we found a weak indication for a gamma-ray excess at 130 GeV, which could be explained by dark matter annihilations. Quantitatively, an internal bremsstrahlung signal from annihilations of a dark matter particle with a mass of approximately 150 GeV and a cross section of around $6 \times 10^{-27} \mathrm{cm}^3 \mathrm{s}^{-1}$ is preferred at 3.1σ once the look-elsewhere effect is taken into account.

With the great wealth of experimental data, which has become available recently, it is now possible to analyse the complementarity of different observation strategies. One intriguing question in this context is the relative strength of direct and indirect detection in the search for mass-degenerate models. On the one hand, we find direct searches to be very powerful in constraining models with interactions with the light quarks and note that the limits from the XENON100 experiment even preclude the observation of a gamma-ray feature from internal bremsstrahlung with the next generation of gamma-ray telescopes for dark matter masses lighter than 1 TeV. On the other hand, future direct detection experiments, e.g. XENON1T, are complementary to projected large scale Cherenkov telescopes, e.g. CTA, which are able to probe the multi-TeV mass range to which the sensitivity of direct detection experiments is limited.

A different opportunity, which is becoming more relevant due to the unprecedented sensitivity of direct detection experiments, is the interpretation of the data in terms of different interactions.

In particular, it has been noted that xenon based experiments possess an excellent sensitivity to SD interactions and can be used to derive limits on the SD cross section. In this thesis, we used the latest data published by the XENON100 collaboration and derived upper limits on the SD scattering cross section. Furthermore, we discussed the impact of nuclear uncertainties on the constraints. Unfortunately, the SD-proton cross section is strongly affected by nuclear uncertainties and we find that a better understanding of nuclear form factors is imperative in order to derive useful limits. However, this issue does not arise in SD-neutron scattering and we obtained stringent upper limits. Furthermore, we discussed the impact of SD searches on dark matter in two exemplary models and demonstrated that the constraints on SD interactions are able to exclude parts of the parameter space of thermal dark matter, which are compatible with SI limits. In particular, the next generations of direct detection experiments, namely XENON1T and DARWIN, can be expected to cut into the parameter space of thermal dark matter.

Finally, we commented on the relevance of the LHC for dark matter detection. In this context it is worth noting that collider experiments are fundamentally different from other searches for dark matter, as they are not only able to detect dark matter but rather probe the entire dark sector. Therefore, the most promising signatures of dark matter at the LHC are not necessarily related to the direct production of dark matter particles since other states of the dark sector can be produced as well. We demonstrated the importance of such a search in our simplified model for dark matter interacting with the light quarks and showed that searches for the production of the scalar mediator can impose stringent constraints on the parameter space. We find that for dark matter masses lighter than 1 TeV, and for a mass splitting of the order of the dark matter mass, collider searches are very competitive and exclude direct detection cross sections in the range $10^{-45} - 10^{-48} \text{cm}^2$. Furthermore, the LHC is able to rule out parts of the parameter space of thermal dark matter and can, in some mass ranges, even exclude subleading contributions to the dark matter abundance.

All considered, it is fair to say that dark matter is under siege today. Multiple experiments employing completely different detection strategies are beginning to cut into the expected parameter space and provide independent constraints on the properties of dark matter. Using a simplified model we have been able to analyse the non-trivial correlations between direct, indirect and collider searches. We find them to be complementary and probe the parameter space in different directions. The results obtained with this simplified model are promising and such an approach could turn out to be very useful. Last but not least, the prospects for the next generation of experiments are encouraging and we can expect significant progress in the near future.

A. Flavour constraints [1]

The interaction term of the dark matter particle and the coloured scalars with the right-handed quarks in general violates the $SU(3)_{u_R}$ flavour symmetry. Therefore, it is necessary to check whether the stringent constraints arising from flavour physics are satisfied. In this Appendix we discuss how two well-known possibilities to suppress flavour-changing neutral currents, namely degeneracy or alignment, can be realized within the toy-model considered in this work.

Consider first the possibility of a single coloured scalar η, but allowing for arbitrary couplings f_i to all right-handed quarks,

$$\mathcal{L} = -f_i \bar{u}_{Ri} \chi \eta \tag{A.0.1}$$

where $i = 1, 2, 3$ corresponds to u, c, t. In this case the box diagram shown in fig. A.1 gives a contribution to $D - \bar{D}$ mixing, which is strongly constrained by the measured value of the D-meson mass splitting Δm_D (note that there is no contribution to CP violation in presence of a single species η, such that constraints from ϵ_D do not apply). The box diagram gives a contribution to the operator

$$\mathcal{L} = \frac{\tilde{z}}{m_\eta^2} \bar{u}_R^\alpha \gamma^\mu c_R^\alpha \, \bar{u}_R^\beta \gamma_\mu c_R^\beta \tag{A.0.2}$$

given by

$$\tilde{z} = -\frac{f_1^2 f_2^2}{96\pi^2} g_\chi(m_\chi^2/m_\eta^2) \tag{A.0.3}$$

where $g_\chi(x) = 24x f_6(x) + 12\tilde{f}_6(x)$ (with $g_\chi(1) = 4/5$). The functions $f_6(x)$ and $\tilde{f}_6(x)$ are given e.g. in [185]. On the other hand, the experimental constraint inferred from measurements of Δm_D is $|\tilde{z}| \lesssim 5.7 \cdot 10^{-7} (m_\eta/\text{TeV})^2$ [185]. For $m_\eta \simeq m_\chi$, this translates into an upper bound

$$|f_2/f_1| \lesssim 0.026 \times (f_1)^{-2} \times \frac{m_\eta}{\text{TeV}} \; . \tag{A.0.4}$$

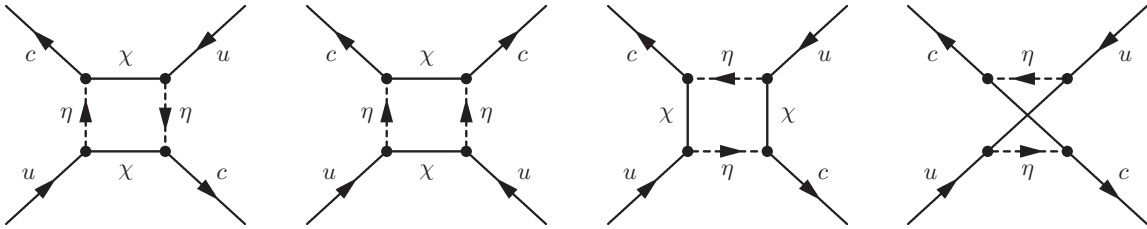[1]This appendix has been published in [22].

Figure A.1.: Box diagrams giving rise to a non-standard contribution to $D - \bar{D}$ mixing.

Since thermal production requires typically $f_1 \sim \mathcal{O}(1)$, this means that η has to couple nearly exclusively to the up-quark, with very suppressed coupling to charm (or vice-versa). A possible exception are regions in parameter space with strong coannihilation for which $f_1 \ll 1$. For a generic $f_1 \sim \mathcal{O}(1)$, the flavour-vector f_i should be aligned with the mass eigenbasis of the quarks. This can be realized e.g. in the presence of a $U(1)$ flavour symmetry under which $u_{R,L}$ and η transform with equal charge, while all other states are uncharged. This symmetry is then broken only by the CKM mixing in the left-handed quark sector, and thus this breaking should lead to a misalignment suppressed by the quark masses as well as CKM mixing angles. More precisely, one may consider a situation where $f_i \propto (1,0,0)$ at some high scale M. Due to renormalization group running, the quark mass matrices $M_u(\mu)$ and $M_d(\mu)$ are scale-dependent. This leads to a running of the diagonalization matrices $M_u^{diag}(\mu) = V_u^L(\mu) M_u(\mu) V_u^R(\mu)^\dagger$, with a similar expression for the down-type quarks. The left-handed rotations lead to the well-known running of the CKM matrix $V_{CKM}(\mu) = V_u^L(\mu) V_d^L(\mu)^\dagger$, while the right-handed rotations are unobservable in the Standard Model [186]. However, in the present case they lead to a flavour-dependent running of the dark matter couplings,

$$f_i(\mu) = V_u^R(\mu)_{ij} f_j(M) \,, \tag{A.0.5}$$

where we neglect flavour-insensitive contributions to the running and assume that $V_u^R(M)_{ij} = \delta_{ij}$. Using the one-loop RGEs for the quark mass matrices from [187], one finds for the off-diagonal entry corresponding to $i = u$ and $j = c$

$$\frac{d}{d\ln\mu} V_u^R(\mu)_{uc}^\dagger = -\frac{3}{16\pi^2 v_{EW}^2} \frac{m_u m_c}{m_u^2 - m_c^2} \left(V_{ud} V_{cd}^* m_d^2 + V_{us} V_{cs}^* m_s^2 + V_{ub} V_{cb}^* m_b^2 \right) \tag{A.0.6}$$

where V_{ud} etc. denotes the CKM matrix elements. Thus, even for perfect alignment $f_i(M) = (f_1, 0, 0)$ at the high scale, the coupling to the second generation induced by the running is approximately

$$|f_2/f_1| \simeq |V_u^R(\mu)_{uc}| \sim \frac{3}{16\pi^2} \frac{m_u}{m_c} \frac{|V_{us} V_{cs}^* m_s^2 + V_{ub} V_{cb}^* m_b^2|}{v_{EW}^2} \ln\frac{M}{\mu} \sim 10^{-10} \tag{A.0.7}$$

which is safely below the upper bound required from $D - \bar{D}$ mixing.

Alternatively, one may consider a situation where three additional scalars η_i are introduced, which are taken to transform under the $SU(3)_{u_R}$ flavour symmetry. Then the allowed coupling is of the form

$$\mathcal{L} = -f \sum_i \bar{u}_{Ri} \chi \eta_i \tag{A.0.8}$$

and the η_i are all mass-degenerate. One may consider a breaking of the symmetry in the scalar mass matrix, which induces non-degenerate mass eigenvalues of the η_i, and singles out a preferred basis, namely the mass eigenbasis (similar to the right-handed squarks in the MSSM). After rotating into this basis (as well as the mass basis for the quarks) the interaction term has the generic form

$$\mathcal{L} = -f K_{ij} \sum_i \bar{u}_{Ri} \chi \eta_j \tag{A.0.9}$$

where K is an unitary matrix, which can have large off-diagonal entries. The resulting contribution to the box diagram will be proportional to [34]

$$\sum_{\alpha,\beta} K_{1\alpha} K_{2\alpha}^* K_{1\beta} K_{2\beta}^* F(m_{\eta_\alpha}, m_{\eta_\beta}) \qquad (A.0.10)$$

where F is a function of the masses. In the limit of degenerate masses this expression goes to zero by virtue of the unitarity condition $(KK^\dagger)_{12} = 0$. Lets assume for concreteness that the mixing with the third generation is negligible, similar as in the CKM matrix. In this case the box diagram gives a contribution

$$\tilde{z} = -\frac{f^4}{384\pi^2} g_\chi(m_\chi^2/m_\eta^2) \times \delta^2 \qquad (A.0.11)$$

with $\delta = K_{21}K_{11}(m_{\eta_1}^2 - m_{\eta_2}^2)/m_\eta^2$ and $m_\eta = (m_{\eta_1} + m_{\eta_2})/2$. Thus, the strong requirement of precise alignment $f_2/f_1 = K_{21}/K_{11}$ found above can be considerably relaxed provided the masses are quasi-degenerate. For order one mixing, the upper bound on $\tilde{z}$ required from $D - \bar{D}$ mixing then translates into an upper bound on the mass splitting

$$\frac{|m_{\eta_1} - m_{\eta_2}|}{m_{\eta_1} + m_{\eta_2}} \lesssim 0.026 \times (f_1)^{-2} \times \frac{m_\eta}{\text{TeV}} \ . \qquad (A.0.12)$$

Thus, in both cases discussed above, the flavour constraints can be fulfilled in presence of an (approximate) flavour symmetry.

B. Three-body annihilation cross sections [1]

B.1. $SU(2)_L$ singlet dark matter

The differential cross-sections for the two-to-three dark matter annihilation processes $\chi\chi \to V f\bar{f}$ in the limit $v, m_f \to 0$, for the case of $SU(2)_L$-singlet Majorana dark matter χ coupling to the SM fermions f via a mediating scalar η_f are given by

$$\frac{vd\sigma(\chi\chi \to \gamma f\bar{f})}{dE_\gamma dE_f} = \frac{C_{\gamma f\bar{f}}\alpha_{em}f^4(1-x)[x^2 - 2x(1-y) + 2(1-y)^2]}{8\pi^2 m_{\mathrm{DM}}^4(1-2y-\mu_f)^2(3-2x-2y+\mu_f)^2} \tag{B.1.1}$$

$$\frac{vd\sigma(\chi\chi \to Z f\bar{f})}{dE_Z dE_f} = \frac{C_{Zf\bar{f}}\alpha_{em}f^4}{8\pi^2 m_{\mathrm{DM}}^4(1-2y-\mu_f)^2(3-2x-2y+\mu_f)^2} ,$$

$$\times \left\{ (1-x)[x^2 - 2x(1-y) + 2(1-y)^2] \right.$$

$$\left. + x_0^2[x^2 + 2y^2 + 2xy - 4y]/4 - x_0^4/8 \right\} , \tag{B.1.2}$$

$$\frac{vd\sigma(\chi\chi \to W f\bar{f}')}{dE_W dE_f} = \frac{C_{Wf\bar{f}'}\alpha_{em}f^4}{8\pi^2 m_{\mathrm{DM}}^4(1-2y-\mu_f)^2(3-2x-2y+\mu_{f'})^2}$$

$$\times \left\{ (1-x)[x^2 - 2x(1-y) + 2(1-y)^2 + 2(2-x-2y)\Delta\mu] \right.$$

$$+ x_0^2[x^2 + 2y^2 + 2xy - 4y + 2(2-x-2y)\Delta\mu + \Delta\mu^2]/4 - x_0^4/8$$

$$\left. + \Delta\mu^2[(1-2x)/2 - 2(1-y)(1-x-y)/x_0^2] \right\} , \tag{B.1.3}$$

$$\frac{vd\sigma(\chi\chi \to g f\bar{f})}{dE_\gamma dE_f} = \frac{C_{gf\bar{f}}\alpha_s(m_{\mathrm{DM}})f^4(1-x)[x^2 - 2x(1-y) + 2(1-y)^2]}{8\pi^2 m_{\mathrm{DM}}^4(1-2y-\mu_f)^2(3-2x-2y+\mu_f)^2} . \tag{B.1.4}$$

Here, $x = E_V/m_{\mathrm{DM}}$ for $V = \gamma, W, Z, g$, $y = E_f/m_{\mathrm{DM}}$, $x_0 = M_V/m_{\mathrm{DM}}$, $\mu_f = m_{\eta_f}^2/m_{\mathrm{DM}}^2$, $\mu_{f'} = m_{\eta_{f'}}^2/m_{\mathrm{DM}}^2$, and $\Delta\mu = (\mu_{f'} - \mu_f)/2$. The pre-factors are given by the following expressions

	$C_{\gamma f\bar{f}}$	$C_{Zf\bar{f}}$	$C_{Wf\bar{f}'}$	$C_{gq\bar{q}}$
$\chi\chi \to V f_R \bar{f}_R$	$q_f^2 N_c$	$q_f^2 N_c \tan^2(\theta_W)$	$-$	$N_c C_F$
$\chi\chi \to V f_L \bar{f}_L$	$q_f^2 N_c$	$\frac{(t_{3f} - q_f \sin^2(\theta_W))^2}{\sin^2(\theta_W)\cos^2(\theta_W)} N_c$	$\frac{N_c}{2\sin^2(\theta_W)}$	$N_c C_F$

where q_f and t_{3f} are the electric charge and the weak isospin, respectively, with $q_e = -1$ and $t_{3e} = -1/2$. For quarks, one has $N_c = 3$, and $C_F = (N_c^2 - 1)/(2N_c) = 4/3$. The spectra of the vector bosons can be obtained by integrating the differential cross-section over the fermion energy, with integration limits given by $E_f^{min/max} = m_{\mathrm{DM}} - (E_V \pm \sqrt{E_V^2 - M_V^2})/2$. The total

---

[1]This Appendix has been published in [17].

cross-section can be obtained by integrating over the remaining energy with limits $E_V^{min} = M_V$ and $E_V^{max} = m_{DM} + M_V^2/(4m_{DM})$. The relevant Feynman diagrams are shown in part (a) and (b) of Fig. B.1 for the exemplary case $\chi\chi \to Ze\bar{e}$.

For comparison, we also quote the leading contribution to the two-to-two cross section for $v \to 0$, in the limit $m_f = 0$,

$$\sigma v(\chi\chi \to f\bar{f}) = \frac{N_c f^4 v^2}{48\pi m_{DM}^2} \frac{1 + \mu_f^2}{(1 + \mu_f)^4} \ , \tag{B.1.5}$$

where v is the relative velocity.

B.2. $SU(2)_L$ doublet dark matter

Here, we report the $2 \to 3$ cross sections for the case of $SU(2)_L$-doublet Majorana dark matter χ that arise from a coupling to the SM fermions f via a mediating scalar η_f. There can be additional contributions due to $2 \to 2$ annihilations into WW or ZZ, with a subsequent decay of one of the gauge bosons. We do not include them here for simplicity. Their size depends on the ratio g/f of gauge interactions and the interactions with the scalar η_f.

The main difference compared to the case of $SU(2)_L$ singlet dark matter are additional contributions from initial state radiation. For annihilation into $\gamma f\bar{f}$ or $gf\bar{f}$, there are no such contributions because the dark matter is electrically neutral and uncoloured. Therefore, the cross-section is identical to the one from above. The cross-section for the annihilation to $Zf\bar{f}$ is given by a sum of ten diagrams: four with initial and final state radiation, respectively, and two where the Z is emitted from the mediating particle η. The Feynman diagrams for the case $\chi\chi \to Ze\bar{e}$ are shown in Fig. B.1. For the cross-section, we find in the limit $m_f, v \to 0$

$$\begin{aligned}
\frac{vd\sigma(\chi\chi \to Zf\bar{f})}{dE_Z dE_f} &= \frac{N_c \alpha_{em} f^4}{2\pi^2 \sin^2(2\theta_W) m_{DM}^4 (2x - x_0^2)^2 (1 - 2y - \mu_f)^2 (3 - 2x - 2y + \mu_f)^2} \\
&\quad \times \left\{ (1 + x_0^2/4 - x)[x^2 - 2x(1-y) + 2(1-y)^2 - x_0^2/2]C_f(x)^2 \right. \\
&\quad + x_0^2(1 - y - x/2)^2 \left[(1 + x_0^2/4 - x)(4C_f(x) + x_0^2) \right. \\
&\quad \left. \left. - x_0^2/2 - 2(1-y)(1-x-y) \right] \right\} \ ,
\end{aligned} \tag{B.2.1}$$

where $C_f(x) \equiv 1 + \mu_f + (x - x_0^2/2)(g_A^f \pm g_V^f) - x_0^2/2$, and $g_V^f = t_{3f} - 2q_f \sin^2(\theta_W)$ and $g_A^f = t_{3f}$ are the couplings to the Z boson. The plus and minus sign applies to annihilation into left-handed or right-handed fermions, respectively. For the annihilation into $Zf_L\bar{f}_L$ the corresponding mediating particle η_f has to have the SM gauge quantum numbers of f_R, and vice versa.
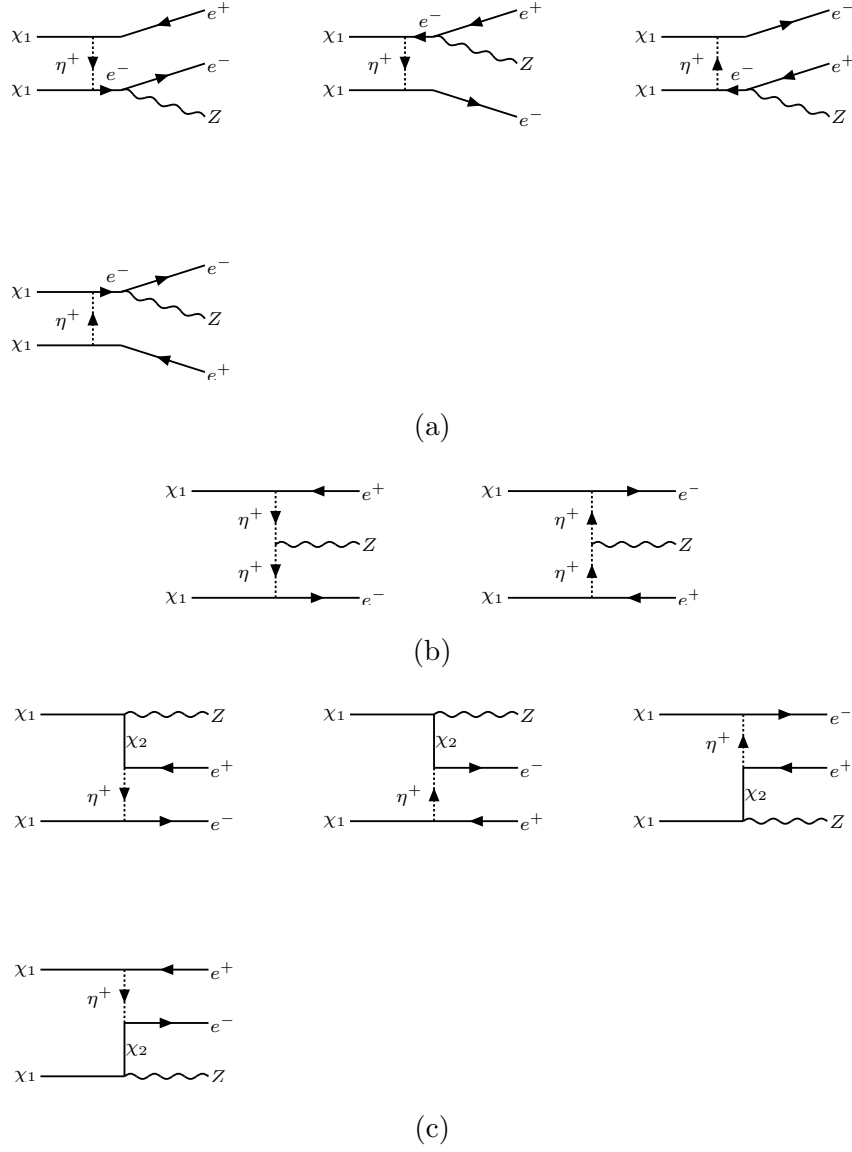
Figure B.1.: Feynman diagrams contributing to the annihilation channel $\chi\chi \to Ze\bar{e}$. For a singlet dark matter particle χ the diagrams corresponding to final state radiation (a) and virtual internal bremsstrahlung (b) contribute. Note that only their sum is gauge invariant. For a doublet dark matter particle χ, also the diagrams (c) where the Z-boson is emitted from the initial state have to be taken into account in addition to (a) and (b). Here, χ_1 and χ_2 refer to the two neutral mass eigenstates of $SU(2)_L$ doublet dark matter. Their mass splitting is assumed to be negligibly small in Eq. (B.2.1). Figures from [17].

Similarly, for the annihilation into W bosons, we find

$$\frac{vd\sigma(\chi\chi \to W f_L \bar{f}'_L)}{dE_W dE_f} = \frac{N_c \alpha_{em} f^4}{64\pi^2 \sin^2(\theta_W) m_{\rm DM}^4 (2x - x_0^2)^2 (1 - 2y - \mu_f)^2}$$
$$\times \left\{ 4(1-x)[x^2 - 2x(1-y) + 2(1-y)^2] + 2(1-x-y)x_0^4 \right.$$
$$\left. + x_0^2[5x^2 - 2x - 2 + 8(1-y)(1-x))] + x_0^6/4 \right\}, \qquad (B.2.2)$$

$$\frac{vd\sigma(\chi\chi \to W f_R \bar{f}'_R)}{dE_W dE_f} = 2c_W^2 \left. \frac{vd\sigma(\chi\chi \to Z f\bar{f})}{dE_Z dE_f} \right|_{M_Z \mapsto M_W, f^4 \mapsto (ff')^2, C_f(x) \to 1 + \mu_f - x_0^2/2}.$$
$$(B.2.3)$$

The former process can proceed via a mediating particle with the quantum numbers of the right-handed partners of either f or of f' and incorporates contributions from initial and final state radiation. The latter process is mediated by the doublet (η_f, η'_f) with quantum numbers of the left-handed fermion doublet (f, f'), and involves contributions from initial state radiation and from diagrams where the W is emitted off the internal line. Here, we assumed $m_{\eta_f} = m_{\eta_{f'}}$ for simplicity. Note that annihilation into $W f_R \bar{f}'_R$ is only possible for quarks in the SM. It can also exist for leptons if neutrinos are Dirac particles.

In connection to Sommerfeld corrections also annihilations of the charged components of the doublets containing the dark matter particle are relevant. Here it is important to project out only the contributions where the initial particles have total spin zero. We find that

$$\frac{vd\sigma(\chi^+ \chi^- \to \gamma f\bar{f})|_{S=0}}{dE_\gamma dE_f} = 4s_W^2 c_W^2 \left. \frac{vd\sigma(\chi\chi \to Z f\bar{f})}{dE_Z dE_f} \right|_{M_Z \to 0, C_f \to 1 + \mu + q_f x}. \qquad (B.2.4)$$

For annihilation into right-handed fermions f_R, the mediating particle η_f needs to have the same quantum numbers as f_R. For annihilation into left-handed fermions f_L, a mediating particle with quantum numbers of the $SU(2)_L$ partner f'_L of f_L is required.

C. Details on the statistical analysis [1]

In order to study the sampling distribution of the test statistic TS (4.2.4) in absence of a signal, we performed a *subsampling analysis* of Fermi LAT data. To this end, we extracted the gamma-ray events measured in the hemisphere pointing towards the anti-galactic center, with longitudes $|\ell| > 90°$. Any signal from dark matter annihilation should be significantly suppressed in this direction. From these events we generate 30000 random sample spectra, with the Poisson expectation values in each energy bin given by $\mu_j = fc_j$. Here, c_j is the number of actually measured events in bin j, and $f = 0.13$ is adjusted such that the total number of events above 1 GeV in each random sample is $\sim 4 \times 10^5$ (in Reg1 and Reg2 the number of events are 5.8×10^5 and 2.7×10^5, respectively). In the limit of large event numbers, this is equivalent to subsampling the energy distribution of the measured events with replacement. In each of these sample spectra, we search for VIB features like discussed above and record the largest TS value found. The histogram of the maximal TS values that are obtained in this way is shown in Fig. C.1. There, we also show the distribution that one obtains when selecting the maximum from 4 trials over a $\chi^2_{k=2}$ distribution. The agreement is very good, and we used this distribution when calculating the look-elsewhere effect above.

In Fig. C.2 we show the observed limits (black solid lines) in comparison with the limits that are expected at 68% (yellow) and 95% (green) CL. We derived these expected limits from 2000 mock data samples that were generated from the null model. In Reg1 to Reg3, the limits at $m_\chi \simeq 150\mathrm{GeV}$ are significantly weaker than the expectation; this corresponds to the large TS values in the left panel of Fig. 4.7. On the other hand, the relatively strong limits at around $m_\chi \approx 100\mathrm{GeV}$ and $m_\chi \approx 250\mathrm{GeV}$ are a consequence of the 150GeV excess, which influences the background fits. To illustrate this, we show by the dashed black lines the limits that we obtain when removing all data between 115 to 145 GeV (where the excess is most pronounced) from the fits; in this case the limits remain in the expected range.

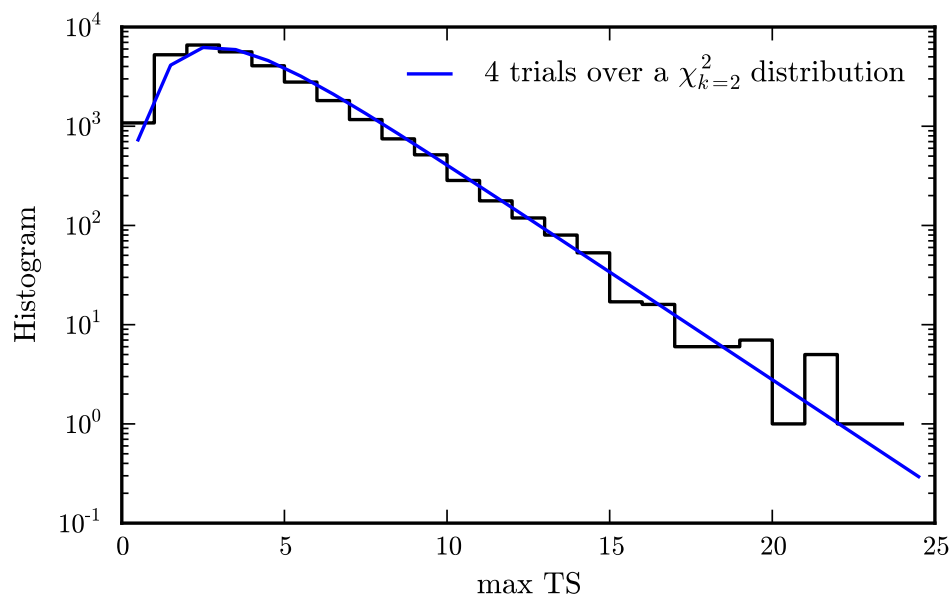
[1]This appendix has been published in [18].

Figure C.1.: Histogram of the maximal TS values obtained from a subsampling analysis of the Fermi LAT data in the hemisphere pointing towards the galactic anticenter. The blue line shows the theoretical distribution that we used to calculate the look-elsewhere effect. This figure has been published in [18].
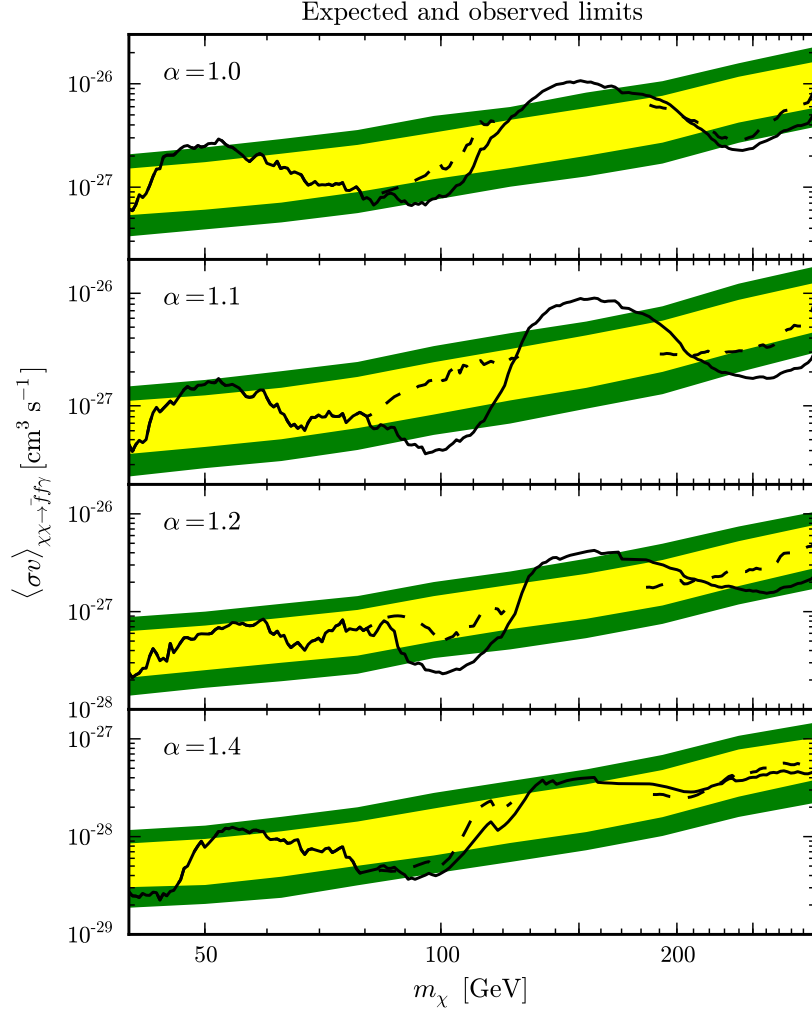
Figure C.2.: Experimental sensitivity for VIB-like features compared to actual limits. The yellow (green) bands show the expected limits at 68% (95%) CL, see text for details. The black solid line shows the actually observed limits; these limits are significantly weaker than expected at dark matter masses around 150 GeV. The dashed black line shows for comparison the limits obtained when removing the data between 115 to 145 GeV from our fits. This figure has been published in [18].

D. Results and prospects for dark matter coupling to leptons [1]

The analysis of gamma-ray features in association to leptons, $\chi\chi \to l\bar{l}\gamma$, is completely analogous to the case of quarks, with the obvious substitution of the quark charge by the lepton charge. Taking for concreteness the case of a dark matter particle coupling to muons, the different charge of the muon compared to the quark leads to a small shift in the relative importance of the loop process $\gamma\gamma$ with respect to the $\mu\bar{\mu}\gamma$ channel. However, for a small mass splitting $m_\eta/m_\chi = 1.1$ the limits from Fermi-LAT and H.E.S.S. remain essentially unchanged, as shown in Fig. D.1. A more important difference arises from the limits from the observations of dwarf galaxies with the Fermi-LAT telescope. These limits are obtained from the non-observation of secondary gamma rays from dark matter annihilations, and therefore their strength depends on the ratio of secondary-to-primary gamma rays, which in turn depends substantially on the final state. In particular, the relative importance of the dwarf limits in the case of quarks mainly stems from the fact that the annihilation channels producing primary photons $q\bar{q}\gamma$ and $\gamma\gamma$ are always accompanied by the channels $q\bar{q}g$ and gg which, as seen in Fig. 4.3, have a significantly higher branching ratio and produce only secondary gamma rays. Consequently, these bounds are significantly weaker for leptons and are less stringent than the constraints from the searches for gamma-ray features [18]. Furthermore, in the case of couplings to leptons, direct detection experiments practically pose no limit, since the only interactions with the nucleus arise at the two loop level [188]. Besides, new physics that couples exclusively to leptons is inherently hard to probe at the LHC, making LEP limits still competitive at present. LEP II constraints require $m_\eta \gtrsim 90\,\text{GeV}$ [189] unless $m_\eta/m_\chi \lesssim 1.03$ as the searches lose sensitivity in the limit of degenerate masses. In that case the bound $m_\eta \gtrsim M_Z/2$ from the Z decay width applies.

We show in Fig. D.2 the current status and prospects for this class of scenarios in the plane m_χ vs. m_η/m_χ, assuming that the dark matter particle was thermally produced. It follows from the figure that the sensitivity of gamma-ray observations reaches a maximum for $m_\eta/m_\chi \approx 1.1$, for the same reason as discussed before for quarks. It is interesting to note that even with cross sections of electroweak strength, there is a region in the parameter space where coannihilations are so efficient that it is not possible to produce thermally the whole cold dark matter population.

Searches for charged colourless scalars at hadron colliders rely mainly on Drell-Yan production and are therefore practically independent of the size of the coupling constant f. LHC searches

---

[1] The content of this appendix has been published previously in [21].
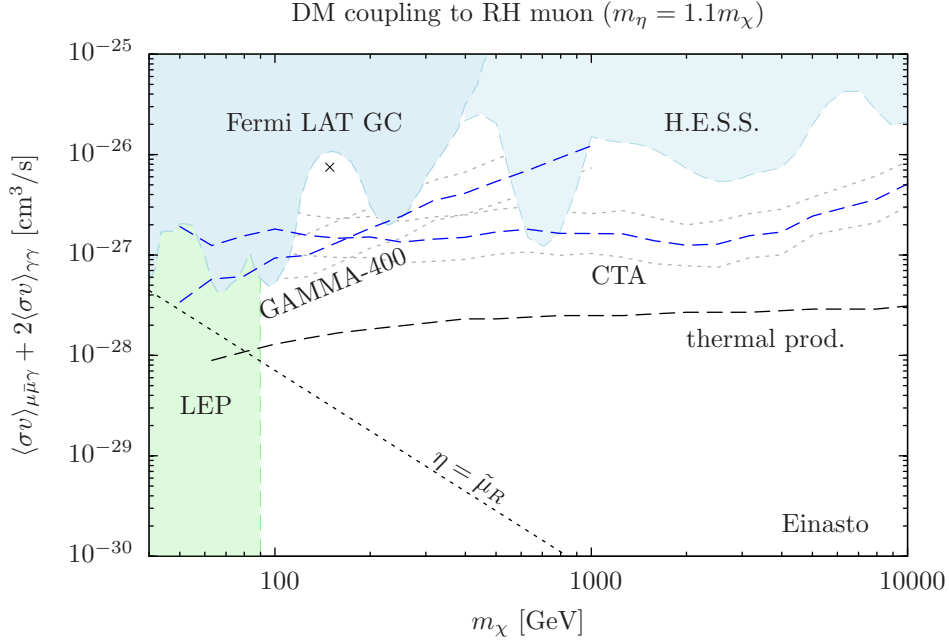
Figure D.1.: As Figs. 5.1 and 5.2, but for dark matter coupling to right-handed muons. Figure published originally in [21].

for muon pairs and missing energy [190] are starting to probe the parameter space at low masses and high splittings, whereas the LEP limits [189] still stand as the strongest ones in the region with low splittings. The ATLAS limits depend rather strongly on the leptonic flavour since taus decay mostly hadronically, thus making their identification rather challenging. In general, collider searches do not probe $m_\chi \gtrsim 100$ GeV so far, therefore, gamma-ray observations remain the most sensitive probe for dark matter coupling to leptons. The next generation of gamma-ray telescopes like GAMMA-400 and CTA will continue closing in on this class of scenarios, see Fig. D.2 (bottom); however, thermally produced dark matter particles might easily escape detection, unless the rate of annihilations is enhanced by astrophysical or particle physics boost factors.
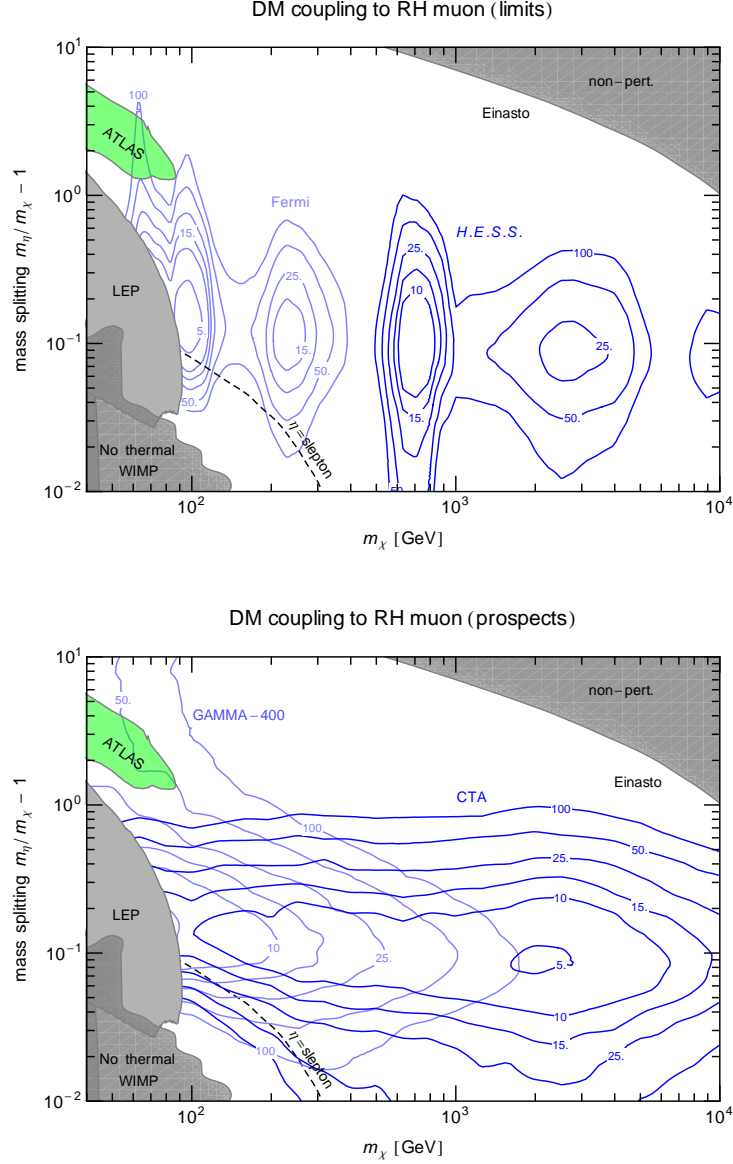
Figure D.2.: Comparison of experimental constraints as a function of the dark matter mass m_χ and the relative mass splitting $m_\eta/m_\chi - 1$. Here we assume that dark matter interacts with muons and fix the Yukawa coupling $f = f_{th}(m_\eta, m_\chi)$ at each point by requiring that the thermal relic density matches the one derived from the cosmic microwave background. The green region indicates exclusions by LHC searches. The contour lines show the ratio $r = \sigma v_{U.L.}/\sigma v_{th}$ of the upper limits on the annihilation cross section obtained from searches for spectral features with Fermi-LAT and H.E.S.S., respectively, and the cross section expected for a thermal relic. The regions inside the contours are excluded if the annihilation signal is boosted relative to the Einasto profile by a factor $BF \geq r$. Within the dark grey regions, thermal freeze-out cannot account for the cold dark matter density (in the lower right corner $\Omega_{th}h^2 < 0.12$ for all values of the coupling f, and in the upper right corner f becomes non-perturbatively large). The lower frame shows the prospects for limits from CTA and GAMMA-400. Figure published originally in [21].

Acknowledgements

Bibliography

[1] J. H. Oort, *The force exerted by the stellar system in the direction perpendicular to the galactic plane and some related problems*, Bulletin of the Astronomical Institutes of the Netherlands **6** (Aug., 1932) 249.

[2] F. Zwicky, *Die Rotverschiebung von extragalaktischen Nebeln*, Helv.Phys.Acta **6** (1933) 110–127.

[3] P. A. R. Ade et al., *Planck 2013 results. xvi. cosmological parameters*, `arXiv:1303.5076`.

[4] **XENON100** Collaboration, E. Aprile et al., *Dark Matter Results from 225 Live Days of XENON100 Data*, `arXiv:1207.5988`.

[5] **LUX** Collaboration, D. Akerib et al., *First results from the LUX dark matter experiment at the Sanford Underground Research Facility*, `arXiv:1310.8214`.

[6] **Fermi-LAT** Collaboration, M. Ackermann et al., *Search for Gamma-ray Spectral Lines with the Fermi Large Area Telescope and Dark Matter Implications*, `arXiv:1305.5597`.

[7] **AMS** Collaboration, M. Aguilar et al., *First Result from the Alpha Magnetic Spectrometer on the International Space Station: Precision Measurement of the Positron Fraction in Primary Cosmic Rays of 0.5-350 GeV*, Phys.Rev.Lett. **110** (2013), no. 14 141102.

[8] **H.E.S.S.** Collaboration, A. Abramowski et al., *Search for photon line-like signatures from Dark Matter annihilations with H.E.S.S*, Phys.Rev.Lett. **110** (2013) 041301, [`arXiv:1301.1173`].

[9] J. Aleksic, S. Ansoldi, L. Antonelli, P. Antoranz, A. Babic, et al., *Optimized dark matter searches in deep observations of Segue 1 with MAGIC*, JCAP **1402** (2014) 008, [`arXiv:1312.1535`].

[10] **IceCube** Collaboration, M. Aartsen et al., *Search for dark matter annihilations in the Sun with the 79-string IceCube detector*, Phys.Rev.Lett. **110** (2013) 131302, [`arXiv:1212.4097`].

[11] **CMS** Collaboration, *Search for supersymmetry in final states with missing transverse energy and 0, 1, 2, 3, or at least 4 b-quark jets in 8 TeV pp collisions using the variable AlphaT*, `CMS-PAS-SUS-12-028`.

[12] **ATLAS** Collaboration, G. Aad et al., *Search for squarks and gluinos with the ATLAS detector in final states with jets and missing transverse momentum and 20.3 fb-1 of*

sqrt(s)=8 TeV proton-proton collision data, .

[13] **CMS** Collaboration, S. Chatrchyan et al., *Search for dark matter and large extra dimensions in monojet events in pp collisions at sqrt(s)= 7 TeV, JHEP* **1209** (2012) 094, [`arXiv:1206.5663`].

[14] **ATLAS** Collaboration, *Search for New Phenomena in Monojet plus Missing Transverse Momentum Final States using 10fb-1 of pp Collisions at sqrts=8 TeV with the ATLAS detector at the LHC,* `ATLAS-CONF-2012-147, ATLAS-COM-CONF-2012-190`.

[15] J. Angle et al., *Limits on spin-dependent WIMP-nucleon cross-sections from the XENON10 experiment, Phys. Rev. Lett.* **101** (2008) 091301, [`arXiv:0805.2939`].

[16] D. Y. Akimov, H. Araujo, E. Barnes, V. Belov, A. Bewick, et al., *WIMP-nucleon cross-section results from the second science run of ZEPLIN-III, Phys.Lett.* **B709** (2012) 14–20, [`arXiv:1110.4769`].

[17] M. Garny, A. Ibarra, and S. Vogl, *Dark matter annihilations into two light fermions and one gauge boson: General analysis and antiproton constraints, JCAP* **1204** (2012) 033, [`arXiv:1112.5155`].

[18] T. Bringmann, X. Huang, A. Ibarra, S. Vogl, and C. Weniger, *Fermi LAT Search for Internal Bremsstrahlung Signatures from Dark Matter Annihilation, JCAP* **1207** (2012) 054, [`arXiv:1203.1312`].

[19] M. Garny, A. Ibarra, M. Pato, and S. Vogl, *Closing in on mass-degenerate dark matter scenarios with antiprotons and direct detection, JCAP* **1211** (2012) 017, [`arXiv:1207.1431`].

[20] M. Garny, A. Ibarra, M. Pato, and S. Vogl, *On the spin-dependent sensitivity of XENON100, Phys.Rev.* **D87** (2013) 056002, [`arXiv:1211.4573`].

[21] M. Garny, A. Ibarra, M. Pato, and S. Vogl, *Internal bremsstrahlung signatures in light of direct dark matter searches, JCAP* **1312** (2013) 046, [`arXiv:1306.6342`].

[22] M. Garny, A. Ibarra, S. Rydbeck, and S. Vogl, *Majorana Dark Matter with a Coloured Mediator: Collider vs Direct and Indirect Searches,* `arXiv:1403.4634`.

[23] M. Garny, A. Ibarra, and S. Vogl, *Antiproton constraints on dark matter annihilations from internal electroweak bremsstrahlung, JCAP* **1107** (2011) 028, [`arXiv:1105.5367`].

[24] T. S. van Albada, J. N. Bahcall, K. Begeman, and R. Sancisi, *Distribution of dark matter in the spiral galaxy NGC 3198, "Astrophys.J."* **295** (Aug., 1985) 305–313.

[25] D. Clowe, M. Bradac, A. H. Gonzalez, M. Markevitch, S. W. Randall, et al., *A direct empirical proof of the existence of dark matter, Astrophys.J.* **648** (2006) L109–L113, [`astro-ph/0608407`].

[26] **Planck** Collaboration, P. Ade et al., *Planck 2013 results. I. Overview of products and scientific results,* `arXiv:1303.5062`.

[27] V. Rubin, N. Thonnard, and J. Ford, W.K., *Rotational properties of 21 SC galaxies with a large range of luminosities and radii, from NGC 4605 /R = 4kpc/ to UGC 2885 /R = 122 kpc/*, *Astrophys.J.* **238** (1980) 471.

[28] J. A. Tyson, G. P. Kochanski, and I. P. Dell'Antonio, *Detailed mass map of CL0024+1654 from strong lensing*, *Astrophys.J.* **498** (1998) L107, [astro-ph/9801193].

[29] M. Bartelmann and P. Schneider, *Weak gravitational lensing*, *Phys.Rept.* **340** (2001) 291–472, [astro-ph/9912508].

[30] A. D. Lewis, D. A. Buote, and J. T. Stocke, *Chandra observations of Abell 2029: The Dark matter profile at ¡ 0.01 R(VIR) in an unusually relaxed cluster*, *Astrophys.J.* **586** (2003) 135–142, [astro-ph/0209205].

[31] G. F. Smoot, C. Bennett, A. Kogut, E. Wright, J. Aymon, et al., *Structure in the COBE differential microwave radiometer first year maps*, *Astrophys.J.* **396** (1992) L1–L5.

[32] E. Komatsu et al., *Seven-year wilkinson microwave anisotropy probe (wmap) observations: Cosmological interpretation*, *Astrophys.J.Suppl.* **192:18,2011** (Jan., 2010) 18, [arXiv:1001.4538].

[33] S. Weinberg, *Cosmology*, .

[34] Y. Nir and N. Seiberg, *Should squarks be degenerate?*, *Phys.Lett.* **B309** (1993) 337–343, [hep-ph/9304307].

[35] G. D'Ambrosio, G. Giudice, G. Isidori, and A. Strumia, *Minimal flavor violation: An Effective field theory approach*, *Nucl.Phys.* **B645** (2002) 155–187, [hep-ph/0207036].

[36] E. W. Kolb and M. S. Turner, *The Early Universe*, *Front.Phys.* **69** (1990) 1–547.

[37] G. Bertone, D. Hooper, and J. Silk, *Particle dark matter: Evidence, candidates and constraints*, *Phys. Rept.* **405** (2005) 279–390, [hep-ph/0404175].

[38] M. Drees, M. Kakizaki, and S. Kulkarni, *The Thermal Abundance of Semi-Relativistic Relics*, *Phys.Rev.* **D80** (2009) 043505, [arXiv:0904.3046].

[39] K. Griest and D. Seckel, *Three exceptions in the calculation of relic abundances*, *Phys.Rev.* **D43** (1991) 3191–3203.

[40] G. Belanger, F. Boudjema, P. Brun, A. Pukhov, S. Rosier-Lees, et al., *Indirect search for dark matter with micrOMEGAs2.4*, *Comput.Phys.Commun.* **182** (2011) 842–856, [arXiv:1004.1092].

[41] J. R. Ellis, K. A. Olive, and Y. Santoso, *Calculations of neutralino stop coannihilation in the CMSSM*, *Astropart.Phys.* **18** (2003) 395–432, [hep-ph/0112113].

[42] A. K. Harding and R. Ramaty, *The pulsar contribution to galactic cosmic-ray positrons*, Proc. 20th ICRC, Moscow **2**, 92-95 (1987).

[43] A. Atoian, F. Aharonian, and H. Volk, *Electrons and positrons in the galactic cosmic rays*, *Phys.Rev.* **D52** (1995) 3265–3275.

[44] X. Chi, E. Young, and K. Cheng, *Pulsar-wind origin of cosmic ray positrons*, *Astrophys.J.* **459** (1995) L83–L86.

[45] D. Hooper, P. Blasi, and P. D. Serpico, *Pulsars as the Sources of High Energy Cosmic Ray Positrons*, *JCAP* **0901** (2009) 025, [`arXiv:0810.1527`].

[46] **PAMELA** Collaboration, O. Adriani et al., *An anomalous positron abundance in cosmic rays with energies 1.5-100 GeV*, *Nature* **458** (2009) 607–609, [`arXiv:0810.4995`].

[47] P. Blasi and P. D. Serpico, *High-energy antiprotons from old supernova remnants*, *Phys.Rev.Lett.* **103** (2009) 081103, [`arXiv:0904.0871`].

[48] F. Aharonian, D. Khangulyan, and D. Malyshev, *Cold ultrarelativistic pulsar winds as potential sources of galactic gamma-ray lines above 100 GeV*, `arXiv:1207.0458`.

[49] L. Bergstrom and H. Snellman, *Observable monochromatic photons from cosmic photino annihilation*, *Phys.Rev.* **D37** (1988) 3737–3741.

[50] T. Bringmann and C. Weniger, *Gamma Ray Signals from Dark Matter: Concepts, Status and Prospects*, *Phys.Dark Univ.* **1** (2012) 194–217, [`arXiv:1208.5481`].

[51] `http://www.slac.stanford.edu/exp/glast/groups/canda/lat_Performance.htm`. as of 23 Feb 2012.

[52] L. Bergstrom, *Radiative processes in dark matter photino annihilations*, *Phys.Lett.* **B225** (1989) 372.

[53] T. Bringmann, L. Bergstrom, and J. Edsjo, *New Gamma-Ray Contributions to Supersymmetric Dark Matter Annihilation*, *JHEP* **0801** (2008) 049, [`arXiv:0710.3169`].

[54] L. Bergstrom, T. Bringmann, M. Eriksson, and M. Gustafsson, *Gamma rays from heavy neutralino dark matter*, *Phys.Rev.Lett.* **95** (2005) 241301, [`hep-ph/0507229`].

[55] R. Flores, K. A. Olive, and S. Rudaz, *Radiative processes in LSP annihilation*, *Phys.Lett.* **B232** (1989) 377–382.

[56] M. Drees, G. Jungman, M. Kamionkowski, and M. M. Nojiri, *Neutralino annihilation into gluons*, *Phys.Rev.* **D49** (1994) 636–647, [`hep-ph/9306325`].

[57] N. F. Bell, J. B. Dent, T. D. Jacques, and T. J. Weiler, *Dark Matter Annihilation Signatures from Electroweak Bremsstrahlung*, *Phys.Rev.* **D84** (2011) 103517, [`arXiv:1101.3357`].

[58] N. F. Bell, J. B. Dent, A. J. Galea, T. D. Jacques, L. M. Krauss, et al., *W/Z Bremsstrahlung as the Dominant Annihilation Channel for Dark Matter, Revisited*, *Phys.Lett.* **B706** (2011) 6–12, [`arXiv:1104.3823`].

[59] N. F. Bell, A. J. Brennan, and T. D. Jacques, *Neutrino signals from electroweak bremsstrahlung in solar WIMP annihilation*, *JCAP* **1210** (2012) 045, [`arXiv:1206.2977`].

[60] P. Ciafaloni, M. Cirelli, D. Comelli, A. De Simone, A. Riotto, et al., *On the Importance of Electroweak Corrections for Majorana Dark Matter Indirect Detection*, *JCAP* **1106**

(2011) 018, [arXiv:1104.2996].

[61] P. Ciafaloni, M. Cirelli, D. Comelli, A. De Simone, A. Riotto, et al., *Initial State Radiation in Majorana Dark Matter Annihilations*, *JCAP* **1110** (2011) 034, [arXiv:1107.4453].

[62] P. Ciafaloni, D. Comelli, A. De Simone, A. Riotto, and A. Urbano, *Electroweak bremsstrahlung for wino-like Dark Matter annihilations*, *JCAP* **1206** (2012) 016, [arXiv:1202.0692].

[63] A. De Simone, A. Monin, A. Thamm, and A. Urbano, *On the effective operators for Dark Matter annihilations*, *JCAP* **1302** (2013) 039, [arXiv:1301.1486].

[64] M. Asano, T. Bringmann, and C. Weniger, *Indirect dark matter searches as a probe of degenerate particle spectra*, *Phys.Lett.* **B709** (2012) 128–132, [arXiv:1112.5158].

[65] K. Fukushima, Y. Gao, J. Kumar, and D. Marfatia, *Bremsstrahlung signatures of dark matter annihilation in the Sun*, *Phys.Rev.* **D86** (2012) 076014, [arXiv:1208.1010].

[66] F. Luo and T. You, *Enhancement of Majorana Dark Matter Annihilation Through Higgs Bremsstrahlung*, *JCAP* **1312** (2013) 024, [arXiv:1310.5129].

[67] L. Bergström, T. Bringmann, and J. Edsjö, *New Positron Spectral Features from Supersymmetric Dark Matter - a Way to Explain the PAMELA Data?*, *Phys. Rev.* **D78** (2008) 103520, [arXiv:0808.3725].

[68] T. Sjostrand, S. Mrenna, and P. Z. Skands, *PYTHIA 6.4 Physics and Manual*, *JHEP* **0605** (2006) 026, [hep-ph/0603175].

[69] L. Bergstrom and P. Ullio, *Full one-loop calculation of neutralino annihilation into two photons*, *Nucl.Phys. B* **504** (1997) 27–44, [hep-ph/9706232].

[70] Z. Bern, P. Gondolo, and M. Perelstein, *Neutralino annihilation into two photons*, *Phys.Lett.* **B411** (1997) 86–96, [hep-ph/9706538].

[71] P. Ullio and L. Bergstrom, *Neutralino annihilation into a photon and a Z boson*, *Phys.Rev.* **D57** (1998) 1962–1971, [hep-ph/9707333].

[72] A. Ibarra, M. Totzauer, and S. Wild, *Higher order dark matter annihilations in the Sun and implications for IceCube*, arXiv:1402.4375.

[73] K. Nakamura et al., *Review of particle physics*, *J.Phys.G* **G37** (2010) 075021.

[74] J. F. Navarro, C. S. Frenk, and S. D. White, *A Universal density profile from hierarchical clustering*, *Astrophys.J.* **490** (1997) 493–508, [astro-ph/9611107].

[75] A. Abdo, M. Ackermann, M. Ajello, W. Atwood, L. Baldini, et al., *Fermi LAT Search for Photon Lines from 30 to 200 GeV and Dark Matter Implications*, *Phys.Rev.Lett.* **104** (2010) 091302, [arXiv:1001.4836].

[76] R. Catena and P. Ullio, *A novel determination of the local dark matter density*, *JCAP* **1008** (2010) 004, [arXiv:0907.0018].

[77] P. Salucci, F. Nesti, G. Gentile, and C. Martins, *The dark matter density at the Sun's location*, Astron.Astrophys. **523** (2010) A83, [arXiv:1003.3101].

[78] G. R. Blumenthal, S. M. Faber, R. Flores, and J. R. Primack, *Contraction of Dark Matter Galactic Halos Due to Baryonic Infall*, Astrophys. J. **301** (1986) 27.

[79] O. Y. Gnedin and J. R. Primack, *Dark Matter Profile in the Galactic Center*, Phys. Rev. Lett. **93** (2004) 061302, [astro-ph/0308385].

[80] M. Gustafsson, M. Fairbairn, and J. Sommer-Larsen, *Baryonic Pinching of Galactic Dark Matter Haloes*, Phys. Rev. **D74** (2006) 123522, [astro-ph/0608634].

[81] O. Y. Gnedin et al., *Halo Contraction Effect in Hydrodynamic Simulations of Galaxy Formation*, arXiv:1108.5736.

[82] F. Iocco, M. Pato, G. Bertone, and P. Jetzer, *Dark Matter distribution in the Milky Way: microlensing and dynamical constraints*, JCAP **1111** (2011) 029, [arXiv:1107.5810].

[83] http://fermi.gsfc.nasa.gov/.

[84] A. R. Pullen, R.-R. Chary, and M. Kamionkowski, *Search with EGRET for a Gamma Ray Line from the Galactic Center*, Phys.Rev. **D76** (2007) 063006, [astro-ph/0610295].

[85] G. Vertongen and C. Weniger, *Hunting Dark Matter Gamma-Ray Lines with the Fermi LAT*, JCAP **1105** (2011) 027, [arXiv:1101.2610].

[86] T. Bringmann, F. Calore, G. Vertongen, and C. Weniger, *On the Relevance of Sharp Gamma-Ray Features for Indirect Dark Matter Searches*, Phys.Rev. **D84** (2011) 103525, [arXiv:1106.1874].

[87] W. A. Rolke, A. M. Lopez, and J. Conrad, *Confidence Intervals with Frequentist Treatment of Statistical and Systematic Uncertainties*, Nucl. Instrum. Meth. **A551** (2005) 493–503, [physics/0403059].

[88] http://fermi.gsfc.nasa.gov/ssc/data/analysis/LAT_caveats.html. as of 23 Feb 2012.

[89] M. Su and D. P. Finkbeiner, *Strong Evidence for Gamma-ray Line Emission from the Inner Galaxy*, arXiv:1206.1616.

[90] E. Tempel, A. Hektor, and M. Raidal, *Fermi 130 GeV gamma-ray excess and dark matter annihilation in sub-haloes and in the Galactic centre*, JCAP **1209** (2012) 032, [arXiv:1205.1045].

[91] **Fermi-LAT** Collaboration, M. Ackermann et al., *Search for Gamma-ray Spectral Lines with the Fermi Large Area Telescope and Dark Matter Implications*, Phys.Rev. **D88** (2013) 082002, [arXiv:1305.5597].

[92] **Fermi-LAT** Collaboration, A. A. Abdo et al., *Observations of Milky Way Dwarf Spheroidal galaxies with the Fermi-LAT detector and constraints on Dark Matter models*, Astrophys. J. **712** (2010) 147–158, [arXiv:1001.4531].

[93] **Fermi-LAT** Collaboration, M. Ackermann et al., *Constraining Dark Matter Models from a Combined Analysis of Milky Way Satellites with the Fermi Large Area Telescope*, *Phys.Rev.Lett.* **107** (2011) 241302, [`arXiv:1108.3546`].

[94] A. Geringer-Sameth and S. M. Koushiappas, *Exclusion of canonical WIMPs by the joint analysis of Milky Way dwarfs with Fermi*, *Phys.Rev.Lett.* **107** (2011) 241303, [`arXiv:1108.2914`].

[95] T. Moroi, *The Muon Anomalous Magnetic Dipole Moment in the Minimal Supersymmetric Standard Model*, *Phys. Rev.* **D53** (1996) 6565–6575, [`hep-ph/9512396`].

[96] F. Jegerlehner and A. Nyffeler, *The Muon g-2*, *Phys. Rept.* **477** (2009) 1–110, [`arXiv:0902.3360`].

[97] M. E. Peskin and T. Takeuchi, *A New constraint on a strongly interacting Higgs sector*, *Phys. Rev. Lett.* **65** (1990) 964–967.

[98] M. E. Peskin and T. Takeuchi, *Estimation of oblique electroweak corrections*, *Phys. Rev.* **D46** (1992) 381–409.

[99] V. Barger, W.-Y. Keung, H. E. Logan, and G. Shaughnessy, *Neutralino annihilation to q anti-q g*, *Phys.Rev.* **D74** (2006) 075005, [`hep-ph/0608215`].

[100] M. Kachelriess, P. Serpico, and M. A. Solberg, *On the role of electroweak bremsstrahlung for indirect dark matter signatures*, *Phys.Rev.* **D80** (2009) 123533, [`arXiv:0911.0001`].

[101] R. Bernabei et al., *New results from DAMA/LIBRA*, *Eur. Phys. J.* **C67** (2010) 39–49, [`arXiv:1002.1028`].

[102] G. Angloher, M. Bauer, I. Bavykina, A. Bento, C. Bucci, et al., *Results from 730 kg days of the CRESST-II Dark Matter Search*, *Eur.Phys.J.* **C72** (2012) 1971, [`arXiv:1109.0702`].

[103] C. Aalseth, P. Barbeau, J. Colaresi, J. Collar, J. Leon, et al., *Search for an Annual Modulation in a P-type Point Contact Germanium Dark Matter Detector*, `arXiv:1106.0650`.

[104] **CDMS** Collaboration, R. Agnese et al., *Silicon Detector Dark Matter Results from the Final Exposure of CDMS II*, *Phys.Rev.Lett.* **111** (2013) 251301, [`arXiv:1304.4279`].

[105] **CDMS** Collaboration, Z. Ahmed et al., *Search for annual modulation in low-energy CDMS-II data*, `arXiv:1203.1309`.

[106] D. G. Cerdeno and A. M. Green, *Direct detection of WIMPs*, `arXiv:1002.1912`.

[107] G. Jungman, M. Kamionkowski, and K. Griest, *Supersymmetric dark matter*, *Phys. Rept.* **267** (1996) 195–373, [`hep-ph/9506380`].

[108] J. D. Lewin and P. F. Smith, *Review of mathematics, numerical factors, and corrections for dark matter experiments based on elastic nuclear recoil*, *Astropart. Phys.* **6** (1996) 87–112.

[109] M. C. Smith, G. Ruchti, A. Helmi, R. Wyse, J. Fulbright, et al., *The RAVE Survey: Constraining the Local Galactic Escape Speed*, Mon.Not.Roy.Astron.Soc. **379** (2007) 755–772, [`astro-ph/0611671`].

[110] M. W. Goodman and E. Witten, *Detectability of Certain Dark Matter Candidates*, Phys.Rev. **D31** (1985) 3059.

[111] M. Drees and M. Nojiri, *Neutralino-nucleon scattering reexamined*, Phys.Rev. **D48** (1993) 3483–3501, [`hep-ph/9307208`].

[112] J. R. Ellis, K. A. Olive, and C. Savage, *Hadronic Uncertainties in the Elastic Scattering of Supersymmetric Dark Matter*, Phys.Rev. **D77** (2008) 065026, [`arXiv:0801.3656`].

[113] J. Hisano, K. Ishiwata, and N. Nagata, *Gluon contribution to the dark matter direct detection*, Phys.Rev. **D82** (2010) 115007, [`arXiv:1007.2601`].

[114] Y. Akrami, C. Savage, P. Scott, J. Conrad, and J. Edsjo, *How well will ton-scale dark matter direct detection experiments constrain minimal supersymmetry?*, JCAP **1104** (2011) 012, [`arXiv:1011.4318`].

[115] J. Pumplin, D. Stump, J. Huston, H. Lai, P. M. Nadolsky, et al., *New generation of parton distributions with uncertainties from global QCD analysis*, JHEP **0207** (2002) 012, [`hep-ph/0201195`].

[116] A. Galper, O. Adriani, R. Aptekar, I. Arkhangelskaja, A. Arkhangelskiy, et al., *Status of the GAMMA-400 Project*, Adv.Space Res. **51** (2013) 297–300, [`arXiv:1201.2490`].

[117] **CTA** Collaboration, M. Actis et al., *Design concepts for the Cherenkov Telescope Array CTA: An advanced facility for ground-based high-energy gamma-ray astronomy*, Exper.Astron. **32** (2011) 193–316, [`arXiv:1008.3703`].

[118] K. Bernlohr, A. Barnacka, Y. Becherini, O. B. Bigas, E. Carmona, et al., *Monte Carlo design studies for the Cherenkov Telescope Array*, Astropart.Phys. **43** (2013) 171–188, [`arXiv:1210.3503`].

[119] J. Diemand et al., *Clumps and streams in the local dark matter distribution*, Nature **454** (2008) 735–738, [`arXiv:0805.1244`].

[120] **Fermi-LAT** Collaboration, M. Ackermann et al., *The Fermi Large Area Telescope On Orbit: Event Classification, Instrument Response Functions, and Calibration*, Astrophys.J.Suppl. **203** (2012) 4, [`arXiv:1206.1896`].

[121] C. Weniger, *A Tentative Gamma-Ray Line from Dark Matter Annihilation at the Fermi Large Area Telescope*, JCAP **1208** (2012) 007, [`arXiv:1204.2797`].

[122] L. Bergstrom, G. Bertone, J. Conrad, C. Farnier, and C. Weniger, *Investigating Gamma-Ray Lines from Dark Matter with Future Observatories*, JCAP **1211** (2012) 025, [`arXiv:1207.6773`].

[123] J. Aleksic, J. Rico, and M. Martinez, *Optimized analysis method for indirect dark matter*

searches with Imaging Air Cherenkov Telescopes, *JCAP* **1210** (2012) 032, [`arXiv:1209.5589`].

[124] G. J. Feldman and R. D. Cousins, *A Unified approach to the classical statistical analysis of small signals*, *Phys.Rev.* **D57** (1998) 3873–3889, [`physics/9711021`].

[125] **DARWIN** Collaboration, L. Baudis, *DARWIN: dark matter WIMP search with noble liquids*, `arXiv:1201.2402`.

[126] http://dpnc.unige.ch/dampe/index.html.

[127] **XENON1T** Collaboration, E. Aprile, *The XENON1T Dark Matter Search Experiment*, `arXiv:1206.6288`.

[128] http://cdms.berkeley.edu/.

[129] http://www.eureca.ox.ac.uk/.

[130] http://darwin.physik.uzh.ch/.

[131] **COUPP** Collaboration, E. Behnke et al., *First Dark Matter Search Results from a 4-kg CF$_3$I Bubble Chamber Operated in a Deep Underground Site*, *Phys.Rev.* **D86** (2012) 052001, [`arXiv:1204.3094`].

[132] S. Archambault, F. Aubin, M. Auger, E. Behnke, B. Beltran, et al., *Dark Matter Spin-Dependent Limits for WIMP Interactions on F-19 by PICASSO*, *Phys.Lett.* **B682** (2009) 185–192, [`arXiv:0907.0307`].

[133] **CDMS-II** Collaboration, Z. Ahmed et al., *Dark Matter Search Results from the CDMS II Experiment*, *Science* **327** (2010) 1619–1621, [`arXiv:0912.3592`].

[134] **XENON100** Collaboration, E. Aprile et al., *First Dark Matter Results from the XENON100 Experiment*, *Phys. Rev. Lett.* **105** (2010) 131302, [`arXiv:1005.0380`].

[135] G. Angloher, M. Bauer, I. Bavykina, A. Bento, C. Bucci, et al., *Results from 730 kg days of the CRESST-II Dark Matter Search*, *Eur.Phys.J.* **C72** (2012) 1971, [`arXiv:1109.0702`].

[136] M. Ressell and D. Dean, *Spin dependent neutralino - nucleus scattering for A approximately 127 nuclei*, *Phys.Rev.* **C56** (1997) 535–546, [`hep-ph/9702290`].

[137] J. Engel, *Nuclear form-factors for the scattering of weakly interacting massive particles*, *Phys.Lett.* **B264** (1991) 114–119.

[138] P. Toivanen, M. Kortelainen, J. Suhonen, and J. Toivanen, *Large-scale shell-model calculations of elastic and inelastic scattering rates of lightest supersymmetric particles (LSP) on I-127, Xe-129, Xe-131, and Cs-133 nuclei*, *Phys.Rev.* **C79** (2009) 044302.

[139] J. Menendez, D. Gazit, and A. Schwenk, *Spin-dependent WIMP scattering off nuclei*, `arXiv:1208.1094`.

[140] **XENON100** Collaboration, E. Aprile et al., *Limits on spin-dependent WIMP-nucleon cross sections from 225 live days of XENON100 data*, *Phys.Rev.Lett.* **111** (2013), no. 2

021301, [arXiv:1301.6620].

[141] C. Savage, P. Gondolo, and K. Freese, *Can WIMP spin dependent couplings explain DAMA data, in light of null results from other experiments?*, *Phys.Rev.* **D70** (2004) 123513, [astro-ph/0408346].

[142] R. Catena and P. Ullio, *A novel determination of the local dark matter density*, *JCAP* **1008** (2010) 004, [arXiv:0907.0018].

[143] C. Rott, "Latest results from icecube." IDM2012.

[144] C. Rott, *Review of Indirect WIMP Search Experiments*, *Nucl.Phys.Proc.Suppl.* **235-236** (2013) 413–420, [arXiv:1210.4161].

[145] M. Felizardo, T. Girard, T. Morlat, A. Fernandes, A. Ramos, et al., *Final Analysis and Results of the Phase II SIMPLE Dark Matter Search*, *Phys.Rev.Lett.* **108** (2012) 201302, [arXiv:1106.3014].

[146] **CDMS** Collaboration, D. Akerib et al., *Limits on spin-dependent wimp-nucleon interactions from the cryogenic dark matter search*, *Phys.Rev.* **D73** (2006) 011102, [astro-ph/0509269].

[147] **COUPP** Collaboration, E. Behnke et al., *Improved Spin-Dependent WIMP Limits from a Bubble Chamber*, *Science* **319** (2008) 933–936, [arXiv:0804.2886].

[148] A. Rajaraman, W. Shepherd, T. M. Tait, and A. M. Wijangco, *LHC Bounds on Interactions of Dark Matter*, *Phys.Rev.* **D84** (2011) 095013, [arXiv:1108.1196].

[149] **ATLAS** Collaboration, G. Aad et al., *Search for dark matter candidates and large extra dimensions in events with a jet and missing transverse momentum with the ATLAS detector*, arXiv:1210.4491.

[150] P. J. Fox, R. Harnik, J. Kopp, and Y. Tsai, *Missing Energy Signatures of Dark Matter at the LHC*, *Phys.Rev.* **D85** (2012) 056011, [arXiv:1109.4398].

[151] O. Buchmueller, M. J. Dolan, and C. McCabe, *Beyond Effective Field Theory for Dark Matter Searches at the LHC*, *JHEP* **1401** (2014) 025, [arXiv:1308.6799].

[152] M. Papucci, A. Vichi, and K. M. Zurek, *Monojet versus rest of the world I: t-channel Models*, arXiv:1402.2285.

[153] A. Ibarra, M. Totzauer, and S. Wild, *High-energy neutrino signals from the Sun in dark matter scenarios with internal bremsstrahlung*, *JCAP* **1312** (2013) 043, [arXiv:1311.1418].

[154] M. Pato, L. Baudis, G. Bertone, R. Ruiz de Austri, L. E. Strigari, et al., *Complementarity of Dark Matter Direct Detection Targets*, *Phys.Rev.* **D83** (2011) 083505, [arXiv:1012.3458].

[155] H. Silverwood, P. Scott, M. Danninger, C. Savage, J. Edsjo, et al., *Sensitivity of IceCube-DeepCore to neutralino dark matter in the MSSM-25*, arXiv:1210.0844.

[156] E. Vázquez Jáuregui, "Coupp500: a 500kg bubble chamber for dark matter detection." IDM2012.

[157] *Search for supersymmetry with jets and missing transverse momentum: Additional model interpretations*, Tech. Rep. ATLAS-CONF-2011-155, CERN, Geneva, Nov, 2011.

[158] **L3** Collaboration, P. Achard et al., *Search for scalar leptons and scalar quarks at LEP*, *Phys.Lett.* **B580** (2004) 37–49, [`hep-ex/0310007`].

[159] G. Belanger, M. Heikinheimo, and V. Sanz, *Model-Independent Bounds on Squarks from Monophoton Searches*, `arXiv:1205.1463`.

[160] H. Baer, V. Barger, and A. Mustafayev, *Neutralino dark matter in mSUGRA/CMSSM with a 125 GeV light Higgs scalar*, *JHEP* **1205** (2012) 091, [`arXiv:1202.4038`].

[161] O. Buchmueller, R. Cavanaugh, A. De Roeck, M. Dolan, J. Ellis, et al., *Higgs and Supersymmetry*, *Eur.Phys.J.* **C72** (2012) 2020, [`arXiv:1112.3564`].

[162] C. Strege, G. Bertone, D. Cerdeno, M. Fornasa, R. R. de Austri, et al., *Updated global fits of the cMSSM including the latest LHC SUSY and Higgs searches and XENON100 data*, *JCAP* **1203** (2012) 030, [`arXiv:1112.4192`].

[163] A. Fowlie, M. Kazana, K. Kowalska, S. Munir, L. Roszkowski, et al., *The CMSSM Favoring New Territories: The Impact of New LHC Limits and a 125 GeV Higgs*, `arXiv:1206.0264`.

[164] P. Gondolo, J. Edsjo, P. Ullio, L. Bergstrom, M. Schelke, et al., *DarkSUSY: Computing supersymmetric dark matter properties numerically*, *JCAP* **0407** (2004) 008, [`astro-ph/0406204`].

[165] **ATLAS** Collaboration, G. Aad et al., *Search for squarks and gluinos with the atlas detector in final states with jets and missing transverse momentum using 4.7 fb-1 of sqrt(s) = 7 tev proton-proton collision data*, `arXiv:1208.0949`.

[166] **ATLAS** Collaboration, G. Aad et al., *Search for direct top squark pair production in final states with one isolated lepton, jets, and missing transverse momentum in sqrt(s) = 7 TeV pp collisions using 4.7 fb-1 of ATLAS data*, `arXiv:1208.2590`.

[167] C. Cheung, L. J. Hall, D. Pinner, and J. T. Ruderman, *Prospects and Blind Spots for Neutralino Dark Matter*, *JHEP* **1305** (2013) 100, [`arXiv:1211.4873`].

[168] G. Busoni, A. De Simone, E. Morgante, and A. Riotto, *On the Validity of the Effective Field Theory for Dark Matter Searches at the LHC*, *Phys.Lett.* **B728** (2014) 412–421, [`arXiv:1307.2253`].

[169] S. Chang, R. Edezhath, J. Hutchinson, and M. Luty, *Effective WIMPs*, *Phys.Rev.* **D89** (2014) 015011, [`arXiv:1307.8120`].

[170] H. An, L.-T. Wang, and H. Zhang, *Dark matter with t-channel mediator: a simple step beyond contact interaction*, `arXiv:1308.0592`.

[171] Y. Bai and J. Berger, *Fermion Portal Dark Matter*, *JHEP* **1311** (2013) 171, [`arXiv:1308.0612`].

[172] A. DiFranzo, K. I. Nagao, A. Rajaraman, and T. M. P. Tait, *Simplified Models for Dark Matter Interacting with Quarks*, *JHEP* **1311** (2013) 014, [`arXiv:1308.2679`].

[173] J. Kopp, L. Michaels, and J. Smirnov, *Loopy Constraints on Leptophilic Dark Matter and Internal Bremsstrahlung*, `arXiv:1401.6457`.

[174] S. Chang, R. Edezhath, J. Hutchinson, and M. Luty, *Leptophilic Effective WIMPs*, `arXiv:1402.7358`.

[175] Y. Bai and J. Berger, *Lepton Portal Dark Matter*, `arXiv:1402.6696`.

[176] R. Mahbubani, M. Papucci, G. Perez, J. T. Ruderman, and A. Weiler, *Light non-degenerate squarks at the LHC*, `arXiv:1212.3328`.

[177] M. Kramer, A. Kulesza, R. van der Leeuw, M. Mangano, S. Padhi, et al., *Supersymmetry production cross sections in pp collisions at $\sqrt{s} = 7$ TeV*, `arXiv:1206.2892`.

[178] https://twiki.cern.ch/twiki/bin/view/LHCPhysics/SUSYCrossSections.

[179] W. Hollik, J. M. Lindert, and D. Pagani, *NLO corrections to squark-squark production and decay at the LHC*, *JHEP* **1303** (2013) 139, [`arXiv:1207.1071`].

[180] A. Pukhov, *CalcHEP 2.3: MSSM, structure functions, event generation, batchs, and generation of matrix elements for other packages*, `hep-ph/0412191`.

[181] J. Alwall, M. Herquet, F. Maltoni, O. Mattelaer, and T. Stelzer, *MadGraph 5 : Going Beyond*, *JHEP* **1106** (2011) 128, [`arXiv:1106.0522`].

[182] S. Ovyn, X. Rouby, and V. Lemaitre, *DELPHES, a framework for fast simulation of a generic collider experiment*, `arXiv:0903.2225`.

[183] T. Sjöstrand, S. Mrenna, and P. Skands, *PYTHIA 6.4 physics and manual*, *Journal of High Energy Physics* **5** (May, 2006) 26, [`hep-ph/0603175`].

[184] H. K. Dreiner, M. Kramer, and J. Tattersall, *How low can SUSY go? Matching, monojets and compressed spectra*, *Europhys.Lett.* **99** (2012) 61001, [`arXiv:1207.1613`].

[185] O. Gedalia, Y. Grossman, Y. Nir, and G. Perez, *Lessons from Recent Measurements of D0 - anti-D0 Mixing*, *Phys.Rev.* **D80** (2009) 055024, [`arXiv:0906.1879`].

[186] E. Ma and S. Pakvasa, *Variation of Mixing Angles and Masses With q^2 in the Standard Six Quark Model*, *Phys.Rev.* **D20** (1979) 2899.

[187] V. D. Barger, M. Berger, and P. Ohmann, *Universal evolution of CKM matrix elements*, *Phys.Rev.* **D47** (1993) 2038–2045, [`hep-ph/9210260`].

[188] J. Kopp, V. Niro, T. Schwetz, and J. Zupan, *Dama/libra and leptonically interacting dark matter*, *Phys.Rev.D* **80:083502,2009** (July, 2009) [`arXiv:0907.3159`].

[189] http://lepsusy.web.cern.ch/lepsusy/www/sleptons_summer04/slep_final.html.

[190] http://atlas.web.cern.ch/Atlas/GROUPS/PHYSICS/CONFNOTES/ATLAS-CONF-2013-049.